THE UNIVERSITY OF ASTON IN BIRMINGHAM

# "THE APPLICATION OF LOW ENERGY ACCELERATORS TO ANALYSIS PROBLEMS"

Thesis submitted for the Degree of
Master of Sciences

by

T. Vilaithong, B.Sc.

Department of Physics
August, 1971

# ABSTRACT

The work reported here describes the characteristics of low energy particle accelerators and the way in which these instruments may be used to study analytical problems.

Two specific analytical problems which have been studied using a 500 KV Van de Graaf accelerator are described.

In the first the stoichiometry of the ferrite $MgFe_2O_4$ formed by sintering MgO and $Fe_2O_3$ was studied using fast neutron activation analysis. Samples of the ferrite were irradiated with 14-MeV neutrons produced in the Van de Graaf by the $T(d,n)^4He$ reaction. The radio-active isotopes $^{24}Na$ and $^{56}Mn$ were produced by the reactions $^{24}Mg(n,p)^{24}Na$ and $^{56}Fe(n,p)^{56}Mn$. Subsequent $\gamma$-ray spectrometry enabled the relative quantities of Mg and Fe to be determined and comparison with similar measurements on unsintered stoichimetric mixes of MgO and $Fe_2O_3$ allowed any relative loss of Mg or Fe during the sintering process to be observed.

Samples sintered at 1100°C, 1200°C and 1400°C all showed a relative loss of about 6% of the iron.

The second problem studied was the possible incorporation of F in chromium plating when fluorine salts are incorporated in the plating bath. Samples of the plate were bombarded with protons having various energies up to about 400 KeV. These protons generated the $^{19}F(p, \alpha\gamma)^{16}O$ reaction at depths within the plate where the protons reached an energy of 340 KeV at which energy the reaction has a strong resonance. It was observed that all samples had relatively large quantities of F on the surfaces and much lower, but constant, level in the thickness of the plate. An attempt was made to estimate the amount of F at different depths by comparing the observed $\gamma$-rays with a standard of $CaF_2$.

Possible explanations of these observations are discussed and further experiments suggested.

# ACKNOWLEDGEMENTS

I would like to thank Dr. D. Crumpton for devoting much of his time in supervising the project and for his many valuable suggestions. I am also grateful to Dr. P. E. Francois for his continuous guidance and encouragement.

I would also like to thank Professor S. E. Hunt for offering me the opportunity to carry out the research programme and for his interest in the project. My thanks are also due to Mr. N. W. Grimes for supplying the sintered ferrite samples and for helpful discussions and to Dr. P. N. Cooper for the use of the water-cooled target assembly and electronic components.

I am indebted to Mr. P. L. Barrett for his help in preparing the microcracked chromium samples and to my colleagues of the Applied Nuclear Physics Division for many generous discussions. The assistance received from Messer F. Lane and the work shop staff is gratefully acknowledged. My thanks are also due to Messers J. Phul and B. Biggs for the operation and maintenance of the Van de Graaf accelerator.

Thanks are given to the British Council for a grant during this work.

Finally I would like to thank my wife for much of her patience and understanding.

T. VILAITHONG

## TABLE OF CONTENTS

Page No.

CHAPTER III NUCLEAR INSTRUMENTATIONS

3.3 Detection of gamma radiation

CHAPTER IV AN INVESTIGATION BY NEUTRON ACTIVATION OF THE Mg/Fe RATIO AFTER THE REACTION $MgO + Fe_2O_3 \rightarrow MgFe_2O_4$

CHAPTER V ANALYSIS OF FLUORINE IN MICROCRACKED CHROMIUM BY METHOD OF PROMPT $\gamma$-RADIATION DETECTION

CHAPTER VI GENERAL CONCLUSION

# LIST OF FIGURES

Figure No.

Figure No.

Figure No.

# CHAPTER I INTRODUCTION

## 1. Introduction

In the early development of machines (Van-de-Graaf 1931, Cockcroft-Walton 1932, Lawrence 1932) (1),(2),(3) for the acceleration of charged particles in the beginning of this century the use of particle accelerators was confined to research in nuclear physics. In fact, the first nuclear reaction induced by artificially accelerated particles was obtained by Cockcroft and Walton in 1932, the $^7Li(p, \alpha)^4He$ reaction (4).

Important as their works is for nuclear physics, the technological achievement implied was no less significant, the accelerators developed by them have been for many years a valuable tool for research in all branches of science and engineering.

The phenomenal growth of nuclear science during the past two decades has been replete with important consequences for all natural sciences. The physical method of analysis, particularly the discipline of nuclear activation analysis has been specially favoured by this development.

In recent years, it has been recognised that micro-amounts of impurities or trace elements in a system can exert a considerable influence on the biological, chemical, mechanical and physical properties of the system. With this realization there came a great demand for experimental determination of these micro-amounts of material. The potentially high sensitivity of nuclear techniques, their simplicity and their independence of chemical state have made them particularly suitable for the accurate determination of a wide variety of elements which are not conveniently determined by conventional chemical analysis.

The basic principle of activation analysis is that a stable isotope, when irradiated by neutrons (or charged particles), can undergo nuclear transformation to produce a radioactive nuclide. Each of these radioactive nuclides have characteristic properties including the half-life and the type and energy of the emitted radiations. These characteristics can be identified by relatively simple techniques which, however have excellent sensitivity for quantitative estimation.

Activation analysis requires a consideration of the law governing growth and decay in radioactivation. The activity induced in a sample can be expressed by the following activation equation (Section 4.2) as

$$A = N\sigma\phi(1-e^{-\lambda t}) \qquad (1.1)$$

where A = induced activity present at the end of irradiation, dis./sec.

N = number of target atoms present

$\sigma$ = activation cross section, $cm.^2$

$\phi$ = irradiation flux, particles/$cm.^2$-sec.

t = irradiation time

$\lambda$ = decay constant of the product nuclide

Eq. (1.1) then shows how the induced activity and hence the sensitivity depends on various nuclear parameters.

Activation analysis, being a nuclear technique, is not similar to other elemental analysis, which are based upon chemical reactions or electronic excitations, but not necessarily better than other methods. There are many different methods of elemental analysis, $^{(5)}$ in addition to activation analysis, for example;

spectro photometry, emission spectroscopy, atomic absorption, flame emission, polarography, X-ray emission, electron microprobe spectroscopy and spark-source mass spectrometry. However there are some desirable features of activation analysis which meet the demand for the determination of impurities at the p.p.m. and p.p.b. level. These are, in favourable cases

(1) the rapidity of analysis
(2) the insensitivity to chemical form of element
(3) the non destructive nature of analysis
(4) the high sensitivity if a large particle flux is available
(5) the availability of a signal for automatic recording of results and automatic control of process
(6) the equipment requirements may be relatively inexpensive
(7) independence of distribution within the sample

Not all these will be applicable to any given case.

Though the chemical and instrument methods used are relatively simple and inexpensive, the irradiation stage of the technique requires access to source of sub-atomic particles or radiations.

The discovery of fission in 1939, by O. Hahn and F. Strassman, and the subsequent construction of nuclear reactors made it possible to obtain fluxes of slow neutrons as high as $10^{15}$ n/cm.$^2$-sec. However the use of reactor neutron sources is limited to thermal neutron activation analysis, utilizing the

$(n, \gamma)$ reaction, and reactions that have fairly long half lives. Besides, thermal neutron activation analysis for light elements $(Z < 10)$ is not possible owing to the extremely small absorption cross section they show and because mainly isotopes produced are short lived. This limits the number of elements that can be analysed and the speed at which results can be obtained in addition to the expense of such reactors and the attendant hazards which are also factors in limiting their use for neutron activation analysis.

In recent years, one of the fastest developing branches of radiation technology is the use of acceleration neutron source for neutron activation. The best high-energy neutron producer for bombarding energy less than 1 MeV is the $T(d,n)^4He$ reaction, which yields mono-energetic neutrons in the 10-16 MeV energies range.

The development of high intensities ion sources during the past fifteen years together with the fact that tritium targets are now readily available at relatively low cost have made low energy accelerators such as the 500 KV Van-de-Graaf and the Cockcroft-Walton major tools for production of 14 MeV neutrons. As a result, neutron generators of high flux, low cost are now available, for example, the neutron generator, developed by the research staff at the Taxas Nuclear Corporation (6) operates at 150 KV and costs less than £10,000 is capable of producing a yield of $10^{11}$n/sec. With suitable moderator, a useable slow neutron flux of $10^8$ to $10^9$ n/cm$^2$-sec. can be obtained.

For higher energy accelerators, charged particle activation analysis for light elements is also possible and can serve as an independent technique. Another nuclear technique which has commanded a great interest in recent years is the method of detecting prompt $\gamma$-rays during charged particles bombardment. The problem of surface analysis is almost impossible by neutron activation method due to high penetratibility of neutrons. Low energy charged particles can be used with advantage to determine light elements in surface, due to its low depth of penetration, by prompt $\gamma$-rays detecting method.

In this work the applications of a 500 KV accelerator set have been investigated. Two specific problems have been studied by means of neutron activation and charged particle analysis.

# CHAPTER II SPECIFIC CHARACTERISTICS OF LOW ENERGY ELECTROSTATIC ACCELERATORS OF INTEREST FOR ACTIVATION ANALYSIS

## 2.1 The acceleration of charged particles

The purpose of particle accelerators is to accelerate charged particles to kinetic energies sufficiently high to produce nuclear reactions. The particles most often used for acceleration are electrons and nuclei of light elements, such as protons, deuterons, tritons and alpha particles. In practice the method for accelerating charged particles in low energy accelerators is to use an electric field in the proper direction. Different types of accelerators differ essentially in the way this field is produced.

The structure of a particle accelerator can be represented schematically by a diagram such as that of Fig. 2.1.1. There are three fundamental components: the ion source, the acceleration chamber under high vacuum, and the target. The operation of an accelerator then consists of the following sequence of phases. The particles are injected into the machine from an "ion source". Then the particles, collimated into a beam, follow a certain trajectory under the action of an accelerating electric field until they have reached the required energy, i.e. potential energy converted to kinetic energy. At this moment the beam is directed to hit a "target" where the desired nuclear reactions occur.

In evaluating the performance of a particle accelerator with reference to work on activation analysis the following points are considered;

(1) Maximum energy of the particle

(2) Intensity of the beam

(3) Energy stability

(4) Energy Variation

(5) Type of particles accelerated

(6) Cost of the machine.

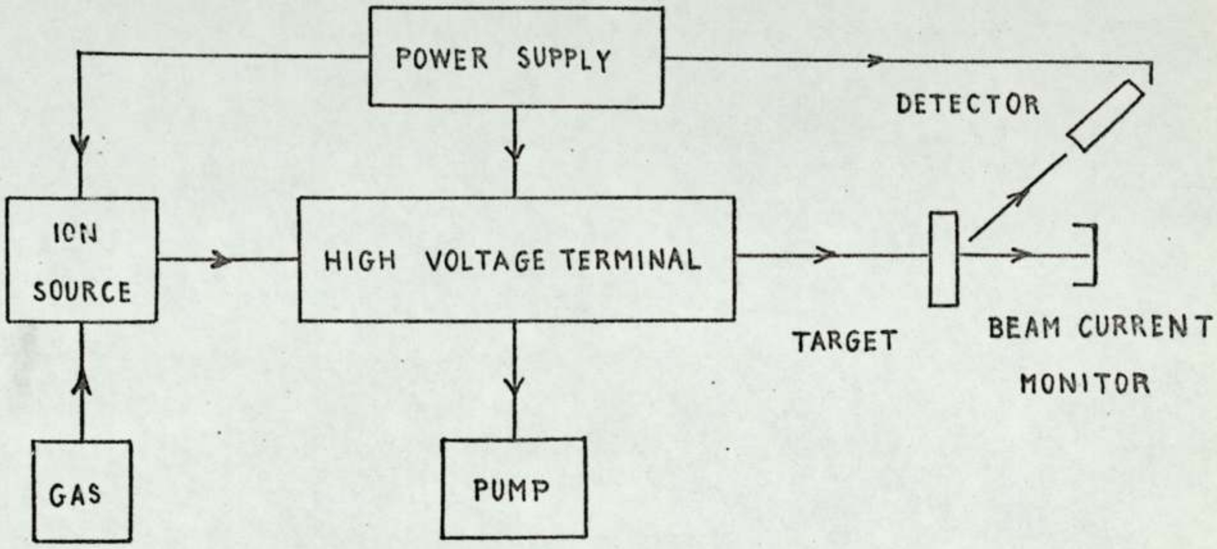

Figure 2.1.1 Structure of particle accelerator

Low energy electrostatic accelerators are perhaps the most widely used machines as far as application to elemental analysis is concerned. The characteristic of each type with respect to the above considerations are discussed in details in the following sections.

## 2.2 Low energy electrostatic accelerators

Electrostatic accelerators are those machines in which the particles are accelerated by applying a voltage difference (7), constant in time, whose value determines the final energy of the particles. The high voltages are obtained through the movement of electric charges. A particle with charge Z times that of the electron, after travelling through a potential difference of V volts, will have a kinetic energy of ZV electron volts*.

The maximum energy obtainable with this sort of machine is limited by the discharges that occur between the high voltage terminal and the walls of the surrounding chamber when the electric field at the surface of the electrode is greater than a certain value. The sparking field in dry air at atmospheric pressure is known by experiment to be 30 KV/cm, the corresponding figure for dry nitrogen at 16 atm. is 200 KV/cm. Working in dry air at atmospheric pressure this sort of accelerator could not be operated at voltage higher than 3 MV. By enclosing the entire machine in a high pressure tank filled with an inert gas, for example, freon ($CCl_2F_2$) at a pressure of 10-15 atm. the maximum voltage could be increased to 8 MV.

---

*One electron volt is the energy required by an electron when it is accelerated by a potential difference of 1 volt. The electron acquires an energy of $E = 1.602 \times 10^{-12}$ erg.

The advantages of the electrostatic accelerators are their high beam intensity, high energy stability variable energy and good beam collimation. These facts together with relatively low cost of machines and installations have made them attractive tools for the production of radiations for activation analysis. Three types of accelerators widely used for elemental analysis in recent years are:-

1. the Van de Graaf accelerator
2. the Cock croft-Walton accelerator
3. the SAMES built accelerator

These electrostatic accelerators consist essentially of two parts, the high voltage generator and the accelerating tube. Different types of electrostatic accelerators have different types of generators where as the accelerating tube are practically the same.

### 2.2.1. The accelerating tube

The accelerating tube usually consists of a series of glass (or other insulating material) cylinders connected with vacuum tight seals to metallic electrodes between the sections of insulator. The electrodes are connected to a chain of very high value resistors so that a uniform distribution of potential is maintained along the tube. These electrodes protect the walls of the tube from the beam and so reduce the possibility of surface discharges. They also limit the accumulation of charge on the insulating walls which can produce electrostatic deflection of the beam. The early electrostatic accelerators built followed closely the design indicated in Fig. 2.2.1. (7)

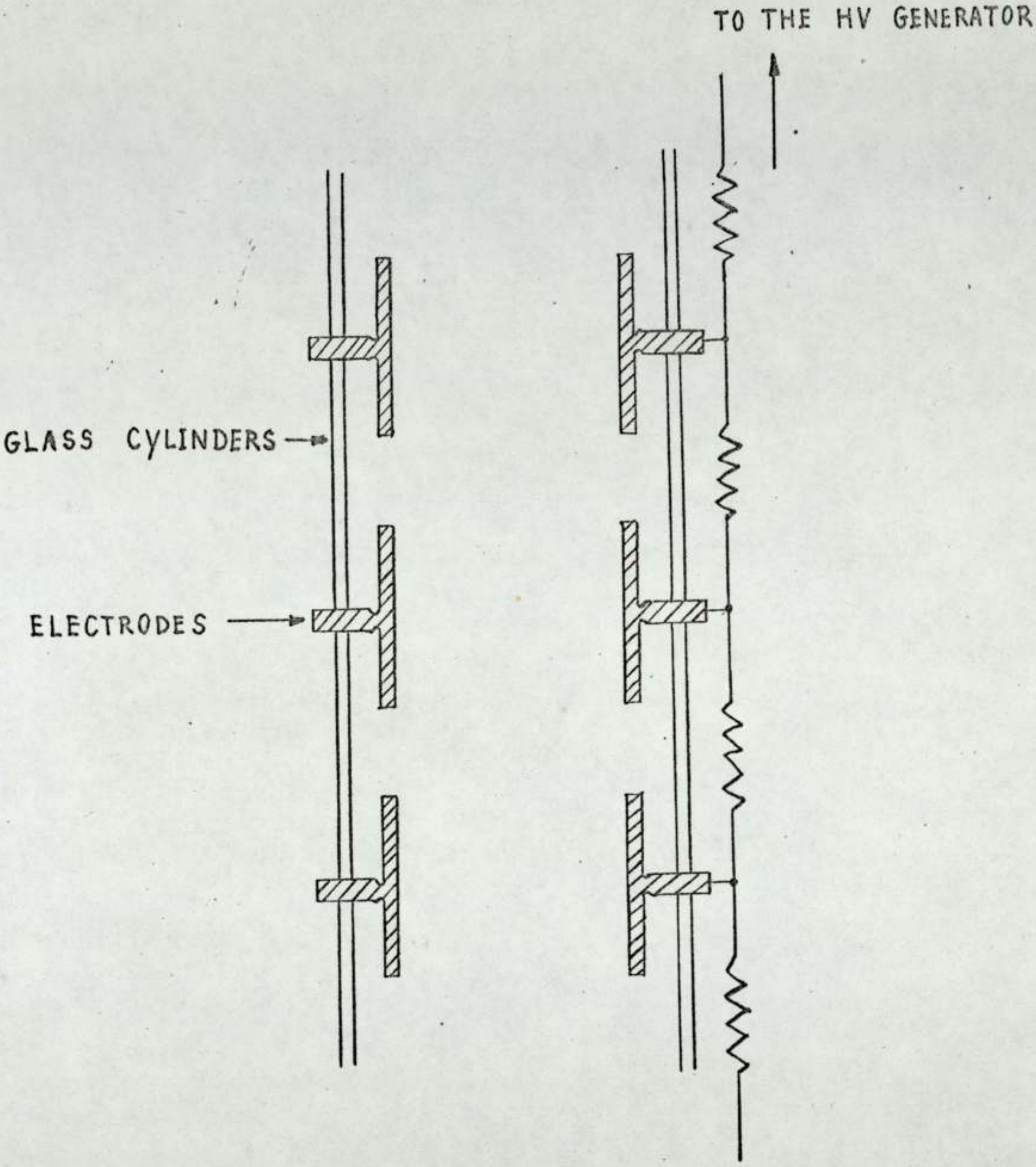

Figure 2.2.1 The accelerating tube

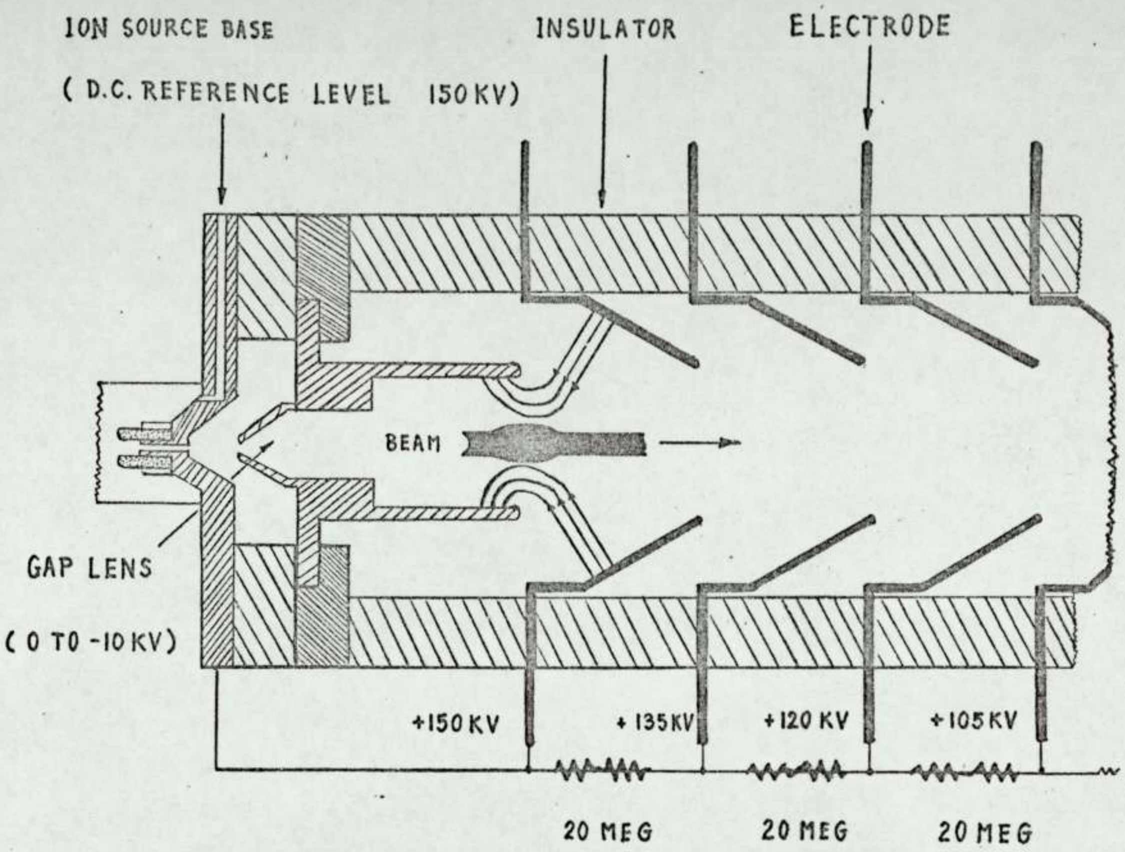

Figure 2.2.2 The 150 KV Neutron Generator accelerating tube

Fig. 2.2.2 is a schematic showing a gap lens and the first few sections of the accelerating tube of the 150 KeV Neutron Generator (6).

In the higher energy accelerators, the number of electrodes are increased by reducing the length of the intermediate ones so that they are practically reduced to metallic rings to withstand higher voltages. With this arrangement it is possible to maintain a uniform distribution of potential by means of the corona current flowing from one ring to the next. The inner diameter of the electrodes have been increased to allow higher pumping speed in view of the fact that modern ion sources giving higher intensities, produce a high flux of gas into the accelerating tube.

### 2.2.2. The high voltage terminal

Part of the electrostatic generator is the high voltage terminal where the problems of its design especially the problem of insulation are common to all type of generators. It usually consists of a metal shell of spherical or ellipsoidal shape to minimise the electric field at the surface for a given voltage, supported by one or more insulating columns. The ion source and the beginning of the accelerating tube are usually contained inside the terminal. The shape and dimension of the terminal are designed so that it can be charged to a high voltage without the occurance of discharges between it and the walls of chamber in which it is contained. For the same reason, the insulating columns are surrounded by closely spaced equipotential rings arranged so that the electric field is constant along the columns.

When the machine is working, the high voltage terminal is continuously supplied with electric charge from the electrostatic generator which feeds it.

### 2.2.3. The Van de Graaf generator

The method of providing high voltage by the use of a convective current to charge the high voltage terminal was first proposed by Van de Graaf (1). The design of the generator which bears his name is based on the principle that if a charged conductor is brought into internal contact with a hollow second conductor, all of its charges transfer to the hollow conductor no matter how high the potential of the latter may be. Except for insulation difficulties, the charge and hence the potential, of a hollow conductor could be raised to any desired value by successively adding charges to it by internal contact. The total charge Q in a conductor and its voltage V with respect to other conductors are related by the expression:

$$V = \frac{Q}{C} \qquad (2.2.1)$$

C = the capacity of the system, depends solely upon the geometrical distribution of the conductors and the dielectric properties of the insulators.

Eq. 2.2.1 implies that the voltage will take the value whenever the charge Q is forced into the conductor, the means by which the charged is carried is in principle immaterial. The Van de Graaf uses a convey or belt of insulating material for this purpose (Fig. 2.2.3)

The machines consist essentially of a belt of insulating material running between two rotating pulley. Near the lower pulley a set of sharp needles extends across the width of the belt and is maintained at a voltage of 20 to 30 KV with respect to

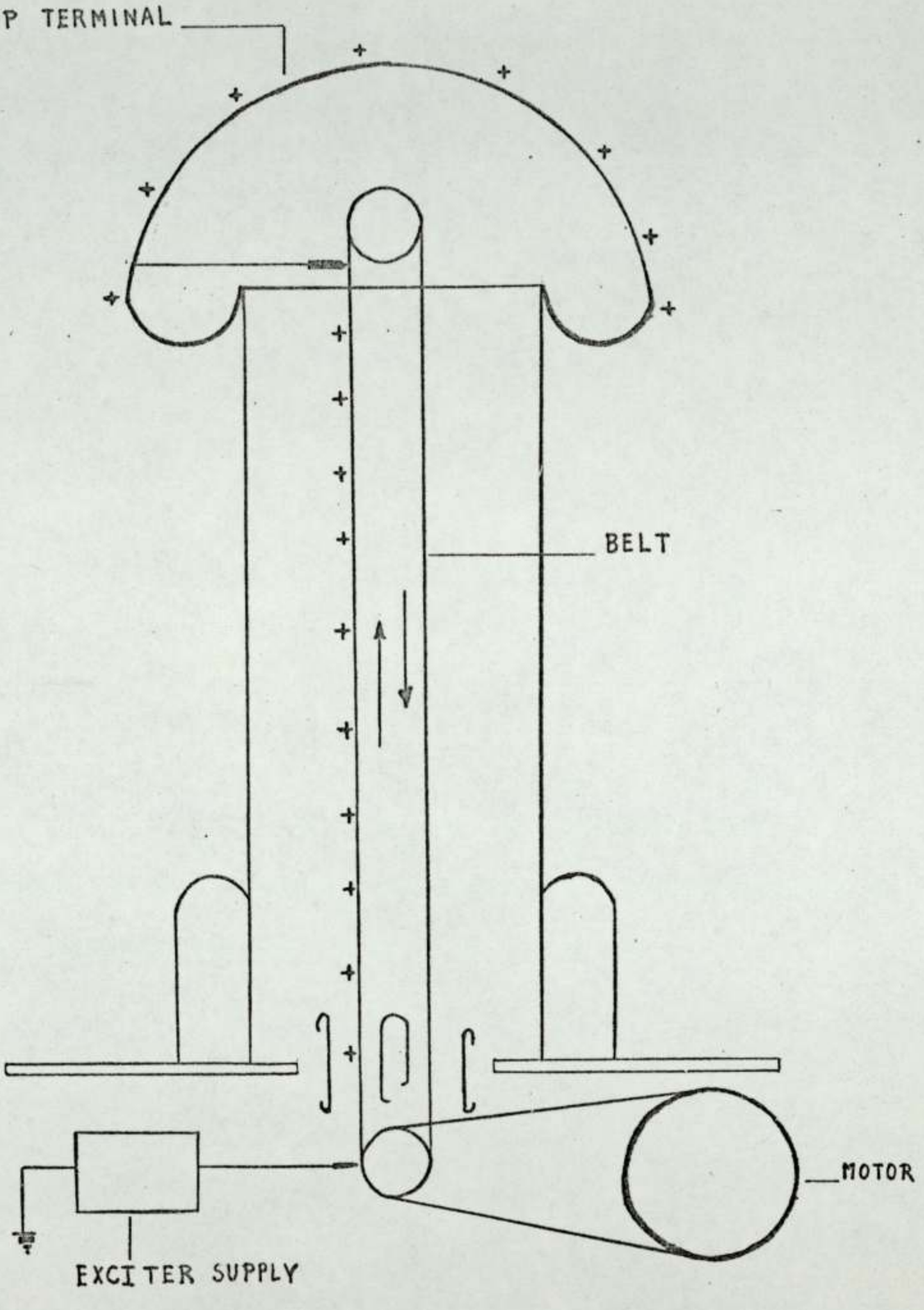

Figure 2.2.3 The Van de Graaf generator

to ground. A resulting corona discharge between the needles and the belt causes the electric charge to be deposited on the moving belt and transported towards the upper pulley. Another corona-point collector removes the charge carried by the belt; this charge accummulates progressively on the outer surface of the terminal and the voltage increases until the rate of loss of charge by leakage equals the rate at which charge is introduced.

The maximum voltage reached is limited by corona loss and voltage break down to neighbouring objects as already mentioned. Higher energy can be obtained by enclosing the apparatus in a gas tight steel chamber and operating at pressure up to about 15 atmospheres.(8)

The charging current, $i_m$, is determined by the characteristic of the belt and is given by

$$i_m = p\,v\,a \qquad (2.2.2)$$

where, p = surface charge density

v = speed of the moving belt

a = width of the belt

The values of p, v and a are in general limited by practical considerations. Usually v and a are less than 25 m/sec. and 50 cm. respectively. The value of p is limited by gas break down and higher value can be obtained when the belt is inside a high pressure tank. For example it is of the order of $10^{-4}$ coul/m$^2$ against $10^{-5}$ coul/m$^2$ at atmospheric pressure.

The 'single-stage' Van de Graaf accelerators reached an economic limit at about 6 MeV. By making the accelerated particle change the sign of its charge during the acceleration process twice the energy (12 MeV) was obtained in the first two-stage tandem accelerator. (9) The three-stage tandem accelerator (10) used a single-ended negative polarity 8 MeV Van de Graaf feeding a horizontal 12 MeV tandem Van de Graaf to obtain a 20 MeV protons.

### 2.2.4. The Cockcroft-Walton Generator

As in the Van de Graaf machine, high voltages are obtained in the Cockcroft-Walton generator through the movement of electric charges. It is a condenser-rectifier voltage multiplier based on the principle illustrated in Fig. 2.2.4.

The generator consists essentially of two columns of capacitors connected in series; the two columns are connected by a chain of diodes*which conduct only in the direction of the arrows. The generator is fed by a transformer T, capable of producing an a.c. voltage,Vct, with peak value V (order of magnitude of 100 KV).

Initially when no current is drawn from the HV terminal, a stationary state is reached where all the capacitors (except the first one) are charged to a voltage 2V. The potentials of the plates of the capacitors on the right are fixed, where as those of the capacitors on the left oscillates between the limit indicated in the diagram. In these conditions the diodes do not conduct any current. If this state is altered, the diodes (for some fraction of the period) conduct a current which tends to bring back the system to the stationary state.

---

*These are now replaced by solid state rectifiers.

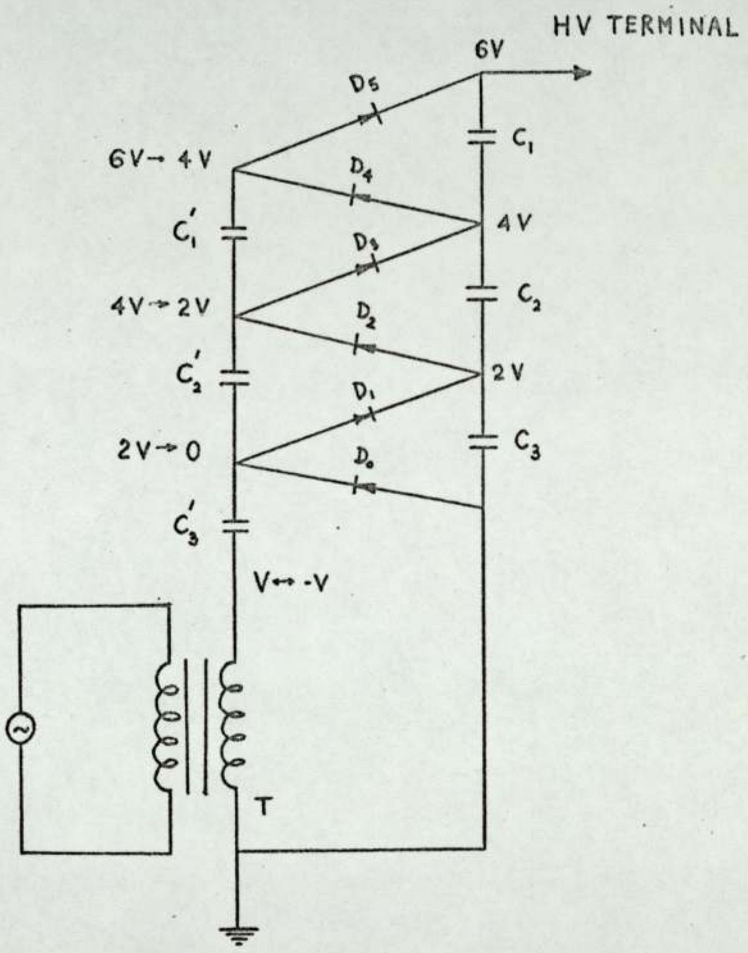

Figure 2.2.4 The Cockcroft-Walton generator

In practice during the operation of the machine a constant current is drawn from the HV terminal. Such current is always drawn by the accelerated ions, corona effect, insulator leakage and a high-voltage resistor used as a voltage divider for measuring purposes. The steady current drained implied a steady discharge of the condensers and the voltage therefore drops steadily until the condensers are charged again. At this moment it increases suddenly, and the whole process repeats itself. The voltage is not exactly constant, but oscillates between a maximum and minimum value. For n stages generator with all condensers having the same capacity, C, except the first one which is 2C, operated at a frequency, f, and delivers a current, I, the voltage oscillates between the values (11).

$$V\ \max = 2nV - \frac{2n^3}{3}\frac{I}{fC} \qquad (2.2.3)$$

$$V\ \min = V\ \max - \frac{1}{2}n(n+1)\frac{I}{C} \qquad (2.2.4)$$

By differentiating Eq. (2.2.3) a maximum value of n is reached for

$$n = \left(\frac{VfC}{I}\right)^{\frac{1}{2}} \qquad (2.2.5)$$

Unlike the Van de Graaf, the limitation of the Cockcroft-Walton machines are of a technological nature since there is a maximum voltage that the rectifier, condenser and transformer can stand. Present day selenium rectifiers set a practical limit for V around 100 KV, which is also typical of available transformers. Nevertheless the machine is relatively simple with no moving part. The maximum energies which can be obtained are low compared to the Van de Graaf, but it provides fairly large currents at relatively constant voltage and is very useful for experimental work below 1 MeV.

### 2.2.5. The 'SAMES*' Generator

The 'SAMES' is based on the principle that an electric charge placed in a field is subjected to a force. If the charge is mechanically displaced in a direction opposite to this force, the potential of the charge will increase and the mechanical work done will be converted into electrical energy. The essential parts of the machine are shown schematically in Fig. 2.2.5.

It consists of a hollow cylinder, called Rotor, made of insulating material. Electric charges are deposited on the surface of the rotor which is driven by an electric motor to effect the transfer of charges in the field. The mechanism of deposition and extraction of the ionic charges is accomplished by extremely thin metallic blades, called Ionizers, placed in close proximity to the rotor. A strong electric field is induced on the sharp edge of the ionizers by means of inductors which are usually held at high potential with respect to ionizer about 30 KV. This is in practice done by an auxilary "excitation generator". Excitation inductors hold the electric charges on the rotor, where as the extracting inductors withdraw them. The rotor passes successively opposite the charging and discharging ionizer where the rotor is respectively charged and discharged. These operations can take place once or several times per revolution.

The whole system is contained in an air-tight reservior of

---

*Sociéte Anonyme de Machines E'lectrostatiques

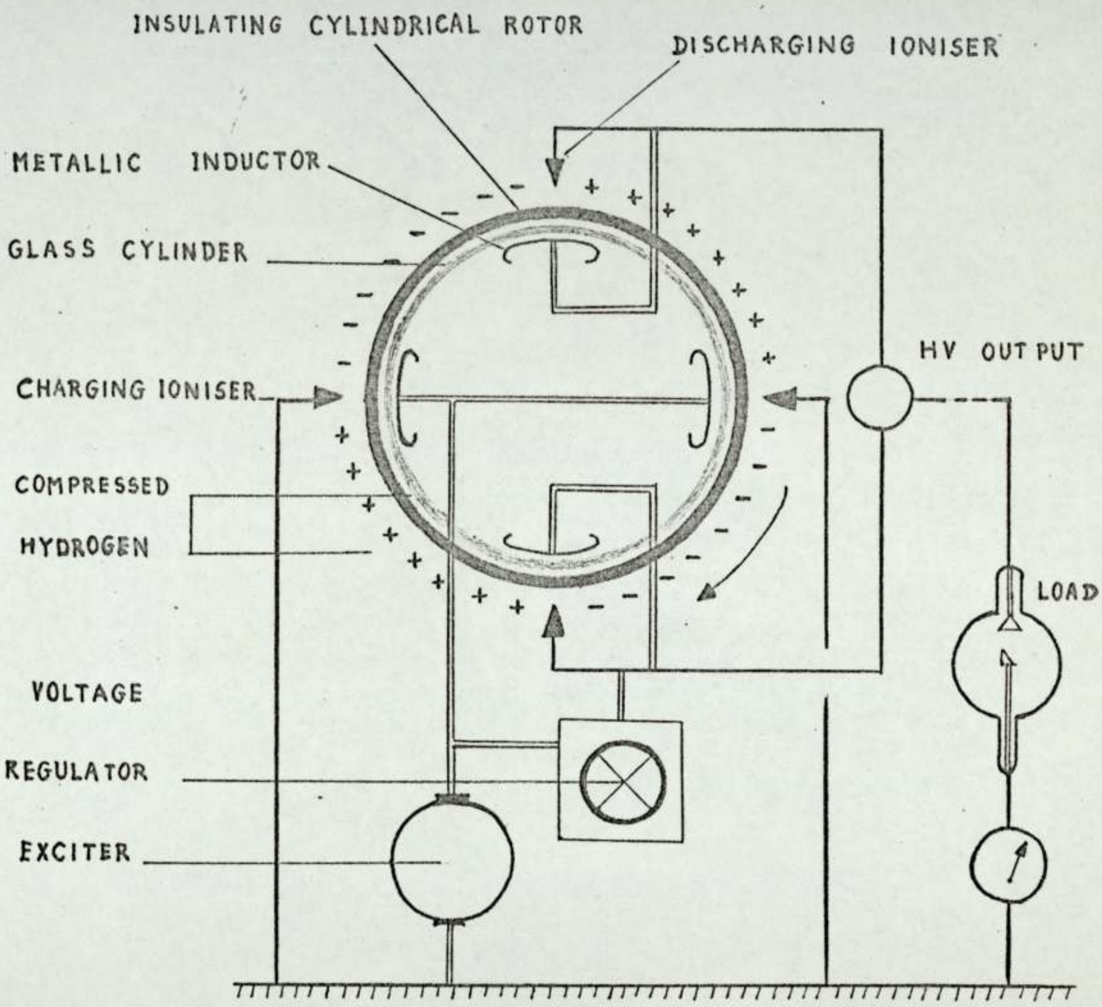

Figure 2.2.5 The "SAMES" generator

of extra pure hydrogen and a pressure of 10 to 25 atmosphere. The use of hydrogen as a dielectric assures excellent insulation while at the same time providing good commutation.

The maximum obtainable voltage with a single generator is between 600 KV and 1000 KV with an output currents of 15 MA. The distinctive feature of the SAMES is its light weight and small size in comparison with the available power and voltage and the resulting perfect direct current without the residual ripple present in rectifier system as obtained from the Cockcroft-Walton machine.

## 2.3. Accelerator neutron source

These accelerators can be used to produce neutrons. In all of these neutron generating machines, a charged particle is accelerated to an appropriate energy and allowed to strike a target which produces neutrons. Two kinds of neutron producing reaction are available at these energies; those from positive ion bombardment and those from electron bombardment.

### 2.3.1. Electron Bombardment

To produce neutrons by electron bombardment, the electron beam from an accelerator produces X-rays from a high atomic number target, such as $^{124}$Sb. X-rays in turn yield neutrons through electro magnetic interactions with nuclei. The following reactions are the most useful (12).

$^{9}Be(\gamma,n)^{8}Be$ : threshold energy 1.66 MeV
$^{2}H(\gamma,n)^{1}H$ : threshold energy 2.20 MeV
$$\left.\begin{array}{l} ^{nat}U(\gamma,n)U \\ ^{235}U(\gamma,f)U \end{array}\right\} : \text{threshold energy} \quad 9 \text{ MeV}$$

These reactions yield neutrons with several energies in a board continuous spectrum, packed in the 1-2 MeV region. The electrons must have an energy greater than the lowest threshold energy for the production of photo neutrons from the above reaction.

## 2.3.2. Neutron-producing reaction

The energy of a fast neutron resulting from positive ion bombardment is a function of the nuclear reaction in the target, the energy of the incident particle and the angle at which the neutron is emitted from the target.

The reactions often used to produce neutrons from positive ion bombardment are summarized in Fig. 2.3.1.

| Reaction | *Threshold (MeV) | @Q(MeV) | Neutron energy at threshold | |
|---|---|---|---|---|
| $D(d,n)^3He$ | | +3.266 | 2.448 | MeV |
| $T(p,n)^3He$ | 1.019 | -0.764 | 63.9 | KeV |
| $T(d,n)^4He$ | | +17.586 | 14.046 | MeV |
| $^9Be(\alpha,n)^{12}C$ | | +5.708 | 5.266 | MeV |
| $^{12}C(d,n)^{13}N$ | 0.328 | -0.281 | 3.4 | KeV |
| $^{13}C(\alpha,n)^{16}O$ | | +2.201 | 2.07 | MeV |
| $^7Li(p,n)^7Be$ | 1.882 | -1.646 | 29.9 | KeV |

(13)

Figure 2.3.1. Energy characteristics of Neutron Source

*Threshold: The threshold is the minium kinetic energy of the bombarding particle which is just sufficient to produce a reaction.

@Q: The Q value is the energy associated with the nuclear transformation.

The yield of neutron per second from various reactions is a function of several interrelated factors. Factors affecting the yield can be summarized as follows:-

1. Nuclear reaction used
2. Energy of bombarding particle
3. Intensity of bombarding beam
4. Target deterioration due to intense heat generated
5. Beam characteristics with regard to spread, purity and stability

The yield and energy of neutron from the $T(d,n)^4He$ reaction is considered in more details in Section 3.2 in view of its important application to the developing field of fast neutron activation analysis.

### 2.3.3. Characteristics and installation cost of low energy accelerators

The choice of an accelerator for neutron production is also involved with such factors as cost of equipment, installation and operation as well as the flexibility of application to problems other than neutron activation analysis such as the range of beam energy of charged particle for other types of analysis. Regardless of the type of accelerator used, the nuclear reaction is more or less the controlling factor influencing the neutron yield and energy.

The very high Q value, of the $T(d,n)^4He$ reaction makes possible the production of fast neutrons with relatively low input energy. The accelerators discussed in Section 2.2 have the advantage of producing fast (14 MeV) neutrons of fluxes sufficiently high for all but the most sensitive neutron activation analysis. These fast neutrons can be slowed down; producing thermal neutron by passing the neutrons through a block of paraffin wax.

Fig. 2.3.2. indicates how various types of low energy accelerators are compared.

## 2.4. Activation analysis with 14 MeV neutrons

In recent years significant progress has been made in the design of low cost charged particle accelerators capable of producing considerable high yield of fast (14 MeV) neutrons using the reaction $T(d,n)^4He$. This development has greatly increased the scope of neutron activation analysis. Although the flux is much lower than that of a reactor, the energy of neutron is 14 MeV and neutrons at this energy are appropriate for $(n,p)$, $(n,\alpha)$ and $(n,2n)$ reactions. These cross sections are generally considerably lower than those of $(n,\gamma)$ reaction with thermal neutrons. The combination of lower flux and smaller cross section results in diminished sensitivity for fast neutron activation analysis.

Another factor which has to be taken into account when using this technique is the interfering reactions. When a certain element is bombarded with fast neutron, usually more than one reaction can occur simultaneously. For example, in the analysis of fluorine following reactions can occur with more or less the same probability;

| | cross section* |
|---|---|
| $^{19}F + n \rightarrow {}^{18}F + 2n$ | 60 mb |
| $\searrow {}^{19}O + p$ | 130 mb |
| $\searrow {}^{16}N + \alpha$ | 50 mb |

---

*1 barn = $10^{-24} cm.^2$

Figure 2.3.2.(11) Various types of low energy electrostatic accelerators

| Installation | Manuf-acturer | Beam Energy* Range (MeV) | Max.Aver Beam Current (ma) | Max.Aver Neutron Yield (n/sec.) | Installa-tion Cost (£$10^3$) |
|---|---|---|---|---|---|
| TYPE L | SAMES | 0.1-0.3 | 0.5 | $2 \times 10^{10}$ | 13.6-15.2 |
| TYPE J |  | 0.05-0.15 | 0.5 | $6 \times 10^{9}$ | 8.4 |
| TYPE S |  | 0.1-0.6 | 0.5 | $2 \times 10^{11}$ | 21.7-24.6 |
| VDG AN-400 | HEVC | 0.2-0.4 | 0.15 | $2 \times 10^{10}$ | 8 |
| VDG KN-500 |  | 0.1-0.5 | 1.5 | $2 \times 10^{11}$ | 28.8 |
| VDG AN-1300 |  | 0.3-1.3 | 0.15 | $9 \times 10^{10}$ | 15.4 |
| COCKCROFT-WALTON | TNC | 0-0.15 | 1 | $4 \times 10^{10}$ | 8.4 |
| COCKCROFT-WALTON |  | 0-0.15 | 1.5 | $4 \times 10^{10}$ | 8.5 |
| COCKCROFT-WALTON |  | 0-0.1 | 1 | $1.7 \times 10^{10}$ | 8.2 |
| COCKCROFT-WALTON |  | 0-0.1 | 1.5 | $1.7 \times 10^{10}$ | 8.5 |
| DYNAMITRON PA-1 | RDI | 0.1-1 | 10 | $10^{12}$ | 35.2 |
| DYNAMITRON DY-3E |  | 0-0.2 | 10 | $1.5 \times 10^{12}$ | 23 |
| DYNAMAG DY-3D |  | 0-0.15 | 10 | $7 \times 10^{12}$ | 20 |
| DYNAMAG PA.1.5 |  | 0.15-1.5 | 10 | $5 \times 10^{12}$ | 38.4 |

*Beam Energy for singly charged particle

| | |
|---|---|
| SAMES | Societe Anonyme de Machines E'lectrostatiques. |
| HVEC | High Voltage Engineering Corp. |
| TNC | Texas Nuclear Corp. |
| RDI | Radiation Dynamics Inc. |

There is also an interfering reaction from $^{16}O(n,p)^{16}N$ reaction so that $^{16}O$ + $^{19}F$ produce the same nuclide. It is quite clear that the cross sections must be known so that the reaction which leads to minimum interference can be chosen. Neutron cross sections have been tabulated by Hughes and co-workers (14) (15) (16) in particular those of (n, 2n), (n,p) and (n, $\alpha$) reaction cross sections. These cross sections have been compiled specifically in the interest of activation analysis by the research staff of Texas Nuclear Corp.(6)

### 2.4.1. Sensitivities obtained with fast neutron activation analysis

In 1961 Coleman (17) and independently Gillespie and Hill (18) calculated the 14 MeV neutron activation analysis sensitivities based on the cross sections compiled by Hughes. The biggest drawback of these theoretical calculations lies in the uncertainty of cross section which are rarely know to pricise. In view of this uncertainty Perdijon (19) in 1967 has made an experimental sensitivity determination with 14 MeV neutrons using the 150 SAMES accelerator. His results normalised to a flux of $10^9$ n/cm.$^2$-sec. is shown in Fig. 2.4.1.

### 2.5. Charged particle analysis by method of prompt $\gamma$-ray detection

Charged particle activation analysis was applied by Seaborg and Livingood as early as 1938 before the advent of chain-reacting pile. This technique commanded little interest due to the fact that with the advent of nuclear reactors intense neutron fluxes became available which solved many analytical problems.

The nature of analysis is indeed complex through various practical problems which are frequently encountered. For example, the simultaneous occuring of nuclear reactions, limited range of

Figure 2.4.1. Optimum limits of detection for the elements under study*

| Limit of detection ($\mu$g) | Element | Interference | Limit of detection ($\mu$g) | Element | Interference |
|---|---|---|---|---|---|
| From 1 to 10 | Ag | Sb, In, Cl, Sn | From 10 to 100 | Cl | Zn, Sn |
| | Al | | | Cr | Mn |
| | Ba | Ag | | F | Pd, Ag |
| | Br | Cu, N, K | | Fe | Co |
| | Cd | | | Ge | As, Pd |
| | Cu | Br, Sb, N, In, K | | K | Br, Cu, N |
| | Ga | Cd, Se, Cr | | Mg | Al |
| | Hg | Cd, Cl, Sn | | Mo | Sb, In, Ag |
| | Sb | Ag, In, Mo | | N | Cu, Br, K |
| | Si | P | | Na | Mg |
| | Sr | | | O | F, B |
| | Zn | Cl, Sn, Se | | P | Si |
| | Zr | Sr | | Pd | |
| From 100 to 1000 | | | | Se | |
| | As | Ge, Pd | | Sn | Hg, Cd, Cl |
| | Au | | | Te | |
| | Np | | | W | Fe, Pd |
| | Ni | Cu | | | |
| | Pt | Au | From 1000 to 10000 | B | O, F |
| | Ta | | | Ca | Cl |
| | Ti | Se | | Pb | |
| | | | | S | Cl, B |

*Irradiation and Counting time = 4 half lives or maximum 20 min, decay time before counting 3 sec.

particles and heating of the bombarded samples.

In the case of low z elements, however, neutron activation analysis has limited applicability, for instance in the case of ultra high purity material. Charged particle activation analysis can supplement this technique or serve as an independent surface analysis technique where charged particles are very useful.

To overcome the coulomb barrier and to obtain sufficiently high reaction rates charged particles applied in activation analysis are almost exclusively light ones, i.e., protons, deuteron, $^{3}$He and $^{4}$He.

It has been suggested by Albert (21) at the recent conference on activation analysis with charged particles that the following energies should be available: proton: 5-25 Mev, deuteron: 5-25 MeV, $^{3}$He: 5-20 MeV and $^{4}$He: 10-45 MeV, hence the need for high energy accelerator.

In recent years there has been a growing interest in using low energy accelerators (section 2.2) for analysis of light elements by measurement of prompt $\gamma$-radiation. Because the energy and the yield of the $\gamma$-ray provides information about the type and number of nuclei present in the sample without radio-active nuclei being necessary as a product of the reaction, and the measurement of $\gamma$-radiation enables the determination to be carried out on the intact sample.

Several investigations have been carried out, (22) (23) (24) (25) but these have been largely concerned with the measurement of $\gamma$-lines excited by 2-3 MeV particles accelerated by the Van de Graaf. Reports on the analysis based on 0.5 MeV protons are rare (26)(27)

Fig. 2.5.1. $\gamma$-Yields from thick targets of some elements bombarded with 0.475 MeV protons. (26)

| Element | Target | Reaction | $\gamma$-ray energy $E_\gamma$, MeV | Sensitivity* c per p.p.m. per $10^5 \mu c$ |
|---|---|---|---|---|
| Be | 2% Be-Cu Alloy | $^{9}Be(p,\gamma)^{10}B$ | 0.72 | 24 |
| B | Be-Fe | $^{11}B(p,\gamma)^{12}C$ | 4.43 | 4.2 |
| C | C-Fe | $^{12}C(p,\gamma)^{13}N$ | 2.36 | 6.1 |
| F | $CaF_2$-Fe | $^{19}F(p,\alpha)^{16}O$ | 6.14 | 950 |
| Na | NaBr-Fe | $^{23}Na(p,\gamma)^{27}Al$ | 1.37 | 2.2 |
| Mg | Mg-Fe | $^{26}Mg(p,\gamma)^{27}Al$ | 0.84 + 1.01 | 2.5 |
| Al | Al-Fe | $^{27}Al(p,\gamma)^{28}Si$ | 1.79 | 0.3 |

*Sensitivity based on the detection of $\gamma$-rays by $3 \times 3$-inch NaI(Tℓ), 3.5 cm from the target at 90° angle of observation.

Fig. 2.5.1 summarized the results obtained by Pierce(26) and co-workers, using 0.5 MeV Cockcroft-Walton accelerator, of some light elements.

Piece has discussed the advantages and disadvantages of prompt $\gamma$-radiation method vis-a-vis conventional activation analysis in recent conference and considered the major limitations to be;(28)

1. The nuclei to be measured cannot be separated from all others by chemistry and therefore the analysis is purely instrumental.
2. As highly excited nuclear states are often produced decay may lead to very complex spectra.

This method is treated however in more detail in CHAPTER IV of this work concerning the analysis of fluorine.

# CHAPTER III NUCLEAR INSTRUMENTATIONS

### 3.1. The 500 KV electrostatic generator and ion accelerator

Throughout the course of the experimental work the accelerator used to provide high energy charged particle was a basic Van de Graaf accelerator, part of which was constructed in 1934 from drawings supplied by Van de Graaf. Originally it could supply a beam of 150 $\mu$A of resolved monatomic ions at energies up to 500 KeV. The general view of the accelerator is shown in Fig. 3.1.1.

The high voltage was measured by an eight vane generating voltmeter (20) which was mounted on the hemispherical casing and positioned as close as possible to the high voltage to be determined. The hemispherical casing is shown, supported from the wall in Fig. 3.1.1.

The operation of the complete machine was controlled from the mobile rack shown in Fig. 3.1.2. The control room was well shielded from high energy neutrons or $\gamma$-ray flux. (30)

### 3.2. The $T(d,n)^4He$ reaction

The $T(d,n)^4He$ is the best high-energy neutron producer for bombarding energies less than 1 MeV; it yields monoenergetic neutrons in the 10-16 MeV range. The J = 3/2 resonance in the compound nucleus $^5He$ which leads to the peak cross section of 5 barns at 110 KeV deuteron energy (Fig. 3.2.1) makes it convenient for the production of neutrons from the 500 KV accelerator set. An extensive bibliography of early work on this reaction has been given by Fowler and Brolley (31).

#### 3.2.1. Energy distribution of the $T(d,n)^4He$ neutrons

Let $E_d^{\cdot}$ = deuteron kinetic energy in the laboratory system

Figure 3.1

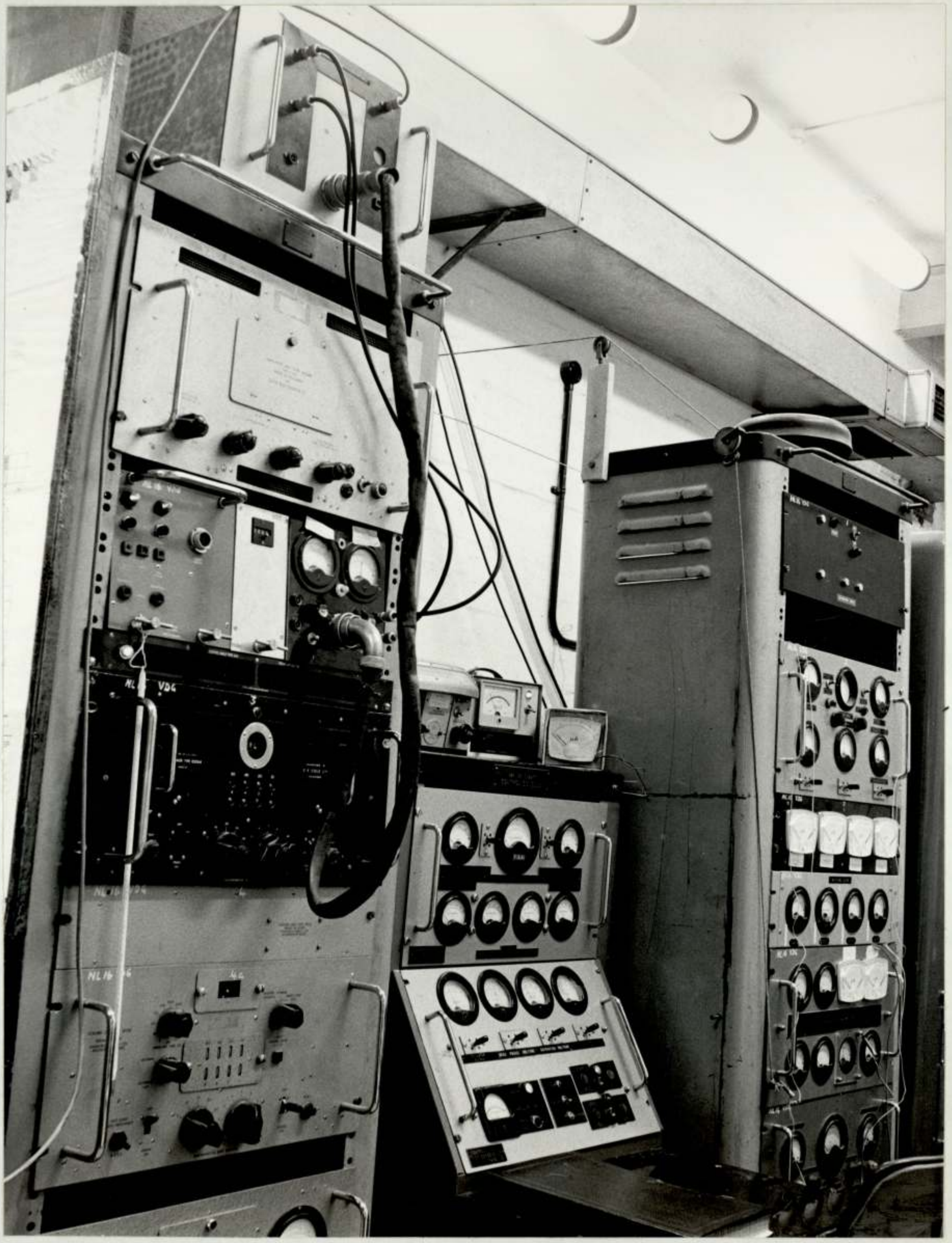

Figure 3.1.2

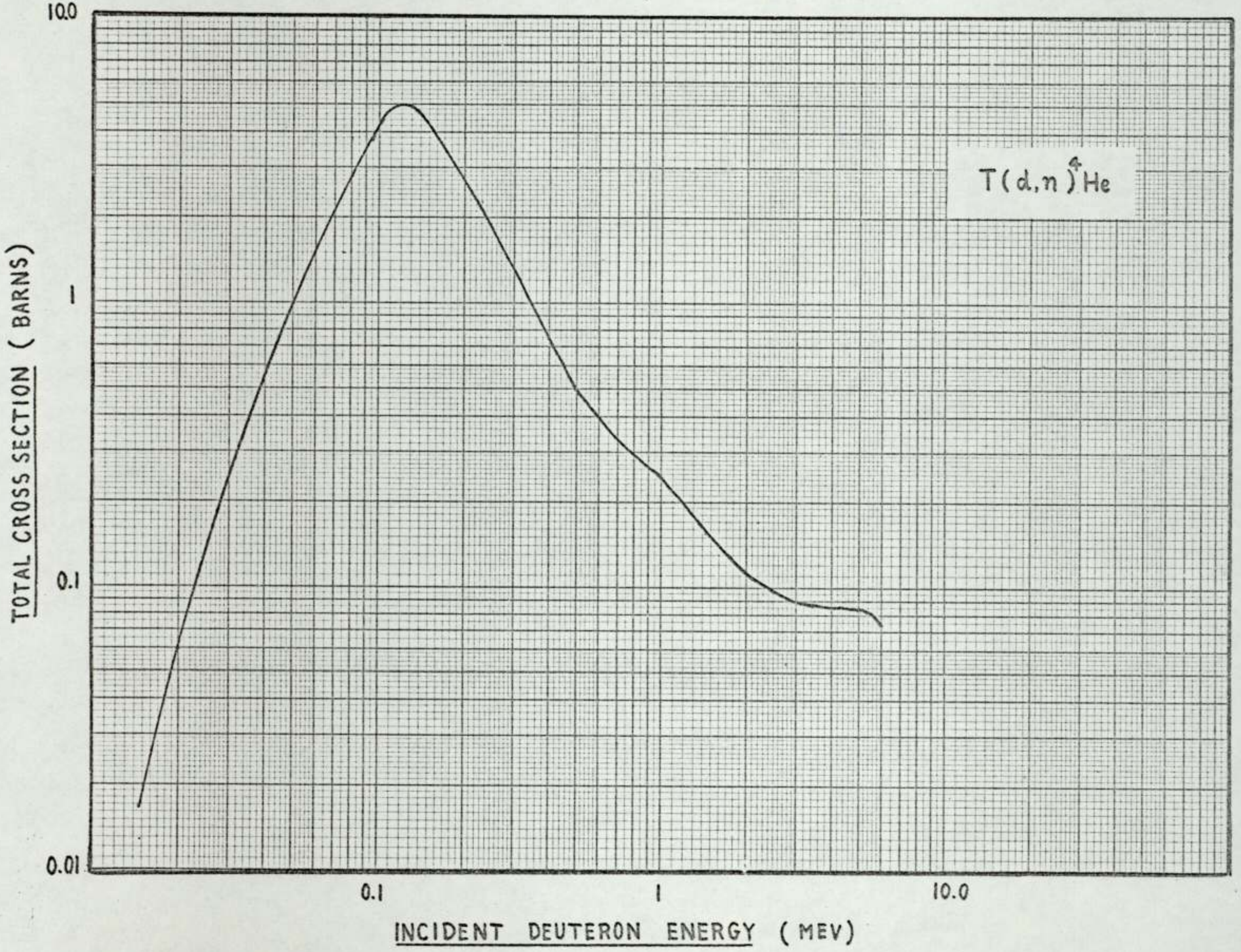

Figure 3.2.1 The T(d,n)$^{4}$He total cross section

$E_n$ = neutron kinetic energy in the laboratory system

$m_i$ = mass of particle i

$\phi$ = angle between the neutron and the deuteron

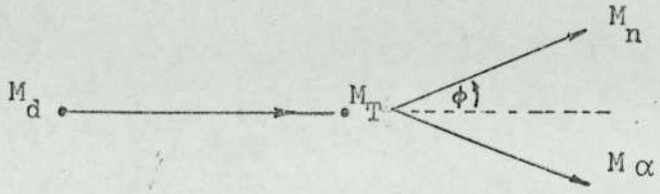

The general expression for the energy of neutron in the laboratory system may be written in the form (32)

$$E_n = \left( \frac{M_d}{M_d + M_T} \right)^2 \frac{M_n}{M_d} E_d \cos 2\phi + \frac{M_\alpha}{M_n + M_\alpha} \left( \frac{M_T}{M_d + M_T} E_d + Q \right) \tag{3.2.1}$$

$$\pm \frac{2 \cos \phi}{M_d + M_T} \sqrt{M_d M_n \frac{M\alpha}{M_n + M\alpha} \cdot E_d \left( \frac{M_T}{M_d + M_T} E_d + Q \right)} \cdot \sqrt{1 - \frac{M_d M_n}{M_d + M_T} \cdot \frac{E_d \sin^2\phi}{M_\alpha \Big( \frac{M_T}{M_d+M_T} E_d + Q}}$$

$$Q = M_n + M_\alpha - M_d - M_T$$

Using the mass values appearing in Segre chart we get

$$E_n = 0.08E_d \cos 2\phi + 0.8(0.6E_d + 17.6) + 0.8 \cos\phi \sqrt{0.4E_d(0.6E_d + 17.6)} \sqrt{1 - \frac{E_d \sin^2\phi}{10(0.6E_d + 17.6}} \tag{3.2.2}$$

$E_q$. (3.2.2) has been evaluated and the results are tabulated in Fig. 3.2.2. Fig. 3.2.3 is a system of curves representing the tabulated data. If the tritium target is "thick" (relative to range of the incident deuterons) deuterons of all energies from the bombarding energy to zero will yield neutrons. The energy spread of neutrons to be found at any angle $\phi$ may be found from Fig. 3.2.3 by measuring the energy spread between the curves for $E_d$ = bombarding energy and $E_d = 0$.

Figure 3.2.2. Neutron Energy VS Lab Angle For Deuteron Bombarding Energy $E_d$

| $\phi$ (LAB) | Deuteron energy (MeV) | | | | | |
|---|---|---|---|---|---|---|
| | 0.0 | 0.1 | 0.2 | 0.3 | 0.4 | 0.5 |
| 0 | 14.080 | 14.808 | 15.144 | 15.417 | 15.655 | 15.874 |
| 10 | 14.080 | 14.797 | 15.129 | 15.398 | 15.632 | 15.849 |
| 20 | 14.080 | 14.766 | 15.083 | 15.340 | 15.566 | 15.774 |
| 30 | 14.080 | 14.714 | 15.009 | 15.248 | 15.458 | 15.650 |
| 40 | 14.080 | 14.644 | 14.908 | 15.123 | 15.312 | 15.486 |
| 50 | 14.080 | 14.546 | 14.785 | 14.971 | 15.134 | 15.286 |
| 60 | 14.080 | 14.460 | 14.644 | 14.795 | 14.931 | 15.056 |
| 70 | 14.080 | 14.352 | 14.490 | 14.605 | 14.710 | 14.806 |
| 80 | 14.080 | 14.238 | 14.326 | 14.404 | 14.485 | 14.544 |
| 90 | 14.080 | 14.120 | 14.166 | 14.200 | 14.240 | 14.280 |
| 100 | 14.080 | 14.004 | 13.996 | 13.998 | 13.999 | 14.020 |
| 110 | 14.080 | 13.892 | 13.838 | 13.807 | 13.786 | 13.772 |
| 120 | 14.080 | 13.788 | 13.692 | 13.629 | 13.581 | 13.544 |
| 130 | 14.080 | 13.695 | 13.561 | 13.445 | 13.398 | 13.340 |
| 140 | 14.080 | 13.614 | 13.450 | 13.333 | 13.244 | 13.168 |
| 150 | 14.080 | 13.550 | 13.359 | 13.224 | 13.118 | 13.030 |
| 160 | 14.080 | 13.502 | 13.293 | 13.144 | 13.026 | 12.974 |
| 170 | 14.080 | 13.473 | 13.253 | 13.096 | 12.972 | 12.867 |
| 180 | 14.080 | 13.464 | 13.243 | 13.079 | 12.953 | 12.819 |

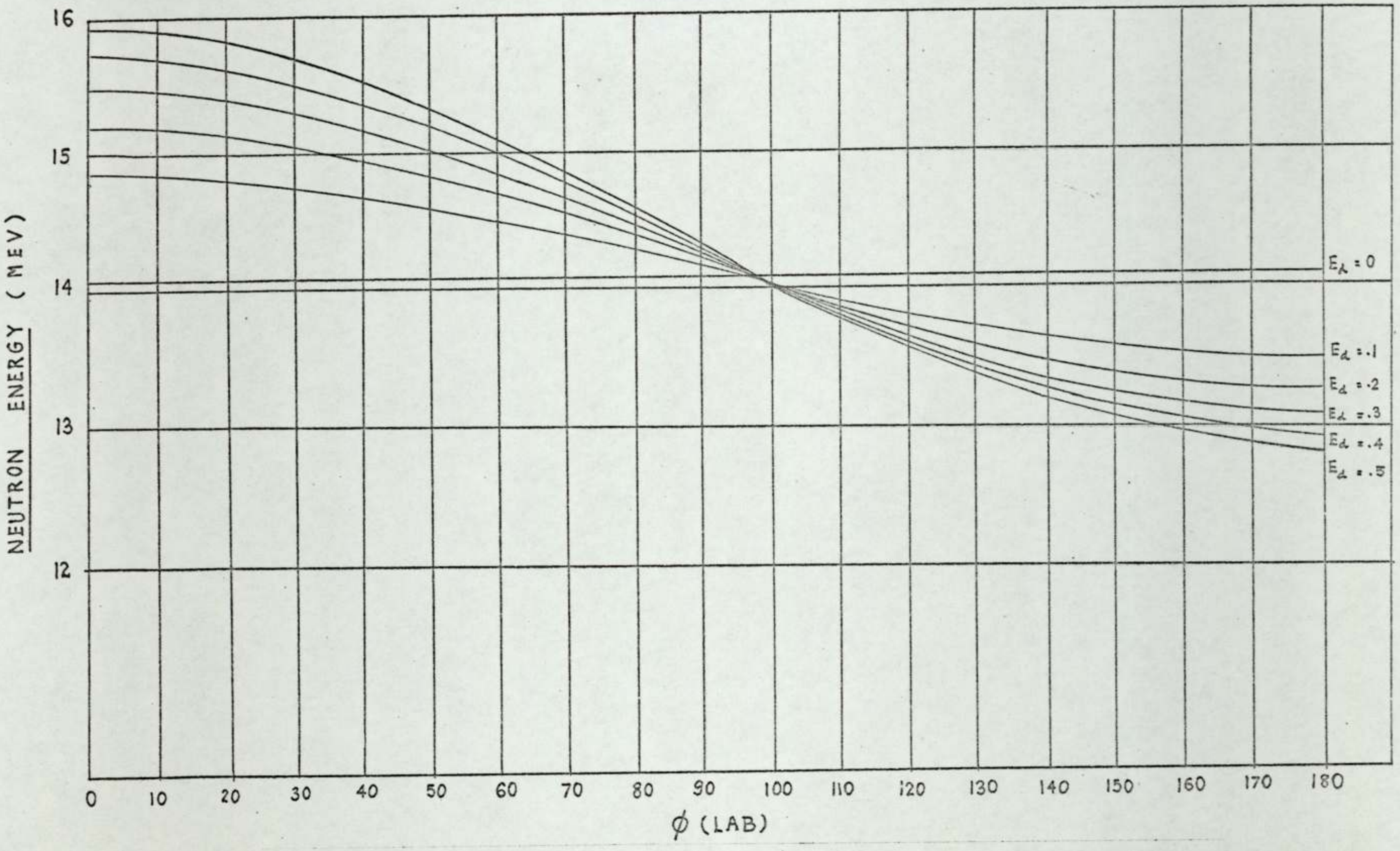

Figure 3.2.3 Plot of neutron energy VS laboratory angle for deuteron energy $E_d$

### 3.2.2. Angular distribution of the $T(d,n)^4He$ neutrons

For any nuclear reaction the yield of the out going particle at any angle $\phi$ is referred to as the differential yield and expressed as the number of particle emerging into a solid angle about $\phi$. The differential yield per unit solid angle, $Y_\phi$, may be expressed simply as

$$Y_\phi = \left(\frac{d\sigma}{d\omega}\right)_\phi N_1 N_2 \qquad (3.2.3)$$

where $\frac{d\sigma}{d\omega}$ = differential cross section, barns per steradian

$N_1$ = number of target nuclei

$N_2$ = number of particle hit targets per $cm^2$ per sec.

Eq. (3.2.3) shows the dependence of the differential yield on the differential cross section. The angular dependence of the differential cross section has been found to be essentially isotropic to 200 KeV by Allan and Poole (33) and to 570 KeV by Argo etal. (34) in the C.M. system. The transformation into the laboratory system of the differential cross section introduces the anisotropy in the yield of the neutron as shown in the following equation

$$Y_\phi = \left(\frac{d\sigma}{d\omega^1}\right)\left(\frac{d\omega^1}{d\omega}\right)_\phi N_1 N_2 \qquad (3.2.4)$$

where $d\omega^1$ = solid angle in the C.M. system.

The $\frac{d\omega^1}{d\omega}$ ratio can be calculated from the kinematics of the reaction. Fig. 3.2.4 tabulates the results obtained by Benveniste and Zenger. (32)

Figure 3.2.4. Ratio of $\left(\frac{dw^1}{dw}\right)$ of neutron solid angles for deuteron energy $E_d$

| $\phi$ (LAB) | Deuteron energy (MeV) | | | | |
|---|---|---|---|---|---|
| | 0.1 | 0.2 | 0.3 | 0.4 | 0.5 |
| 0 | 1.0483 | 1.0684 | 1.0837 | 1.0969 | 1.1085 |
| 10 | 1.0476 | 1.0674 | 1.0823 | 1.0954 | 1.1068 |
| 20 | 1.0454 | 1.0642 | 1.0784 | 1.0908 | 1.1016 |
| 30 | 1.0417 | 1.0590 | 1.0720 | 1.0834 | 1.0933 |
| 40 | 1.0368 | 1.0520 | 1.0634 | 1.0734 | 1.0820 |
| 50 | 1.0308 | 1.0435 | 1.0528 | 1.0611 | 1.0683 |
| 60 | 1.0239 | 1.0336 | 1.0407 | 1.0470 | 1.0525 |
| 70 | 1.0163 | 1.0227 | 1.0274 | 1.0316 | 1.0352 |
| 80 | 1.0082 | 1.0113 | 1.0133 | 1.0154 | 1.0171 |
| 90 | 0.999 | 0.9996 | 0.9990 | 0.9988 | 0.9986 |
| 100 | 0.9917 | 0.9880 | 0.9848 | 0.9825 | 0.9804 |
| 110 | 0.9837 | 0.9768 | 0.9712 | 0.9669 | 0.9629 |
| 120 | 0.9763 | 0.9664 | 0.9586 | 0.9523 | 0.9468 |
| 130 | 0.9696 | 0.9571 | 0.9472 | 0.9394 | 0.9324 |
| 140 | 0.9639 | 0.9491 | 0.9376 | 0.9283 | 0.9201 |
| 150 | 0.9593 | 0.9426 | 0.9298 | 0.9194 | 0.9102 |
| 160 | 0.9559 | 0.9379 | 0.9240 | 0.9128 | 0.9030 |
| 170 | 0.9538 | 0.9350 | 0.9206 | 0.9088 | 0.8986 |
| 180 | 0.99531 | 0.9340 | 0.9194 | 0.9075 | 0.8971 |

Figure 3.2.5 Plot of ratio $\left(\frac{dw^1}{dw}\right)$ of neutron solid angles for deuteron energy $E_d$

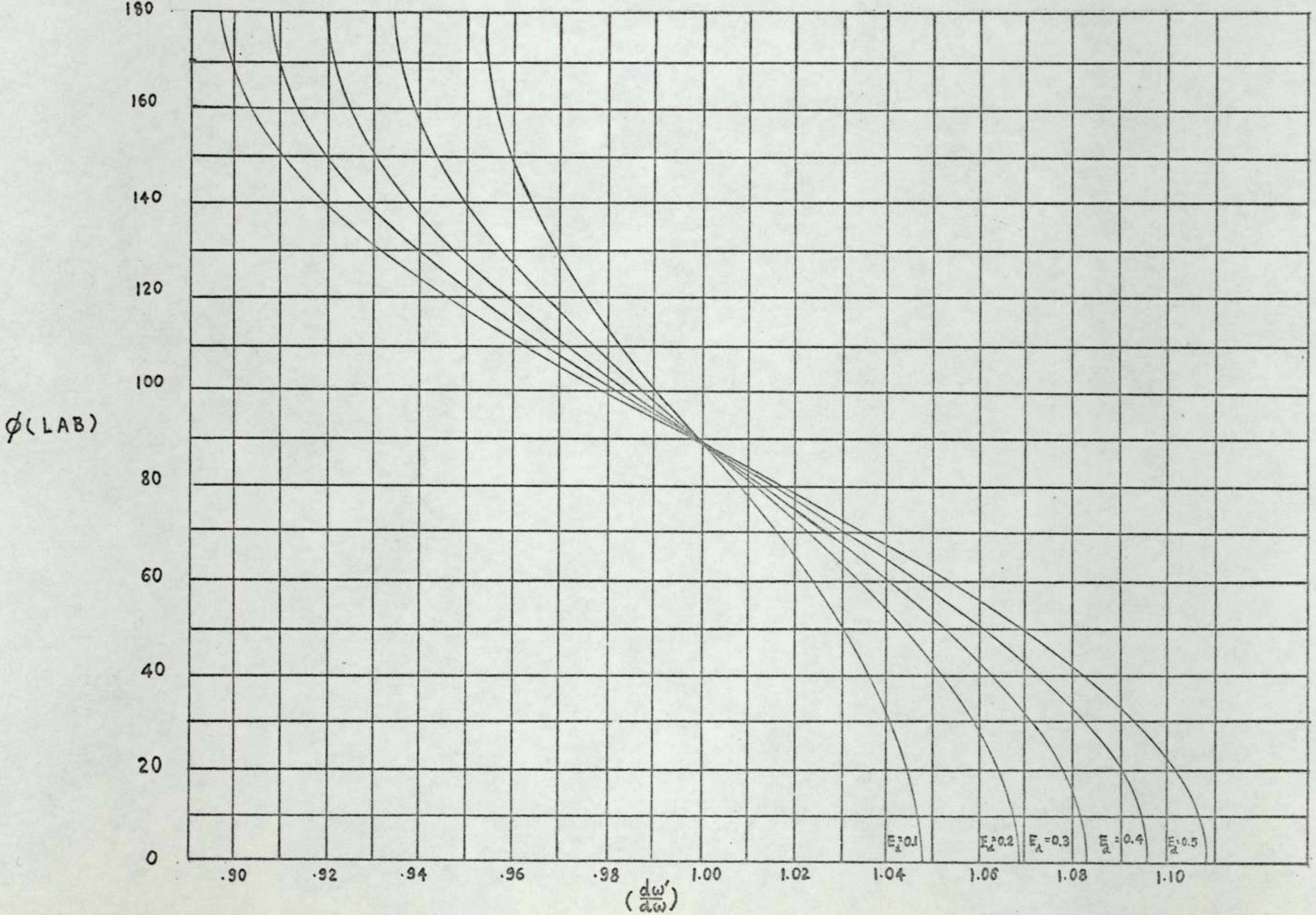

### 3.2.3. Total yield from the $T(d,n)^4He$ reaction

Since the angular dependence of the differential cross section has been found to be essentially isotropic up to 570 KeV, the total thick target yield of neutron per incident deuteron of energy E is given by

$$Y = \int_0^E \frac{4\pi n_t \, d\sigma/d\omega}{d\epsilon/dx} \, d\epsilon \qquad (3.2.5)$$

$n_t$ = the number of tritium nuclei/cm$^3$.

$\frac{d\sigma}{d\omega}$ = the differential cross section for the $T(d,n)He^4$ reaction

$\frac{d\epsilon}{dx}$ = the rate of energy loss of deuterons of energy $\epsilon$ in the $T_i$-T targets.

Assuming a loading factor of one tritium per titanium atom Benveniste and Zenger have calculated the theoretical thick target yield of this reaction. Fig. 3.2.6 shows the results of the calculation. Several other calculations have been made later on the thick target yield of the $T(d,n)^4He$ reactions and results compared with the experimental yield, Fig. 3.2.7.

For a thick target, the yields continue to increase with bombarding energy, however the observed neutron yields are usually different from the calculated yield. This divergence may be due to the lack of accurate energy loss data in metals or to the error introduced by assuming that the tritium concentration in the actual target examined is constant throughout its thickness. Disagreement is also due, in part, to the fact that the beam used in the experiment had a molecular beam.

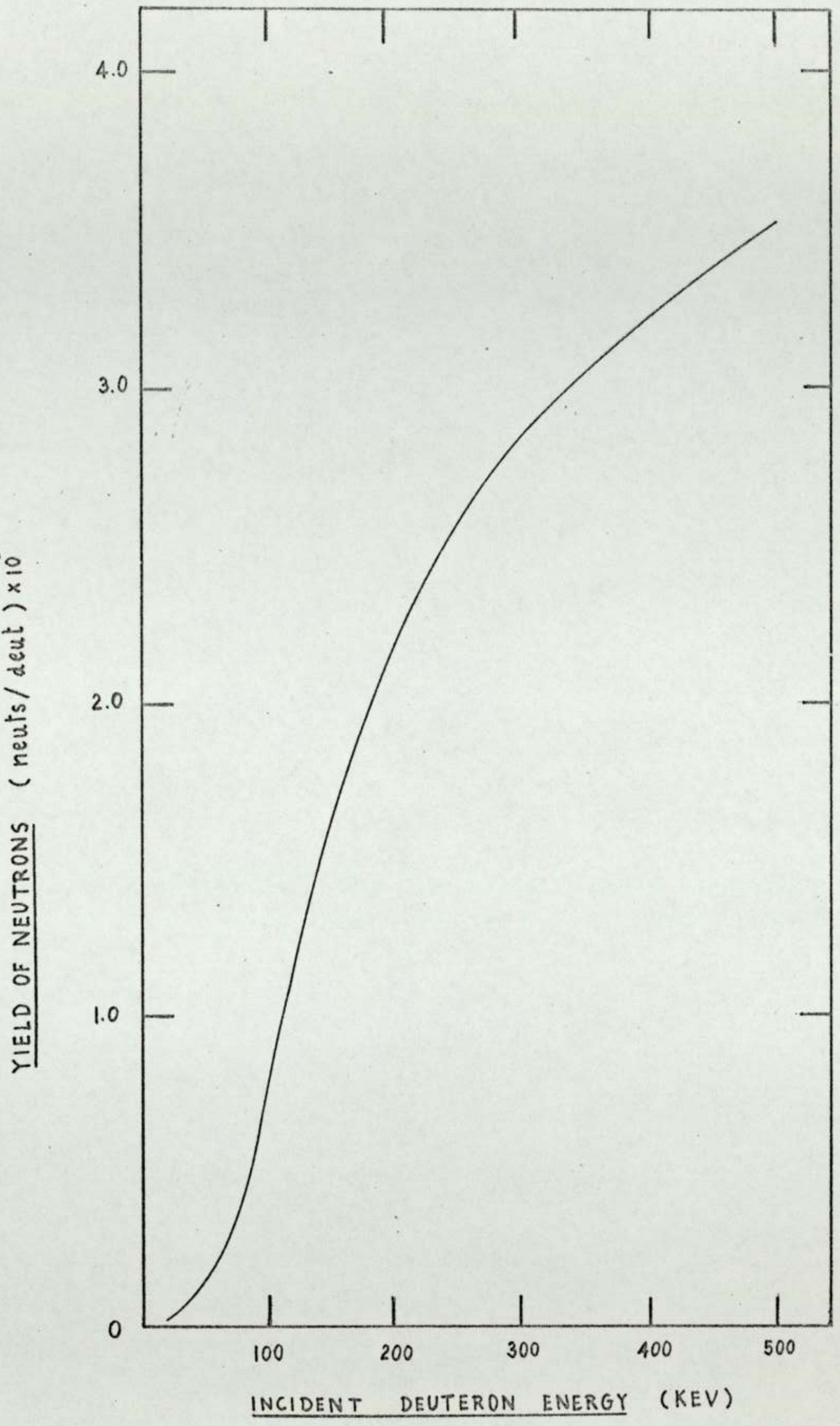

Figure 3.2.6 Theoretical thick target yield of neutrons from the $T(d,n)^4He$ reaction produced in titanium-tritide target

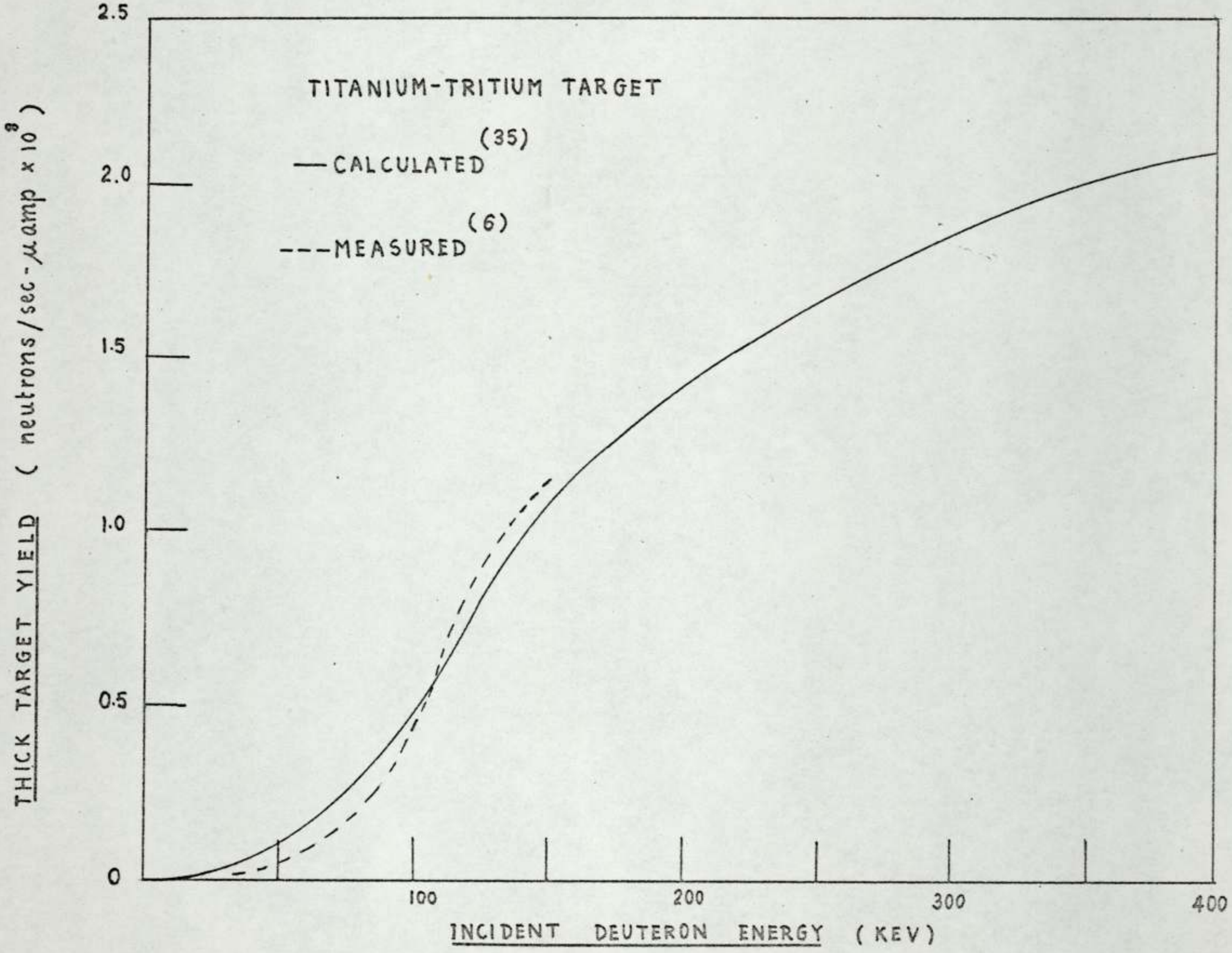

Figure 3.2.7 Comparison of experimental and theoretical thick target yield of neutrons from the $T(d,n)^4He$ reaction

Atomic and molecular beam

The Van de Graaf radio frequency ion source is of the type developed by Thonemann (37) 100 watts of power at a frequency of 20 mega Hertz is capable of producing a ratio of atomic to molecular ions of .85 while the more recently developed ones which are mostly used in the 150 KV accelerator can produce a very high ratio, about 0.9. For maximum output, the need for a very high atomic to molecular ions ratio for a 150 KV accelerator is apparent.

A singly ionized deuterium molecule $D_2^+$ will acquire the same energy as an ionized deuterium atom when accelerated through a potential of 150 KV, but it will be shared equally between the two deuterons, each having an energy of 75 KeV. Refer to Fig. 3.2.7 calculated curve it can be seen that neutron yield for a 150 KeV deuteron is about 4.5 times greater than for a 75 KeV deuteron. Hence the yield for an atomic ion is 2.25 times greater than from a molecular ion.

As the energy increases the yield ratio of the atomic to molecular ion decreases, for example, for the Van de Graaf working at 400 KeV the ratio of the neutron yield at 400 KeV to the neutron yield at 200 KeV for atomic ions is about 1.5. The yield, therefore, due to an atomic is only 0.75 as much as the yield from a molecular ion, the lower atomic to molecular ratio is then a compromise.

### 3.2.4. Target and target mounting

The target used in the experiment was a titanium-tritiated obtained from "Nuklear Chemic of Metallurgie G.M.B.N., West Germany.

It consisted of a copper base 32 mm. in diameter and 3 mm. thick, on to which a layer of titanium was deposited, the use of titanium is preferred to zirconium because of its lower stopping cross section. An active area of 25 mm. diameter was formed by absorbing 4.42 curies of tritium on to the surface. The active area was coated with a thin layer of aluminium to reduce the sputtering of the titanium and so enhance the target life.

Target mounting

Since tritium is lost from the titanium in appreciable quantities at about 200°C it is necessary to keep the temperature of the target below this value during the long irradiation period. Evidence (38) exists in the case of water cooled targets that the temperature of the front surface under deuteron bombardment does not differ from the temperature of the back by more than a few centigrades.

To reduce the heating effect the tritiated-titanium target was mounted on the water cooled target assembly as shown in Fig. 3.2.8.

### 3.3. Detection of gamma radiation

In the conventional activation analysis (CHAPTER IV) the standard procedure is the detection of radiation emitted during the decay of radioactive nuclides. The process of detection involves the evaluation of

(i) types and energies of radiation being emitted by sample

(ii) half lives of the various nuclides present

(iii) the amount of radiation due to each radioactive element

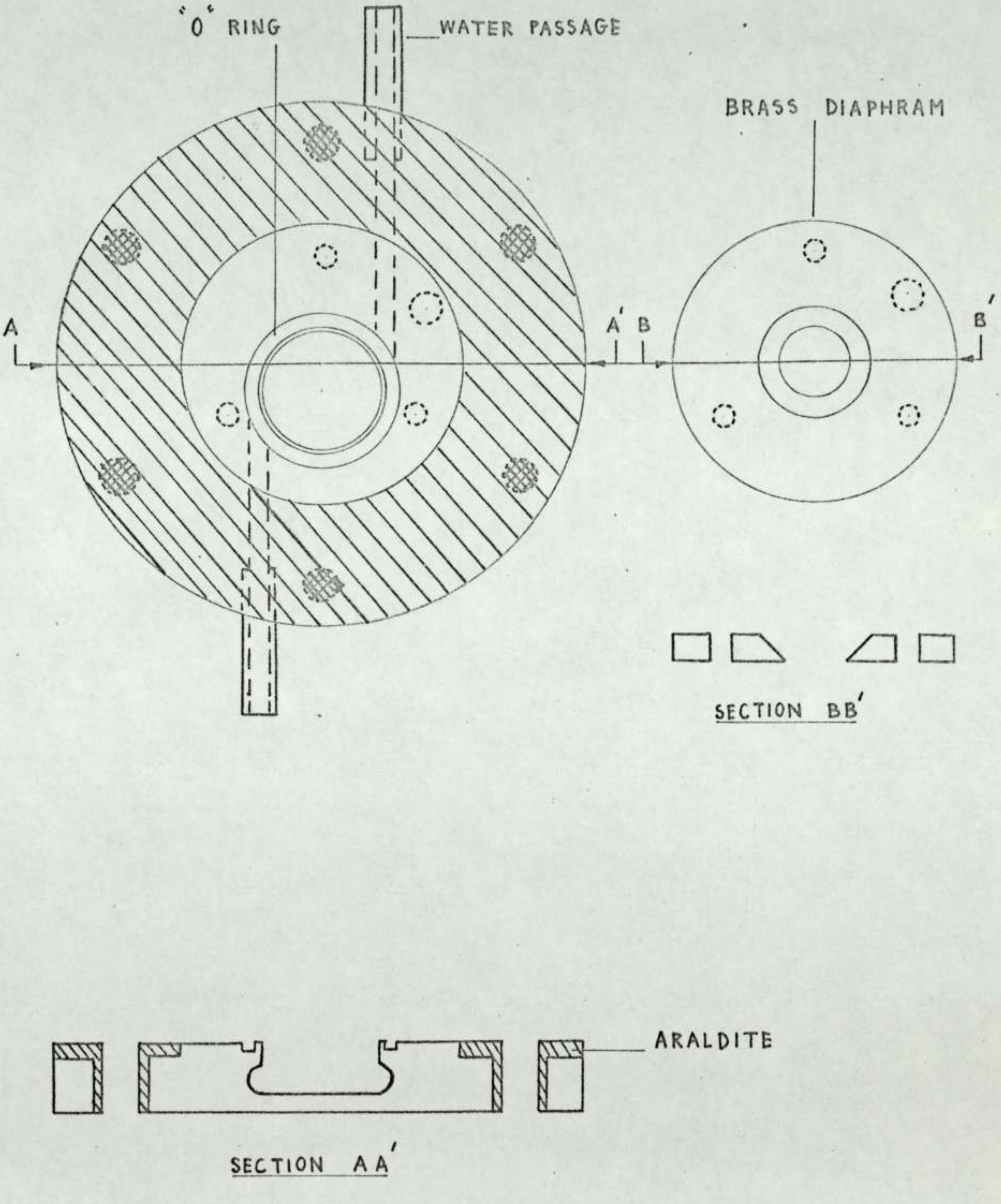

Figure 3.2.8 Water-cooled target assembly

The detection technique is facilitated by the fact that most radioactive nuclides exhibit characteristic beta and gamma ray energies and half lives. Owing to the continuous shape of beta spectra and beta self absorption beta specometry is difficult and omitted in favour of gamma spectrometry.

In some favourable cases (CHAPTER V) it is possible to detect the prompt $\gamma$-radiation emitted during the deexcitation of the excited nuclear states. The detecting process is then concerned with the evaluation of the yield and the energies of $\gamma$-radiation.

### 3.3.1. Properties of gamma ray

The purpose of a radiation detector is to convert the ionization produced by radiation into electronic signal. In the ionization process electrons are removed from an atom, resulting in the formation of positive ion core and free electrons. In the case of gamma radiation there are a number of mechanism which can be important in special cases and the possible processes by which the electromagnetic field of the gamma ray may interact with matter have been put in the following systematic form.(40)

| I Kind of interaction | II Effects of interaction |
|---|---|
| (i) Interation with atomic electron | (a) Complete absorption |
| (ii) Interaction with nucleons | (b) Elastic scattering |
| (iii) Interaction with the electric field surrounding nuclei or electrons | (c) Inelastic scattering |
| (iv) Interaction with mesonfield surround nucleons | |

There are 12 ways of combining column I and II, however in the energy domain met most frequently in nuclear transition, i.e. 0.01 to 10 MeV, all but few of the very minor effects are explainable in terms of three processes namely; photoelectric effect, compton scattering and pair production.

The photoelectric effect

In the photoelectric process a photon of energy E incident on an atom is absorbed resulting in the emission of a photoelectron with a kinetic energy given by

$$Ep = E - E_B \qquad (3.3.1)$$

where $E_B$ = the binding energy of the electron.

The interaction is strongest with the most strongly bound electron, i.e. the K-shell electrons which is responsible for 80% of the process. It has been found both theoretically and experimentally that the total photo effect decreases rapidly as the photon energy is increased further, on the contrary it increases rapidly with the electron binding energy, or with atomic number Z.

Theoretical calculations of photoelectric absorption coefficient, $\tau$, are quite difficult, and accurate results are available for certain limiting case of $E\gamma$ and Z (39). One special case of the theoretical expression, which holds for $E_B << E_\gamma << mc^2$ (0.51 MeV) is

$$\tau = NZ^5 (h\nu)^{-3.5}$$

where N = the number of atoms per unit volume

$h\nu$ = the photon energy

At low $\gamma$-ray energies, photo electric absorption represents by far the most efficient capture process.

The Compton effect

The Compton effect describes an elastic collision between a $\gamma$-ray photon and an atomic electron which is essentially free for sufficiently high $\gamma$-ray energies. Upon collision the $\gamma$-ray behaves in the same way as a particle, that is, it glances off at an angle and proceeds with reduced energy. The incident photon energy $h\nu$ is sufficiently high so that the photon momentum $\frac{h\nu}{c}$ must be considered

Conservation of energy and momentum lead to the formulae (40)

$$h\nu^1 = \frac{h\nu}{1 + (1 - \cos\theta)\frac{h\nu}{m_o c^2}} \qquad (3.3.3)$$

where $h\nu^1$ = the energy of the scattered photon

$\theta$ = the angle between its direction and that of the primary photon

$m_o$ = rest mass of the electron

the kinetic energy, $E_{kin}$, of the recoil electron is

$$E_{kin} = h\nu - h\nu^1 = h\nu\left[\frac{(1 - \cos\theta)\,h\nu/m_o c^2}{1 + (1 - \cos\theta)\frac{h\nu}{m_o c^2}}\right] \qquad (3.3.4)$$

The energies of the recoil electron in Compton collision range from zero ( $\theta = 0$) up to maximum value $E_{max}$ ( $\theta = 180^\circ$) given by

$$E_{max} = \frac{h\nu}{1 + \frac{m_o c^2}{2h\nu}} \qquad (3.3.5)$$

$E_{max}$, the maximum energy of the recoil Compton electron, is known as the Compton edge.

The quantum mechanical theory of the dependence of the absorption coefficient on photon energy has been derived by Klein and Nishina (41) In the special case where $h\nu >> m_oc^2$;

$$\sigma = \frac{NZ}{h\nu} \left[ \text{In} \frac{2h\nu}{m_oc^2} + \frac{1}{2} \right] \qquad (3.3.6.)$$

Only a fraction of the photon energy is transferred to an electron in a Compton collision and hence absorbed, the remainder is scattered without absorption, only the former represents a true energy absorption. Further absorption of the gamma photon with reduced energy may occurwhether as a result of photo electric effect or subsequent Compton absorption. The probability of Compton absorption occuring depends on the incident photon energy as well as on the atomic number of the absorber.

## The pair production effect

Absorption by pair production occurs when the incident photon energy exceeds 1.02 MeV. In this process, the gamma ray dis-appears and an electron and a positron are produced. The total kinetic energy of the pair is

$$E_{kin} = E - 1.02 \qquad (3.3.7)$$

This process only occurs in the field of charged particle normally the nucleus. Pair production in the field of quasi free electrons is completely negligible in all inorganic scintillating material. (42) As in the case of Compton scattering, only a part of the photon energy becomes absorbed energy in the pair production process.

At the end of its range the positron interacts with an electron, producing two anihilation radiation quanta each of energy 0.51 MeV.

One or both of these anihilation photons may escape or they may be absorbed in the detecting material by the Compton or photo electric process.

In Fig. 3.3.1, theoretical cross sections for sodium iodide are presented showing the total absorption as well as separate contributions of photo electric effect, Compton effect and pair production.

### 3.3.2. Types of detector

The working of $\gamma$-radiation detectors is based on the events described in the previous section, arising from the impact of ionization on matter. All $\gamma$-ray detectors utilize at least one of these processes to obtain a measurable out put signal and different types of detectors can be characterized by the nature of the interaction of the radiation with the matter.

Three of the oldest types are the ionization chamber, the proportional counter and the Geiger Müller tube. Each of these detector types employ gas filled chamber and operate by virtue of the ionization which is produced in them by the passage of charged particles. For $\gamma$-rays, the charged particles which are required for the production of ionization originate by secondary processes as described. These gas filled detectors have now been replaced by the solid semiconductor detectors which exhibit several advantages.

The principle of operation of a semiconductor detector is similar to that of a gas-filled detector, except the detecting medium is a solid. In this detector, an electric field is set up across a semiconductor medium of low electrical conductivity.

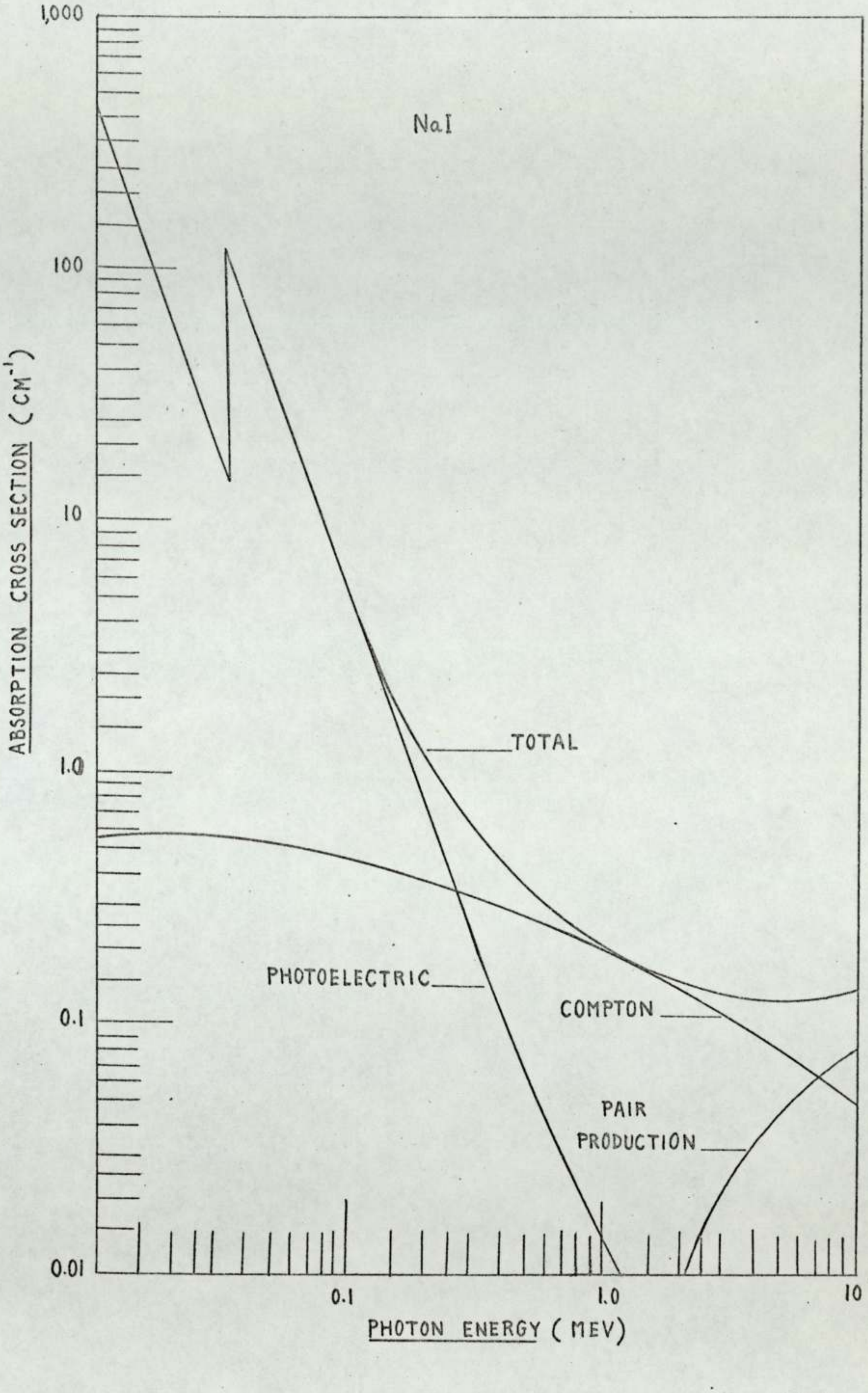

Figure 3.3.1 Absorption cross section of NaI (45)

An electric field sweeps out free electrons and holes, producing a depletion layer containing practically no free charge carriers. The extent of this carrier free region is determined by the applied electric field and can be changed by changing the field. The depletion layers have been produced in ion-drifted (43) and surface barrier detectors (44). When a charged particle passes through the medium, electron hole pairs are produced in it, the charges are separated by the electric field and collected at electrodes producing electrical signal.

The semiconductor detector possesses several advantages with respect to a gas-filled counter;

(i) its higher stopping power makes possible the fabrication of very small detector.

(ii) the energy necessary to produce an ion pair is much lower; 3.5 ev. in silicon as compared to 30 ev. in a gas. Thus, for a particle at a given energy, many more ion pairs are formed and collected in a semiconductor, which results in much higher resolution.

The type of detector, by far the most widely used as far as activation analysis is concerned, is the scintillation detector. In this detector excitation and sometimes molecular dissociation play important roles. When ionizing particles pass through certain substances, ionized and/or excited states are produced, which, during the return to the normal states, produce light emission, or a scintillations. In the modern scintillation detector, this light is picked up by a photomultiplier tube, and the resulting pulse of current out of the photo multiplier indicates the passage of the ionizing radiation through the scintillator. In general there are four classes of scintillators; inorganic crystals, organic crystals, plastic phosphors and liquid phosphors. The more prominent examples of each type are indicated in Fig. 3.3.2. (45)

While there are many desirable characteristics of a luminescent material as illustrated by the above table, the more important include (1) higher density for greater absorption of gamma rays, (2) increased pulse height for detection of low energy interactions, and (3) short decay times for fast counting.

The primary advantage of the inorganic crystals is their higher density which is mainly responsible for the higher stopping power and thus the greater counting efficiency for gamma rays. The alkali halides, and particular NaI(T $\ell$), exhibit such desirable characteristics as high density, high light out put transparency, and suitable index of refraction, it is with this material that most of the specifications will be concerned.

### 3.3.3. Choice of detector

The choice of detector for the present work was limited to two types namely, the semiconductor and the inorganic crystal detectors. The biggest drawbacks of the gas-filled counters are low sensitivity and relatively large resolving time. Besides if several trace elements are present, the use of Geiger-Müller tubes or ionization chamber will normally require chemical separations, some of which may be time consuming, while the use of proportional counter is limited to measurement in extremely low energy regions at most about 20 KeV. The efficiency for

Figure 3.3.2. Characteristics of Representative Scintillation Phosphors

| Material | | Wave length of maximum emission ($A^o$) | Decay Constant $\mu$ sec. | Density g/$cc^3$ | Relative Pulse height |
|---|---|---|---|---|---|
| Inorganic Crystals | Na(T $\ell$) | 4100 | .25 | 3.67 | 210 |
| | CsI(T$\ell$) | 4200-5700 | 1.1 | 4.51 | 55 |
| | KI(T$\ell$) | 4100 | 1.0 | 3.13 | 50 |
| | LiI(Eu) | 4400 | 1.4 | 4.06 | 74 |
| Organic Crystals | Anthracene | 4400 | .032 | 1.25 | 100 |
| | Trans-stilbene | 4100 | .006 | 1.16 | 60 |
| Plastic Phosphors | | 3500-4500 | .003-.005 | 1.06 | 28-48 |
| Liquid Phosphors | | 3550-4500 | .002-.008 | 1.86 | 27-49 |

radiation with an energy of 1 MeV is only approximately 1-1.5%.

Of all the semiconductors the Lithium drifted germanium detector is perhaps the one most exclusively used in activation analysis as a high resolution $\gamma$-ray detector, while the sodium iodide (thallium activated) is the best choice from the scintillating crystals and in recent years the 3 x 3-inch NaI(T$\ell$) has become a standard size.

The important advantage of the Ge(Li) drifted detector over the NaI(T$\ell$) is that the energy necessary to create an electron-hole pair is only about 3 eV, while in the latter case an energy expenditure of at least 300 eV is needed to secure the release of one photo electron from one cathode of one associated photo multiplier. Statistical fluctuations in the pulse production process are much smaller for a solid state detector, hence the resolution is therefore inherently higher as shown by the work of Girardi and Pauly (46).

The advantages of high resolution detectors become obvious in the case where a complex spectrum is obtained and the peaks may be over lapped. The inability of the NaI(T$\ell$) to resolve the photo peaks could lead to serious error (47).

The relatively poor resolution of the NaI(T$\ell$) crystal, however, is compensated by its higher detection efficiency. The scintillation crystal is also available in much larger sensitive volume than the solid state crystal. The increase of the detector size not only gives in general, a better efficiency but also the dependence of efficiency versus $\gamma$-ray energy becomes less pronounced, due to the higher probability of total energy loss in the sensitive volume of the detector by multiple Compton scattering with final photo electric absorption. Hence in the situation where all the absorption peaks are well separated and the resolution of the detector is not an important factor, the choice of NaI(T$\ell$) scintillation crystal is obvious.

# CHAPTER IV AN INVESTIGATION BY NEUTRON ACTIVATION OF THE Mg/Fe RATIO AFTER THE REACTION $MgO + Fe_2O_3 \rightarrow MgFe_2O_4$

## 4.1. Introduction

The preparation of the technologically important spinel $MgFe_2O_4$ has been the subject of several investigations, some results from which are still a matter of controversy. According to Paladino (48) who investigated phase equilibria in the ternary system FeO - MgO - $Fe_2O_3$, $Mg^{2+}$ will replace $Fe^{2+}$ in $Fe_2O_4$ beyond $MgFe_2O_4$ up to a composition $(MgO)_{0.092}.MgFe_2O_4$ but the stoichiometric composition $MgFe_2O_4$ does not exist as a single spinel phase. Entirely different conclusions were reached by Reijnen (49) who suggested that Paladino may have been deceived through a discrepency arising from his use of co-precipitated oxalates as starting material in his method of preparation.

Reijnen's conclusions were based on a thermogravimetric analysis of the reactions of several compositions in the neighbourhood of the equimolar composition (MgO - $Fe_2O_3$) and also on the observation that in a system containing a slight excess of $Fe_2O_3$ the ratio of cation to anion is always 3 : 4 in the limit of high temperature and/or low oxygen pressure. However, he also assumed that the Mg/Fe ratio in the system remain constant. The work described here is concerned with the validity of this last assumption.

The starting materials prepared for the experiments were B.D.H. reagent grade MgO and $Fe_2O_3$. Following Reijnen, an equimolar composition of these constituents was thoroughly mixed, pressed and fired in oxygen at 1100°C for six hours. The product of this reaction was thoroughly ground, sieved, mixed and pressed for the second firing. At this stage the samples were divided into three groups and sintered in oxygen for six hours at 1100, 1200 and 1400°C respectively. It was decided to measure the Mg/Fe ratio in these samples by fast neutron activation analysis, since results obtained by this method are independent of the state of chemical combination of the elements and also of the oxygen content.

This example is not in general a typical application of fast neutron activation analysis technique where one is concerned with detecting small amounts of impurity. Nevertheless it illustrates how the method can be employed under specific circumstances to provide answers to the problem in which other methods have failed to reach the same conclusion.

## 4.2. Principle of method

Consider the formation of radio active isotope whose decay constant is $\lambda$ sec.$^{-1}$ bombarding with $\phi$ neutrons/cm.$^2$-sec.

Let $\sigma$ be the activation cross section in cm.$^2$

No be the number of nuclei in the sample

Then the net rate of growth of the radio active nuclides, N is given by

$$\frac{dN}{dt} = No\,\phi\,\sigma - \lambda N \qquad (4.2.1)$$

Substitute $x = No\,\phi\,\sigma - \lambda N$ in Eq. (4.2.1) and integrate between the limits t = o and t = t, we get

$$N_t = \frac{No\,\phi\,\sigma}{\lambda}\left(1 - e^{-\lambda t}\right) \qquad (4.2.2)$$

Define the activity $A_t$ in terms of disintegrations per second as $A_t = \lambda N_t$ Eq. (4.2.2) can be written as (dropping the subscript)

$$A = No\sigma\phi(1 - e^{-\lambda t}) \qquad (4.2.3)$$

Eq. (4.2.3) describes the induced activity at the end of the irradiation for the sample irradiated for t seconds.

Irradiation of sample containing Mg and Fe

Suppose the irradiation-counting cycle consists of irradiation for $t_1$ sec., waiting for $t_2$ sec. and counting for $t_3$ sec.

The number of count recorded, due to the decay of radio isotope formed, in the counting period is

$$N_c = \frac{KNo\sigma\phi}{\lambda}(1 - e^{-\lambda t_1})\, e^{-\lambda t_2}(1 - e^{-\lambda t_3}) \qquad (4.2.4)$$

where K is a constant and a function of counting geometry.

Suppose we write for the irradiation of Fe

$$N_{c1} = \frac{K_1 N_{Fe}\sigma_1\phi_1(1 - e^{-\lambda_1 t_{11}})\, e^{-\lambda_1 t_{21}}(1 - e^{-\lambda_1 t_{31}})}{\lambda_1} \qquad (4.2.5)$$

and similarly for Mg

$$N_{c2} = \frac{K_2 N_{Mg}}{\lambda_2}\sigma_2\,\phi_2(1 - e^{-\lambda_2 t_{12}})\, e^{-\lambda_2 t_{22}}(1 - e^{-\lambda_2 t_{32}}) \qquad (4.2.6)$$

from (4.2.5) and (4.2.6) we get

$$\frac{N_{Fe}}{N_{Mg}} = \left(\frac{N_{c1}}{N_{c2}}\right)\left(\frac{\lambda_1}{\lambda_2}\right)\left(\frac{K_2}{K_1}\right)\left(\frac{\sigma_2}{\sigma_1}\right)\left(\frac{\phi_2}{\phi_1}\right)\left(\frac{1-e^{-\lambda_2 t_{12}}}{1-e^{-\lambda_1 t_{11}}}\right)\left(\frac{e^{-\lambda_2 t_{22}}}{e^{-\lambda_1 t_{21}}}\right)\left(\frac{1-e^{-\lambda_2 t_{32}}}{1-e^{-\lambda_1 t_{31}}}\right) \qquad (4.2.7)$$

The term $\left(\frac{\phi_2}{\phi_1}\right)$ is usually cancelled out for materials irradiated under identical condition.

Eq. (4.2.7) shows that the $Fe_{/Mg}$ ratio can be evaluated if all other parameters are known.

This direct comparison however is inaccurate owing to the fact that

(i) the activation cross sections are rarely known precisely, the errors involved in measuring were at least 5-10 percents.

(ii) the efficiency of the detector must be determined for every source to detector geometry and in some cases are very difficult and inaccurate.

(iii) some corrections due to absorption of radiation between source and detector and self-absorption must be made and this introduces additional errors.

These errors can be minimesed if this ratio is compared to the standard.

For the standard we can write

$$\frac{Fe}{Mg} = \left(\frac{N^{1}{}_{c1}}{N^{1}{}_{c2}}\right)\left(\frac{\lambda_1}{\lambda_2}\right)\left(\frac{K^{1}{}_{2}}{K^{1}{}_{2}}\right)\left(\frac{\sigma_2}{\sigma_1}\right)\left(\frac{1-e^{-\lambda_2 t^{1}_{21}}}{1-e^{-\lambda_1 t^{1}{}_{11}}}\right)\left(\frac{e^{-\lambda_2 t^{1}{}_{22}}}{e^{-\lambda_1 t^{1}{}_{21}}}\right)\left(\frac{1-e^{-\lambda_2 t^{1}{}_{32}}}{1-e^{-\lambda_1 t^{1}{}_{31}}}\right) \qquad (4.2.8)$$

For samples irradiated under identical conditionsand if the respective counting intervals are the same. Then from Eq. (4.2.7) and Eq. (4.2.8) we get

$$R = \frac{N_{Fe}}{N_{Mg}} \Big/ \frac{Fe}{Mg} = \left(\frac{N_{c1}/N_{c2}}{N^{1}{}_{c1}/N^{1}{}_{c2}}\right)\left(\frac{K_2/K_1}{K^{1}{}_{2}/K^{1}{}_{1}}\right)\left(\frac{e^{-\lambda_2 t_{22}}}{e^{-\lambda_1 t_{21}}}\right)\left(\frac{e^{-\lambda_1 t^{1}{}_{21}}}{e^{-\lambda_2 t^{1}{}_{22}}}\right) \qquad (4.2.9)$$

R is then expressed as a percentage excess of magnesium or Iron, and save for the factor K, is proportional to the ratio of the activities induced at the end of the irradiation.

Factor $\frac{K_2/K_1}{K^1_2/K^1_1}$ for this measurement is taken to be unity with some errors which will be described in the later sections.

### 4.2.1. The $^{56}Fe(n,p)^{56}Mn$ and $^{24}Mg(n,p)^{24}Na$ reactions

The $^{56}Fe(n,p)^{56}Mn$ and $^{24}Mg(n,p)^{24}Na$ reactions were chosen primarily because of relatively high activation cross sections, isotopic abundances and reasonable half-lives of the produced isotopes. Nuclear constants (5 ), (51) of the above reactions are listed below.

| Reaction | $^{24}Mg(n,p)^{24}Na$ | $^{56}Fe(n,p)^{56}Mn$ |
|---|---|---|
| En(MeV) | ~ 14 | ~ 14 |
| Cross section (mb) | ~ 180 | ~ 110 |
| Half Life (hr.) | 15 | 2.58 |
| Principle Mode of Mode of Decay (Energy MeV) | $\beta$ (1.4), $\gamma$(1.37,2.75) | $\beta$ (0.75,1.05,2.56), $\gamma$(0.847,1.81,2.13) |

| Element | Mg. | | | Fe | | | |
|---|---|---|---|---|---|---|---|
| Isotope | 24 | 25 | 26 | 54 | 56 | 57 | 58 |
| Isotopic Abundance (%) | 78.7 | 10.13 | 11.17 | 5.82 | 91.66 | 2.19 | 0.33 |

The $^{24}Na$ decays almost 100% by the emission of $\beta^-$ to the second excited levels of $^{24}Mg$. The resulting $\gamma$-rays are emitted in cascade of energies 1.37 and 2.75 MeV.

The $^{56}Mn$ decays principally by the emission of $\beta^-$ rays of three different energies to the third and fourth level of $^{56}$Fe. the main $\gamma$-lines are the .847, 1.81 and 2.11 MeV.

These are shown schematically in Fig. 4.2.1. $\gamma$ - spectrometry (section 4.5) performed on the irradiated materials hence provided information concerning the type and relative amount of nuclides involved.

### 4.2.2. Competing reactions

Competing reactions for Mg and Fe are listed in Fig. 4.2.2. and Fig. 4.2.3. respectively.

Figure 4.2.2. Competing reactions for Mg

| Reaction | Cross section | Half-Life | Principle Mode of Decay Energy (MeV) |
|---|---|---|---|
| $^{26}Mg(n,\alpha)^{25}Ne$ | 35 mb | 38 sec. | $\beta^-$(4.4,3.9), $\gamma$(.44,1.65) |
| $^{26}Mg(n,\gamma)^{27}Mg$ | 50 mb | 9.5 min. | $\beta^-$(1.75,1.59), $\gamma$(.83,1.01) |
| $^{25}Mg(n,p)^{25}Na$ | 63 mb | 60 sec. | $\beta^-$(3.8,2.8),$\gamma$ (.89,.58,.4,1.61) |
| $^{26}Mg(n,p)^{26}Na$ | 27 mb | 1 sec. | $\beta^-$(6.7),$\gamma$ (1.82) |
| $^{26}Mg(n,{}^{3}He)^{24}Ne$ | 3 mb | 3.38 min. | $\beta^-$(1.98,1.10), $\gamma$(.47,.88) |

Figure 4.2.3. Competing reactions for Fe

| Reaction | Cross section | Half-Life | Principle Mode of Decay Energy (MeV) |
|---|---|---|---|
| $^{54}Fe(n,2n)^{53}Fe$ | 15 mb | 8.9 min. | $\beta^+$(2.6),$\gamma$ (.37) |
| $^{54}Fe(n,p)^{54}Mn$ | 370 mb | 3.4 days | Electron Capture, $\gamma$ (.84) |
| $^{54}Fe(n,\alpha)^{51}Cr$ | 270 mb | 27.8 days | Electron Capture, $\gamma$(.325) |
| $^{57}Fe(n,p)^{57}Mn$ | 50 mb | 1.7 min. | $\beta^-$(2.6,),$\gamma$(.122,.014,.137,.22,.71) |

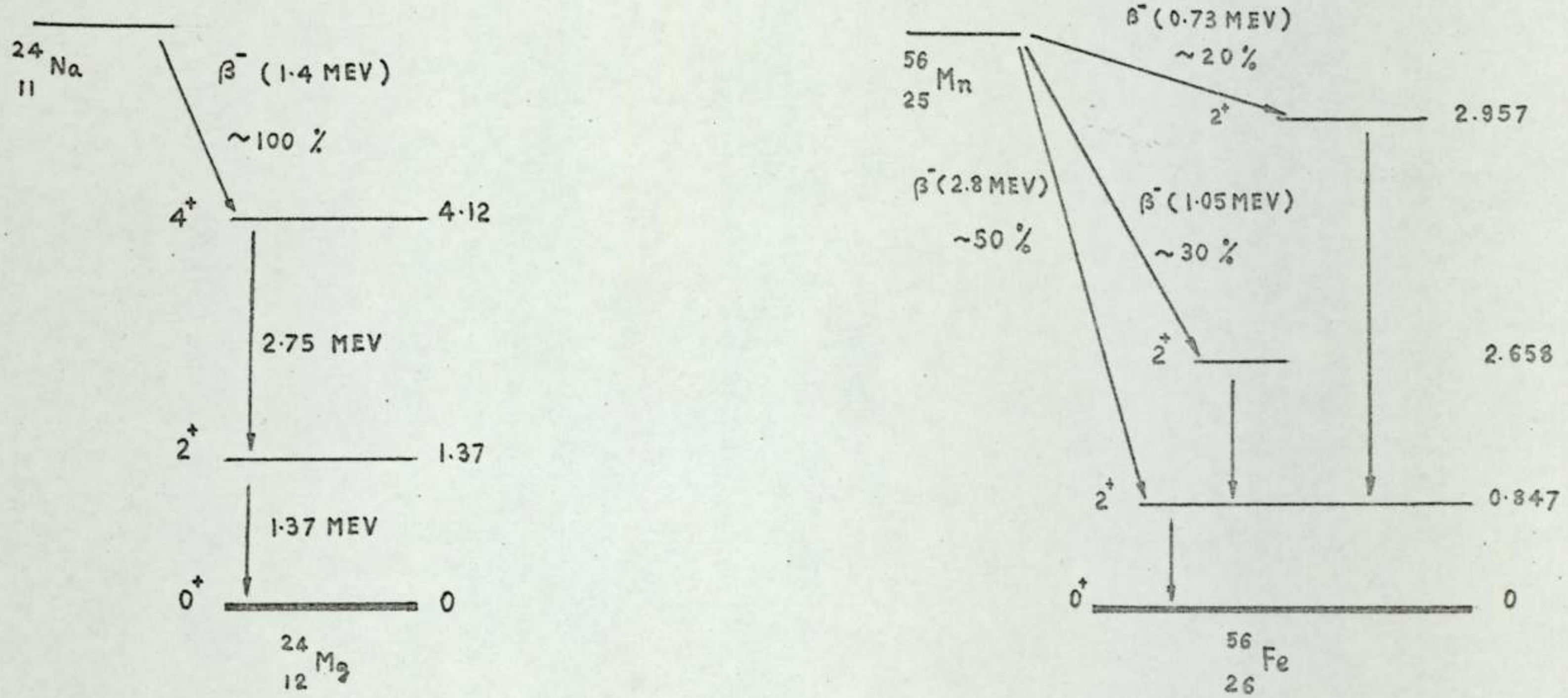

Figure 4.2.1 Decay schemes of $^{24}$Na and $^{56}$Mn

Comment

Radioactive isotopes produced by interfering reactions are either very short lived or very long lived ones. The former effect could be completely eliminated by cooling the samples for about 30 min. to 1 hr. while the latter are produced in negligible quantities for 5 hr. irradiation. Only the $^{26}$Mg(n, $\gamma$)$^{27}$Mg and $^{54}$Fe(n,2n)$^{53}$Fe are worthy of taking into consideration because of the half-lives of the product isotopes. These are 9.5 min. and 8.9 min. respectively and the isotopes of which do not decay completely in a period of 1 hr. if produced in considerable quantities.

Consider first the absorption of thermal neutrons on $^{26}$Mg to produce $^{27}$Mg, the thermal neutral flux, which results from the 14 MeV neutrons scattered off the wall of the flight tube and the end flange, can be shielded by covering the samples with cadmium sheet. This may not be convenient when samples are rotating very close to the end flange for maximum yield. The thermal flux, however, has been reported (52) to be a factor of $10^4$ down on the fast flux at the sample position and because of smaller cross section and isotopic abundance of $^{26}$Mg the yield is hence completely negligible. Contribution from resonance neutrons is also too small to be considered.

The same arguments also apply to the case of $^{54}$Fe(n,2n)$^{53}$Fe reaction. The negligible effect of this reaction was also reported by Yasumi (53) who found no trace of $^{54}$Fe(n,2n)$^{53}$Fe while measuring the $^{56}$Fe(n,p)$^{56}$Mn reaction cross section with 14 MeV neutron.

### 4.2.2. Interfering reactions

Both magnesium and iron used in the experiments were in the form of oxides. Fast neutron induced reaction on $^{16}O$ isotope produces $^{16}N$ by the (n,p)reaction. This radio active isotope decays by the emission of 6.13 and 7.1 MeV $\gamma$-rays with a half-life of 7.4 sec. This interfering effect was also eliminated by cooling method described earlier.

Two reactions which can produce $^{24}Na$ and $^{56}Mn$ isotopes are the (n, $\alpha$) reactions on $^{27}Al$ and $^{59}Co$. Aluminium impurity was checked by looking for the 1.02 MeV $\gamma$-line resulting from the $^{27}Al(n,p)^{27}Mg$ reaction, the $^{27}Mg$ has a half life of 9.5 min. The peak due to 1.02 MeV $\gamma$-ray was not observed in the spectrum recorded few minutes after the irradiation. A check on cobalt contamination was not necessary because of high purity reagents used.

### 4.3. Preparation of irradiating material

The sintered samples were obtained from X-ray CRYSTALLOGRAPHY DIVISION, the method of preparation was briefly described in section 4.1. Also prepared were the unsintered samples of an equimolar mix of the MgO and $Fe_2O_3$ to serve as standards and unsintered samples containing a 5% excess and 5% deficiency of MgO to check the accuracy of method. Each sample was thoroughly ground and mixed before being placed in containers.

### 4.3.1. Specimen container

Initially a 4.5 cc. polyethelene cylindrical container was used to fill specimens taken from the prepared samples. Preliminary investigations showed that reasonable results were obtained when comparing two unsintered standards. However results obtained for the sintered samples appeared to be in a great degree of inconsistency and error indicating that the system employed was unsatisfactory. The discrepencies were mainly due to the fact that

(i) Sintered samples packed loosely inside the containers after a few hr. of being rotated, tended to gather in one corner. The effect is illustrated below

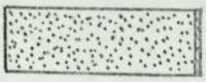

BEFORE

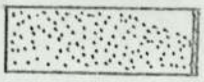

AFTER

(ii) The packing was different between sintered and unsintered specimens, resulting in relatively large differences in macroscopic densities. The effect of self-absorption of $\gamma$-rays was pronounced and had to be accounted for, but the geometry of the container prevented an accurate correction being made.

(iii) Successive layers of sample and standard were not exposed to same flux of neutrons.

Attempts were made to press specimens into container, this method was also unsuccessful due to variation in local density.

To eliminate the variation in local density and minimise the self-absorption effect, specimens weighted from 7 to 9 gm. from each of the prepared samples were pressed into pellets of approximately the same density by a 30 ton press. The finished pellet was wrapped around the side by a ring of scotch tape to localise it inside a plastic container and hence the translational motion of the pellet during rotating was eliminated. To prevent contamination of the materials the container was sealed with a sheet of scotchtape (Fig. 4.3.1)

To ensure uniformity of irradiation specimens were rotated on a turn table at a speed of 36 rev per min. The specimens holder is shown in Fig. 4.3.1.

This sytem permitted four samples to be irradiated simultaneously, two of which were the unsintered standards to check the method, the other two were the sintered samples. The accuracy was then being checked for every measurement carried out.

## 4.4. Irradiation technique

Specimens were irradiated with 14 MeV neutrons derived from the $T(d,n)^4He$ reaction using deuterons of 300 KeV from the 500 KV Van de Graaf accelerator (section 3.1). Samples were positioned as close to the tritium target as possible, since on increasing the target sample distance the flux is reduced in accordance with the inverse square law. The minimum distance could be used for this experiment because systematic error due to uncertainty in the target sample distance was immaterial. Also neglected was the effect of neutron energy spread at any particular angle due to effects of deuteron energy loss and small angle scattering in the target. The positioning of sample assembly for irradiation is shown in Fig. 4.4.1.

The following errors were practically eliminated by rotating the samples during irradiation.

(i) Error due to the possible deviations of the centre of

Figure 4.3.1

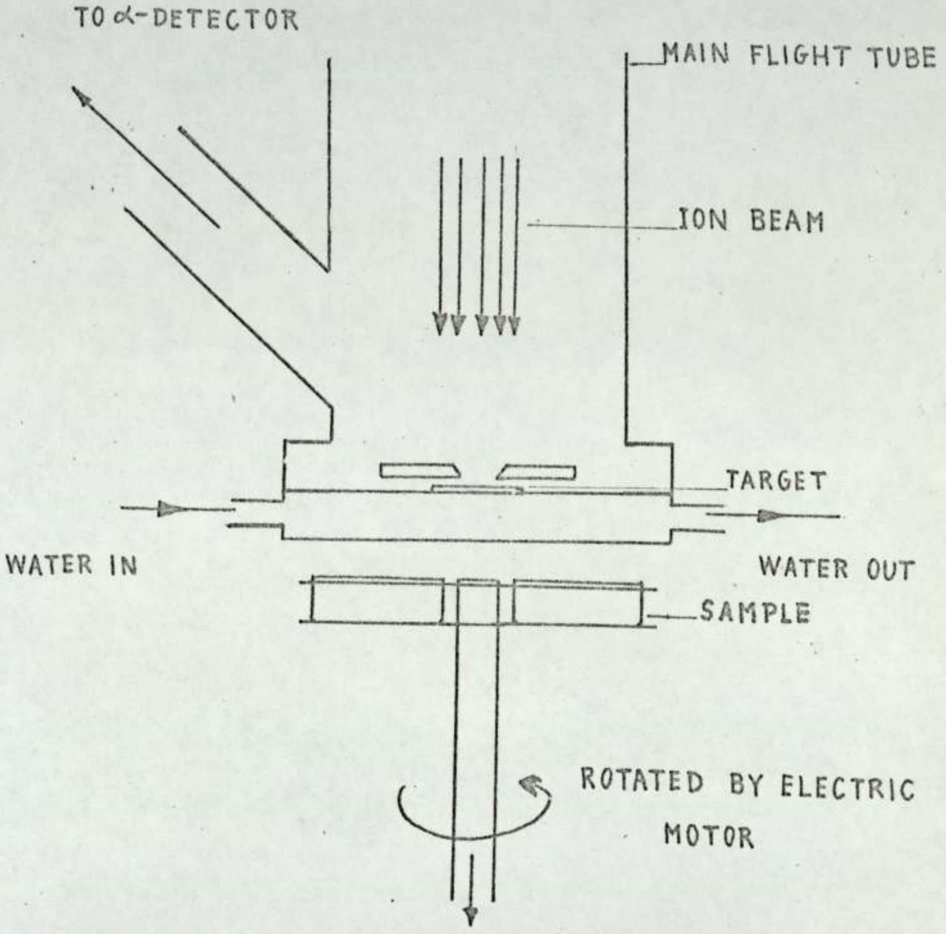

Figure 4.4.1 Experimental neutron activation analysis arrangement

the deuteron beam spot from the target centre.

(ii) The effects of angle dependent neutron attenuation in the target assembly and for the contribution of elastically scattered neutrons to the activation of the sample.

### 4.4.1. Contribution from D-D neutrons

Accompanying the high energy neutrons there were, in small numbers, neutrons produced by the interaction of the deuteron beam with deuterium embedded in the tritium target. Under the conditions of the measurements, the maximum energy these neuterons could assume was 3.7 MeV in the forward direction. For the $^{24}$Mg (n,p)$^{24}$Na reaction these neutrons had energies which were below the threshold for the reaction.

The threshold for the $^{56}$Fe(n,p)$^{56}$Mn is 2.9 MeV, (30) but cross section is known (54) to be only a fraction of millibarn and no appreciable number of reaction can occur.

### 4.4.2. Monitoring of neutron flux

The comparative method employed allowed the calculation to be made without an accurate knowledge of neutron flux. Nevertheless it was desirable to keep the yield of neutron fairly uniform over the irradiating period since neutrons given out in bursts due to rapid fluctuation in beam current or voltage could upset the symmetry requirement. Neutron flux was monitored by associated particle technique (30).

### 4.5. Counting apparatus

The $\gamma$-rays resulting from the decay of $^{24}$Na and $^{56}$Mn were detected* by a 2 x 2-inch NaI(T$\ell$) crystal which was available at the time. An integral line assembly allowed the crystal to be directly attached to a photomultiplier tube with a rigid high index optical coupling medium. The crystal and matching phototube were hermitically encapsulated in a low mass light tight housing having aluminium entrance window. Signals from the photomultiplier were fed into a 100 multichannels analyser via a cascaded emitter follower. Both the detector and the analyser were obtained from Technical Measurement Corporation (U.S.A.).

### 4.5.1. Background and shielding

The counting was performed in a low level background room situated approximately 100 meters from any source of neutron to eliminate the effect of thermal neutron absorption of $^{23}$Na in the crystal itself. Background contribution is most notably from the concrete due to $^{40}$K activity in cement which often contains 5% of K. The $^{40}$K provides a monoenergetic $\gamma$-ray of 1.46 MeV. (12) Much smaller amounts could come from Ra and Th due to crystal and aluminium container contaminants (55). Thorium is relatively easily identified by its 2.12 MeV decay $\gamma$-ray while average $\gamma$-ray from radium is about 0.8 MeV. The glass in phototube also contains significant amounts of $^{40}$K and a smaller amount of Ra.

To reduce the background level the crystal was housed in a thick lead castle which was covered on the top by a 1.3 cm thick

---

*Initially a 3 x 3" NaI(T$\ell$) and a R.I.D.L. 400-channel analyser was used but the print out mechanism was not working satisfactorily at times.

Figure 4.5.1

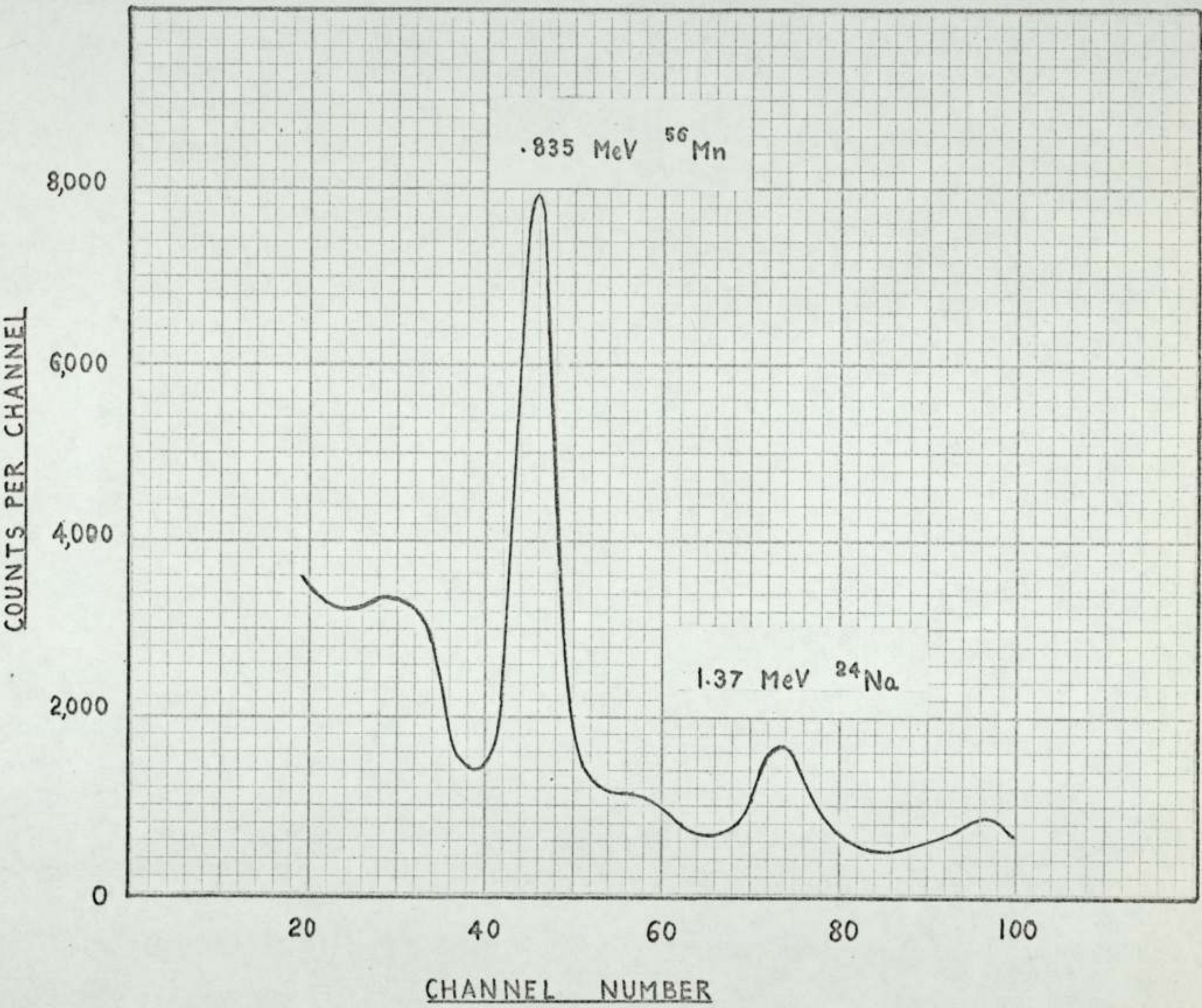

Figure 4.5.2 $\gamma$-Rays spectrum obtained from bombarding of $MgFe_2O_4$ sample with 14 MeV neutrons

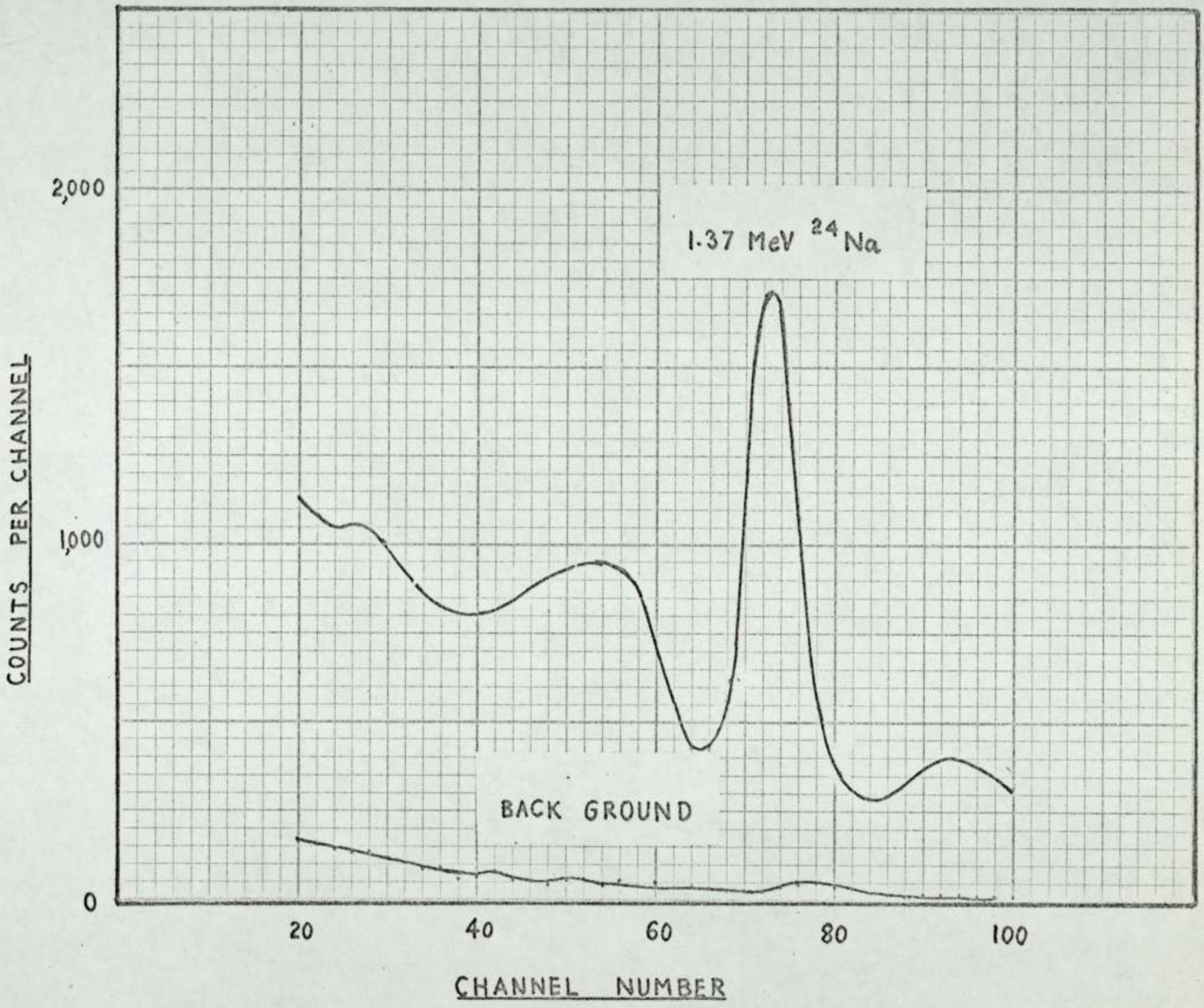

Figure 4.5.3 γ -Rays spectrum recorded 26 hr. after irradiation ended and background spectrum

lead plate. Typical arrangement of the counting equipment and shielding is shown in Fig. 4.5.1.

### 4.5.2. Counting technique

At the end of the irradiation samples were left to cool down for about 1 hr. before counting commenced. Each sample was counted in turn for 10 min. in the first counting period. Counting of 40 min was resumed in the following day. It is important for the counting interval to be less than the half-life to allow activity to be plotted at the mide time of the counting interval (section 4.6.5.)

Spectra showed the .835 MeV and 1.37 MeV lines from the $^{56}$Mn and $^{24}$Na in Fig. 4.5.2. which was recorded immediately after cooling. Fig. 4.5.3 shows the spectrum taken 26 hr. later and only the 1.37 MeV line was present while contribution from smaller half-lived one was almost negligible.

Background was found to be fairly constant over the period of counting, the spectrum of which is shown in Fig. 4.5.3.

### 4.5.4. Method of determining induced activities

The induced activities were initially determined from the integrated counts under the photopeaks by Covell's method (55) which developed an error of about 3%. The major contributions to the error term was the counting statistic.

Since spectra contained no other peaks apart from those of interest, integrating the count rate from the portion of the spectrum should reduce the counting statistic to less than 1% and the method of half-life measurement should allow the two different activities to be isolated. In view of the smaller error involved this method was adopted in preference to Covell's method. Fig. 4.5.4. shows a typical log plot of the induced activity versus time of the 1400 sintered sample.

The $^{56}$Mn and $^{24}$Na activities were isolated from each other by two methods, namely a graphical method and an analytical method. Observation made more than 24 hrs. later gave only the $^{24}$Na spectrum, spectrum stripping therefore allowed the spectrum of the $^{56}$Mn activity to be isolated (Fig. 4.5.4, Fig. 4.5.5). The contributions from the $^{56}$Mn activity in the later counting periods were then corrected for. The process was repeated several times and hence allowed the pure $^{24}$Na activity to be obtained with greater accuracy. The final corrected $^{56}$Mn activity was determined analytically by subtracting off the contribution from the weighted mean $^{24}$Na activity as follows:

Let $Y_1, Y_2 \ldots . Y_g$ be the mixed count rate in the first counting period at time $X_1, X_2 \ldots . X_g$.

$y_1, y_2 \ldots . y_k$ be the graphically determined count rate of $^{24}$Na at time $x_1, x_2 \ldots . x_k$ respectively.

Consider only error from counting statistic

$T_f$ be the counting interval in the first period.

$T_s$ be the counting interval in the second period.

suppose the background be BG count/min

Take the half lives of $^{56}$Mn and $^{24}$Na to be 2.58 and 15 hrs. respectively

Define decay constants $\lambda_1 = \frac{.693}{15}$ , $\lambda_2 = \frac{.693}{2.58}$

Then the weighted mean of the initial induced $^{24}$Na activity can be written as

$$\tau_o = \frac{\sum_{i=1}^{k} \omega_i \tau_i}{\sum_{i=1}^{k} \omega_i} \qquad (4.5.1)$$

where $\tau_i = y_i e^{\lambda_i x_i}$

$$\omega_i = \frac{1}{\sigma_i^2}$$

and $\sigma_i = \frac{(y_i + BG)^{\frac{1}{2}}}{T_S^{\frac{1}{2}}} \left(\frac{\tau_i}{y_i}\right)$

the average error due to the statistic of the counting alone is given by

$$\sigma^2 = \frac{1}{\Sigma \, 1/\sigma_i^2} \qquad (4.5.2)$$

Let $t_j = x_j - X_1$ $\qquad j = 1, 2, \ldots . k$

$t_j$ is then the total time elapsed between first counting period at time $X_1$ and the second period at time $x_j$

Define $R_j = y_j e^{\lambda_1 t_j}$

$$\rho_j = \frac{(y_i + BG)^{\frac{1}{2}}}{T^{\frac{1}{2}}} \left(\frac{R_j}{y_j}\right)$$

$$\omega_j = \frac{1}{\rho_j^2}$$

At time $t_j$ average contribution from $^{24}$Na activity is given by

$$C_1 = \frac{\sum_{j=1}^{k} \omega_j R_j}{\sum_{j=1}^{k} \omega_j} \qquad (4.5.3)$$

The average error associated is given by

$$\alpha_1^2 = \frac{1}{\sum_{j=1} {}^1/\rho_j^2} \qquad (4.5.4)$$

The initial induced activity of $^{56}$Mn due to one observation is then

$$M_1 = (Y_1 - C_1)e^{\lambda_2 X_1} \qquad (4.5.5)$$

with an error of $K_1 = (\beta_1^2 + \alpha_1^2)^{\frac{1}{2}} \dfrac{M_1}{Y_1 - C_1}$ (4.5.6)

where $\beta_1 = \dfrac{(Y_1 + B)^{\frac{1}{2}}}{T_f^{\frac{1}{2}}}$

The weighted mean of g observations is

$$\gamma = \frac{\sum_{a=1}^{g} Wa\, Ma}{\sum_{a=1}^{g} Wa} \qquad (4.5.7)$$

where $Wa = \dfrac{1}{K_a^2}$ $\qquad a = 1, 2 \ldots . g$

and the average error of $\gamma$ is calculated from

$$q^2 = \frac{1}{\sum_{a=1} \frac{1}{K_a^2}} \qquad (4.5.8)$$

An algol programme was written for the above calculation, the programme printed out the initial activity of each component

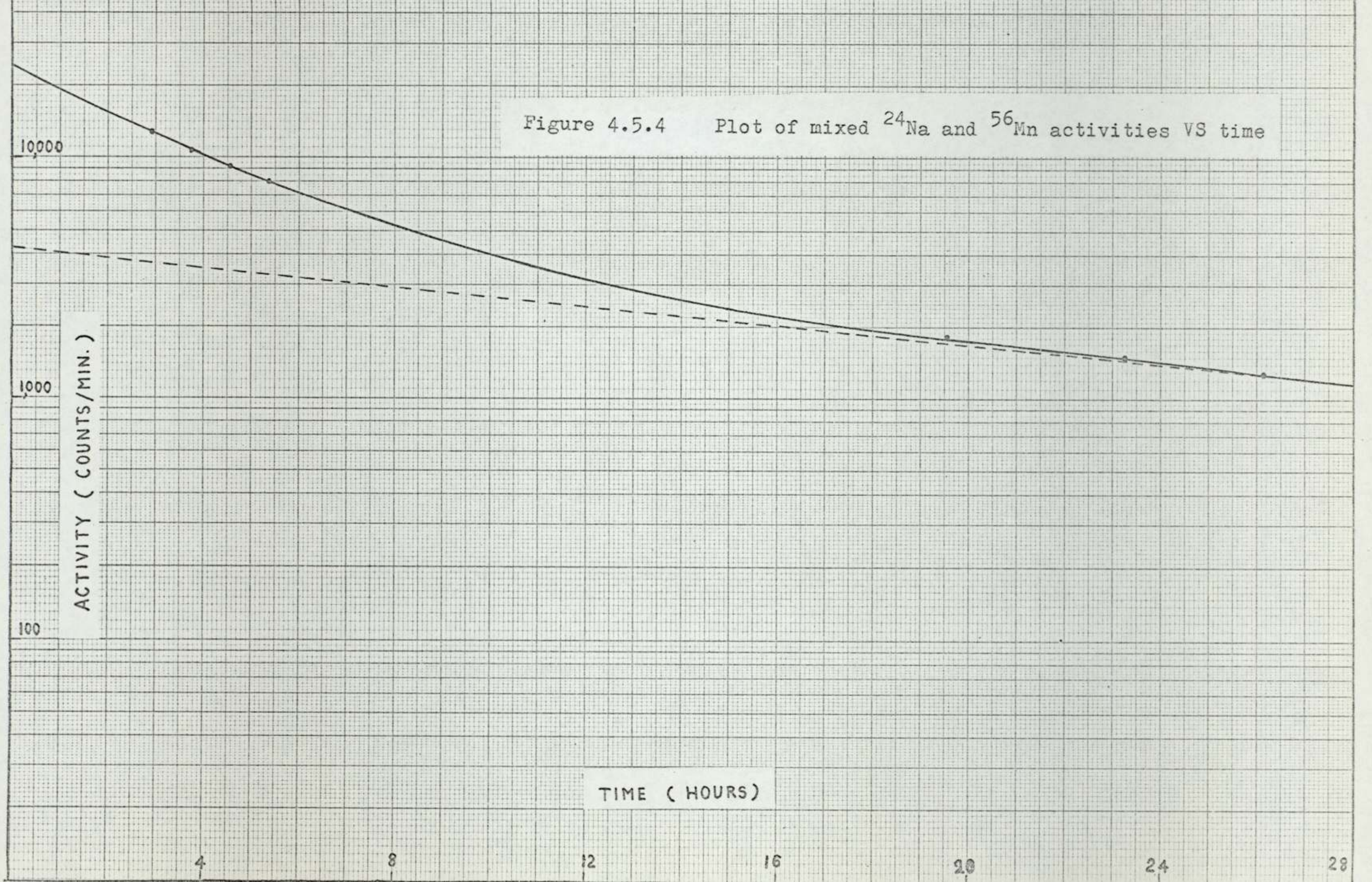

Figure 4.5.4 Plot of mixed $^{24}Na$ and $^{56}Mn$ activities VS time

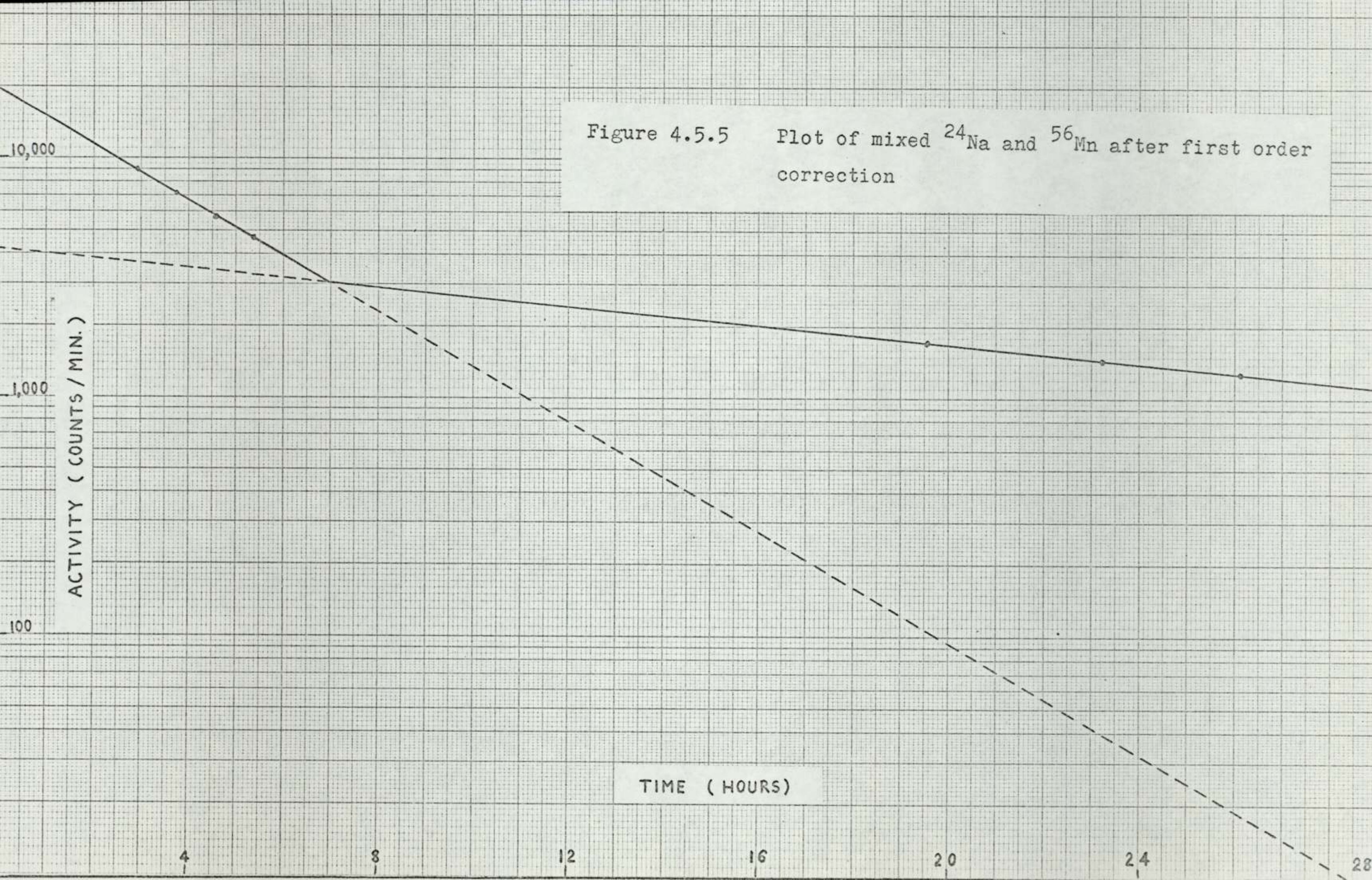

Figure 4.5.5 Plot of mixed $^{24}$Na and $^{56}$Mn after first order correction

and its percentage error.

### 4.6. Error assessment

The percentage loss of iron in various sintered samples was determined by comparing the induced activities between the sample and the standard assuming all other factors were identical. In practice, however, this condition was not always fully satisfied, since, for example, there was always some uncertainty in localising the source to detector geometry, sample and standard could not be made to have exactly the same density.

In this work no attempt was made to correct for these factors analytically. The effects of various factors were minimised by different methods described earlier. The errors introduced by assuming unity in the correction terms will be assessed for in this section.

We are looking for the answer in the form $\frac{A_1}{A_2} \Big/ \frac{B_1}{B_2}$ assuming all other factors being identical. Apart from the statistic of the counting each parameter has also other similar sources of errors some of which could be neglected. Since these errors are statistically independent of one another and assume that $A_1$, $A_2$, $B_1$, $B_2$ are also statistically independent of one another, the total relative errors can be divided into different groups each of which represents the total contribution from each of the four parameters involved.

### 4.6.1. Error propagation

Suppose the desired quantity is not experimentally accessible but can be computed from a set of experimental measurements, the evaluation of error in the computed quantity from errors in the measured quantities is called "propagation of errors".

The desired estimate of $M_o$ is the mean of a distribution $P(x_o)$; $x_o$ is not experimentally accessible, $x_o = f(x_1, x_2 \ldots)$ and therefore $M_o = f(M_1, M_2, \ldots)$. Each $M_i$ is the mean of a contribution $P_i(x_i)$ and all $x_i$'s are accessible to measurement Since the $M_i$'s are subjected to error so is the estimate of Mo.

The standard deviation of $M_o$ is determined approximately from errors in the experimental quantities as follows: (57)

$$\sigma^{2}(x_o) \approx \sum_i \frac{\partial M_o}{\partial M_i} \sigma^{2}(x_i) \qquad (4.6.1)$$

This expression applies if each $\frac{\sigma(x_i)}{M_i}$ is small (< ~20%) and if all $x_i$'s are statistically independent of one another. Some exaples of common function are given in Fig. 4.6.1.

### 4.6.2. Displacement transverse to the counter axis

Suppose the uncertainty in placing the disc source at the symmetry axis of the crystal is ± d cm.

For a cylindrical solid NaI(Tℓ) crystal of radius, $\tau$, and height, t, and suppose the disc source has radius R.

The detection efficiency for a disc source whose centre is at a distance, d, from the symmetry axis of the detector is approximately given by (58):

$$T(E) \approx T_c(E) + \frac{Ld^2}{\tau^2} + \frac{Md^2(2R^2 + d^2)}{\tau^4} \qquad (4.6.2)$$

$T_c(E)$ = efficiency for the disc source whose centre is at the axis of the detector.

L and M are coefficients which vary with gamma ray energy

Figure 4.6.1. Error propagation in common function

| Function | Standard deviation |
|---|---|
| 1. $M_o = M_1 \pm M_2$ | $\sigma^2(x_o) = \sigma^2(x_1) + \sigma^2(x_2)$ |
| 2. $M_o = \frac{M_1 M_2}{M_3}$ | $\sigma^2(x_o) \approx \frac{\sigma^2(x_1)}{M_1^2} + \frac{\sigma^2(x_2)}{M_2^2} + \frac{\sigma^2(x_3)}{M_3^2}$ |
| 3. $M_o = aM_1 + b$ | $\sigma^2(x_o) = a^2 \sigma^2(x_1)$ |
| 4. $M_o = M_1^{\tau}$ | $\frac{\sigma^2(x_o)}{M_o^2} \approx \frac{\tau^2 \sigma^2(x_1)}{M_1^2}$ |
| 5. $M_o = e^{\lambda M_1}$ | $\frac{\sigma^2(x_o)}{M_o^2} \approx \lambda^2 \sigma^2(x_1)$ |
| 6. $M_o = \log_e \lambda M_1$ | $\sigma^2(x_o) \approx \frac{1}{\lambda^2} \frac{\sigma^2(x_1)}{M_1^2}$ |

and source to detector separation distances.

$T_c$ could be expressed in terms of the detection efficiency for a pt. source. (59)

$$T_c(E) \approx T_p(E) + \frac{LR^2}{2\tau^2} + \frac{MR^4}{3\tau^4} \qquad (4.6.3)$$

Values of $T_p$, L and M have been tabulated in (59).

Hence $T_c$ can be found using the following values.

For d = .5 cm., $\tau$ = 2.54 cm.,, t* = 5.08 cm. and R = 1.45 cm.

E = .835 MeV.

L, M were found to be

- .06288661 and - .00827057 respectively.

---

*t = thickness of the crystal

Hence $T(.835) \approx T_c - .00009747 - .00005246$

Using $T_c = .158$

$$T_E \approx .15785$$

Hence the error introduced due to uncertainty in placing the source at the symmetry axis of the crystal is amounted to .1% for a .835 MeV $\gamma$-ray. Similar result was also obtained for the 1.37 MeV.

### 4.6.3. Neutron self-shielding

Consider the case of two samples of 5% different in effective thickness.

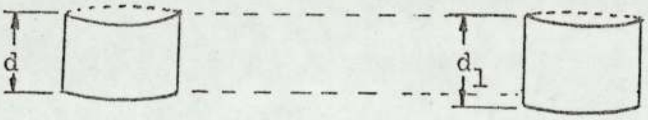

The neutron fluxes at the bottom faces of the two samples are not the same. They were assumed in the calculation to be identical. The error involved in this assumption can be estimated by calculating the percentage difference in the fluxes at thickness d and $d_1$.

Let $\phi_o$ be the flux at the front surface

$\phi_x$ be the flux at depth x

$$\phi_x = \phi_o e^{-\Sigma_r x} \qquad (4.6.4.)$$

where $\Sigma_r$ = the macroscopic removal cross section, $cm^{-1}$

$$\Sigma_r = N_o \sigma_r \qquad (4.6.5.)*$$

$\sigma_r$ = the microscopic removal cross section, barn/atom

For mixture of elements in material

$$\Sigma_r = \sum_y N_y \sigma_{ry}(E) \qquad (4.6.6.)$$

From the available data (60) of $\sigma_r$ at 14 MeV, the percentage

---

*No = no. of atoms per cc.

difference in neutron flux at two different depths was found to be .25%. This figure represents the maximum error in the case where samples were not uniformly mixed and the two oxides were distributed in separate layers. In this experiment this error could be assumed to be less than .1% on the average.

### 4.6.4. Sample preparation error

Small amount of error introduced during the process of mixing and grinding due to material sticking to container and grinding ball. The error was found by weighing to be about .2%.

### 4.6.5. Self absorption of $\gamma$-rays

Consider the case where sample and standard are of 5% difference in density. The error involved in neglecting the effect due to self absorption of $\gamma$-ray can be estimated since the absorption of $\gamma$-ray follows an exponential law. In this experiment the thickness of the sample was much smaller than the diameter which in turn was smaller than the crystal. Then we have

$$\frac{C_d}{C_o} = \frac{1 - e^{-\sigma t}}{\sigma t} = A \qquad (4.6.6.)$$

$C_d$ = observed count rate for sample of thickness t cm.

Co = counting rate which would have been observed in the absence of self-absorption.

$\sigma$ = linear absorption coefficent, $\text{cm}^{-1}$.

For a sample of a mixture of elements the absorption factor is given by;

$$A = \frac{1 - e^{-\sum_i (\mu_i) \left(\frac{W_i}{V}\right) t}}{\sum_i (\mu_i) \left(\frac{W_i}{V}\right) t}$$

$V$ = volume of sample, cc.

$W_i$ = weight of element i, gm.

$\mu_i$ = mass absorption coefficent of element i, $\frac{\text{cm.}^2}{\text{gm.}}$

Using the tabulated values of $\mu$ (61) and considering the case of two samples of 5% difference in density, the error was found to be .1%.

### 4.6.6. Counting interval

Both counting intervals employed in the measurements were about $\frac{1}{15}$ and $\frac{1}{21}$ of the half lives respectively, hence the activity was calculated at the mid-point of counting interval with negligible error.

Consider a radio active substance containing No atoms at $t = o$ and decaying with decay constant $\lambda$ and half life $t_{\frac{1}{2}}$. Then at time t the no. of atoms surviving will be

$$N = No e^{-\lambda t} \qquad (4.6.8)$$

What is measured in the laboratory is the no. of decays $\Delta N$ during the time interval $\Delta t$ for a succession of $\Delta t$ intervals. Each value of $\frac{\Delta N}{\Delta t}$ is then plotted at the mid point of the corresponding time interval. Since $\lambda \Delta t$ is small, this graph is a good approximation to the exact $\frac{dN}{dt}$ graph.

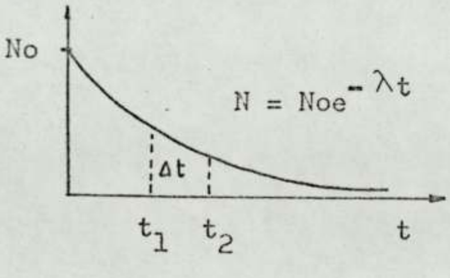

To get an accurate graph the measured value of $\frac{\Delta N}{\Delta t}$ should be plotted at the point between $t_1$ and $t_2$ where $\frac{\Delta N}{\Delta t} = \frac{dN}{dt}$.

Suppose the above condition exists the value of t which satisfies it can be determined, let the quantity $\Delta N$ be the change in N

Now $\frac{dN}{dt} = \frac{\Delta N}{\Delta t}$

From (4.6.8) we get

$$-\lambda No e^{-\lambda t} = \frac{No e^{-\lambda t_2} - No e^{-\lambda t_1}}{\Delta t} \qquad (4.6.9)$$

Multiply Eq. (4.6.9) by $\frac{\Delta t e}{No}^{\lambda(t_1 + t_2)/2}$ we get

$$-\lambda \Delta t \, e^{-\lambda[t - (t_1 + t_2)/2]} = e^{-\lambda(t_2 - t_1)/2} - e^{\lambda(t_2 - t_1)/2}$$

$$= e^{-\lambda \Delta t/2} - e^{\lambda \Delta t/2} \qquad (4.6.10)$$

Since $t_2 - t_1 = \Delta t$ and assuming $\lambda \Delta t$ to be small, the R.H.S. of Eq. (4.6.10) can be expanded in power series, this gives

$$-\lambda \Delta t e^{-\lambda [t-(t_1 + t_2)/2]} = \lambda \Delta t - \frac{1}{3} (\lambda \frac{\Delta t}{2})^3 \, ......... \qquad (4.6.11)$$

$$e^{-\lambda [t - (t_1 + t_2)/2]} = 1 + \frac{1}{24} (\lambda \Delta t)^2 \, ...... \qquad (4.6.12)$$

Hence from (4.6.12) we get

$$-\lambda(t - \frac{t_1 + t_2}{2}) = \text{In}[1 + \frac{1}{24} (\lambda \Delta t)^2 ......]$$

Since $\frac{1}{24} (\lambda \Delta t)^2 << 1$ the logarithm can be expanded

$$-\lambda(t - \frac{t_1 + t_2}{2}) \approx \frac{1}{24} (\lambda \Delta t)^2$$

$$t = \frac{t_1 + t_2}{2} - \frac{1}{24} (\lambda \Delta t^2)$$

For $\Delta t = 10$ mins. and $\lambda = \frac{0.193}{2.58}$

$$\frac{1}{24}(\lambda \Delta t^2) = .003$$

For $\Delta t = 40$ mins. and $\lambda = \frac{0.693}{15}$

$$\frac{1}{24}(\lambda \Delta t^2) = \cdot 0002$$

$\therefore$ there is negligible error in plotting $\frac{\Delta N}{\Delta t}$ at the mid point of the corresponding time interval.

## 4.7. Results and discussion

Several observations were made for each of the samples and results are shown in the Fig. 4.6.2 where the Mg to Fe ratio relative to the standard is expressed as a percentage excess of magnesium. These figures are therefore directly comparable with the parameter x (when this is expressed as a percentage) in the formula $(MgO)_x \cdot MgFe_2O_4$ used by Paladino except that no claim concerning the oxygen content is made in this case.

Although the measurements do not reveal information concerning oxygen content it is clear that present results are consistent with the earlier conclusions drawn by Paladino. His equilibrium value for x is some what higher than the average magnesium excess given here, however it is note worthy that within the experimental uncertainty this excess is also independent of sintering temperatures at least up to 1400 C.

It is also evident that the present results do not support Reijnen's claim for the existence of stoichiometric $MgFe_2O_4$ spinel in spite of the fact that his recommendation concerning preparation was strictly followed.

Figure 4.6.2. Mg to Fe ratio relative to equimolar standard

| Specimen | Magnesium excess (%) | Average |
|---|---|---|
| Check sample with 5% Mg excess | | |
| 1) | 5.4 ± 2 | |
| 2) | 5.8 ± 1.6 | |
| Check sample with 5% Mg deficiency | | |
| 3) | -3.3 ± 1.3 | |
| 4) | -4.2 ± 1.3 | |
| 5) | -3.7 ± 1.4 | |
| 6) | -4 ± 1.4 | |
| 7) | -4.7 ± 1.2 | |
| Sample sintered at 1100° | | |
| 8) | 7 ± 1.3 | 6.9 ± 0.9 |
| 9) | 6.8 ± 1.2 | |
| Sample sintered at 1200° | | |
| 10) | 6 ± 1.4 | 5.7 ± 0.8 |
| 11) | 5.1 ± 1.4 | |
| 12) | 6 ± 1.2 | |
| Sample sintered at 1400° | | |
| 13) | 6.7 ± 1.4 | 6.3 ± 0.8 |
| 14) | 5.8 ± 1.4 | |
| 15) | 6.5 ± 1.4 | |

# CHAPTER V ANALYSIS OF FLUORINE IN MICROCRACKED CHROMIUM BY METHOD OF PROMPT $\gamma$-RADIATION DETECTION

## 5.1. Introduction

The second problem studied was the possible incorporation of fluorine in chromium plating when fluorine salts are included in the plating bath.

Bright chromium electro-deposits may be obtained by electrolysis of solutions containing essentially a chromic acid, $CrO_3$, and sulphuric acid, $H_2SO_4$, using an insoluble lead anode. Addition agents such as silicofluorides result in a microcracked deposit at a thickness of about 2 microns. The chromium deposited has a continuous and uniform net work of cracks (Fig. 5.4.1). When this microcracked chromium is used as a top layer in a decorative nickel plus chromium coating, the nickel can be attacked at many of the cracks instead of a few isolated points. Whilst this does not prevent attack of the nickel it does provide a large anode area so that corrosion is spread out over a large area and the nickel is not penetrated so rapidly.

The mechanism of electrodeposition of microcracked chromium is not fully established although it is known that the deposit is highly stressed, relief occuring through microcracking. From other work (62) it is thought that the fluoride breaks down and there is the possibility of incorporation into the deposit. Break down of the fluoride would mean that it does not function as a true catalyst in similar manner to the sulphuric acid where break down does not occur.

A suggested break down mechanism of fluoride is;

$F^- + H^+ \rightleftharpoons HF$ below pH4

$4HF + S_iO_2 \rightarrow 2H_2O + S_iF_4$ ($S_iO_2$ from glass)

$3S_iF_4 + 2H_2O \rightarrow 2H_2S_iF_6 + S_iO_2$

It has been found that $SiO_2$ is formed from fluoride containing chromium plating solutions when used over a period of several hours.

It is thus of considerable interest to determine the relative quantity of fluorine on the surface and its possible depth of penetration in microcracked chromium. The analysis of fluorine by means of the nuclear reaction $^{19}F(p, \alpha \gamma)^{16}O$ has been done by several workers (22) (23) (25) (26) (27) since this reaction has a higher yield of $\gamma$- radiation for incident protons with energy of less than 1 MeV than any other proton induced reactions. Below 500 KeV the intense and narrow resonance at 340 KeV permits the study of depth distribution of the fluorine below the surface by varying the proton energy.

## 5.2. Theory of method

Consider the reaction of fluorine with 500 KeV protons. In this energy region the proton interacts predominantly with the fluorine-19 via the reaction $^{19}F(p, \alpha)^{16}O$ for which three resonances are observed for proton energies at 224, 340.5 and 485.6 - KeV. The resonance at 340.5 KeV is the most intense and the oxygen-16 deexcites largely by the emission of $\gamma$-rays energies 6.13 and 7.1 MeV.

The characteristics of these resonances shown in Fig. 5.2.1 are extracted from the table prepared by Bewers and Flack (27) for the determination of fluorine by prompt $\gamma$-radiation from proton bombardment based on the compilations of Ajzenbury-Selove and Lauritsen (63) and Marion (64).

Figure 5.2.1. Resonances for 6 to 7 MeV $\gamma$-rays in $^{19}F(p, \alpha\gamma)^{16}O$ from 500 KeV proton

| Ep(KeV) | $\sigma$(mb.) | $\Gamma^*$(KeV) | Relative component intensities<br>6.13 MeV | <br>7.1 MeV |
|---|---|---|---|---|
| 224 | 0.2 | 1.0 | - | - |
| 340.5 | 102 | 2.4 | 0.96 | 0.04 |
| 483.6 | 32 | 0.9 | 0.8 | 0.2 |

* $\Gamma$ is the width of resonance at half-maximum intensity

Consider the resonance at 340 KeV the yield of the characteristic $\gamma$-rays can be shown to be related to the number of fluorine atom in the target sample. According to Fowler, Lauritsen and Lauritsen (65) the yield from the target is obtained by integration of the Breit-Wigner dispersion formula over the energy interval represented by the loss in the target.

For a target of thickness $\Delta x$, corresponding to the loss of energy $\xi$, the yield, Y, of $\gamma$-rays per incident proton is given by

$$Y = \int_{E-\xi}^{E} \frac{N\sigma}{dE/dx} \, dE \qquad (5.2.1)$$

where N = number of disintegrable nuclei per unit volume

E = incident proton energy

$\frac{dE}{dx}$ = stopping power of the medium

Define the stopping cross section for the incident protons per disintegrable fluorine-19 nucleus, $\epsilon$, by

$$\epsilon = \frac{1 dE}{N dx} \qquad (5.2.2)$$

Assume that the Breit-Wigner resonance equation is used, neglecting wave length and penetrating factor,

$$\sigma = \sigma_R \frac{\Gamma^2/4}{(E-E_R)^2 + \Gamma^2/4} \qquad (5.2.3)$$

where $\sigma_R$ = cross section at the resonance energy, $E_R$ substituion for $\sigma$ and $\epsilon$ in Eq. (5.2.1), then, assuming that

$$Y = \int_{E-\xi}^{E} \frac{\sigma_R \quad \Gamma^2/4}{\epsilon \; (E-E_R)^2 + \Gamma^2/4} dE \qquad (5.2.4)$$

$\epsilon$ and $\xi$ are constant over the resonance, integration of Eq. (5.2.4.) gives

$$Y = \frac{\sigma_R \Gamma}{2\epsilon} \left[ \tan^{-1} \frac{E-E_R}{\Gamma/2} - \tan^{-1} \frac{E - E_R - \xi}{\Gamma/2} \right] \qquad (5.2.5)$$

For a target which is thick compared to the range of proton, putting $\xi = E$, then approximately

$$Y = \frac{\sigma_R \Gamma}{2\epsilon} \left[ \tan^{-1} \frac{E-E_R}{\Gamma/2} + \frac{\pi}{2} \right] \qquad (5.2.6)$$

For a given $\xi$, the maximum of Eq. (5.2.5) lies at

$$E_{max} = E_R + \xi/2 \qquad (5.2.7)$$

Hence at this value

$$Y_{max}(\xi) = \frac{\sigma_R \Gamma}{\epsilon} \tan^{-1} \xi/\Gamma \qquad (5.2.8)$$

For a thick target the maximum yield or full step in the thick target curve is

$$Y_{max}(\infty) = \frac{\pi}{2} \quad \frac{\sigma_R \Gamma}{\epsilon} \qquad (5.2.9)$$

For a given resonance, $\sigma_R$ and $\Gamma$ are constants which are independent of the compositions of the sample. In most analysis of materials the sample is "thick" the yield is then inversely proportional to the stopping cross section. The constancy of the term $\epsilon Y$ in Eq (5.2.9) has been verified experimentally by Bewers and Flack (66).

In the special case where the effective thickness of the sample is comparable to the natural width, $\Gamma$, application of Eq. (5.2.8) requires knowledge of the target thickness. Provided the resonance curve is narrow and symmetric the thickness of the target can be evaluated (section 5.6.3) from the observed width $\Delta E$, and the natural width of the resonance from

$$\Delta E^2 = \Gamma^2 + \xi^2 \qquad (5.2.10)$$

Basically, by measuring the $\gamma$-rays yield and applying the above equations the quantity of fluorine in the particular sample can be determined.

## 5.3. Counting assembly

The 6 and 7-MeV gamma rays were detected by a 4 x 4-inch NaI(T$\ell$) scintillation crystal. In the NaI(T$\ell$) phosphor the pulse height per MeV is nearly independent of electron energy, any combination of processes by which the $\gamma$-ray is completely absorbed in the phosphor produces the same pulse height. The probability of multiple processes to occur increases with the increased in size of the crystal hence a large crystal was chosen.

The crystal was mounted as shown in Fig. 5.3.1. onto an 11-stage E.M.I. photomultiplier tube No. 9530B, which has a CsSb secondary emitting surface. The photo cathode was 5 inches in diameter and the tube employs venetian blind dynode system. This structure has a good efficiency for collecting photo electrons because of its large effective surface area.

The tube and crystal were optically coupled with a non-drying immersion oil of refractive index as near as possible to the refractive index of the glass which was 1.75. A 5.7inches diameter mu-metal shield was used to minimise the effect of external magnetic field variation. The photo multiplier tube was spring loaded against the crystal surface to ensure that the optical joint was not disturbed. The complete assembly was mounted in a light tight aluminium container.

### 5.3.1. Electronics for the counting system

The photomultiplier tube was operated in a conventional manner with cathode at earth potential. The voltages for the dynodes of the photomultiplier were obtained from a chain of resistors across a high voltage source. The non-linear dynode chain employed is shown in Fig. 5.3.2. A zener diode stabiliser was inserted between the cathode and first dynode to obtain an adequate voltage, regardless of changes in the chain current. The tube was operated in the 1100 volt region. In this region the pulse height was found to be most linear.

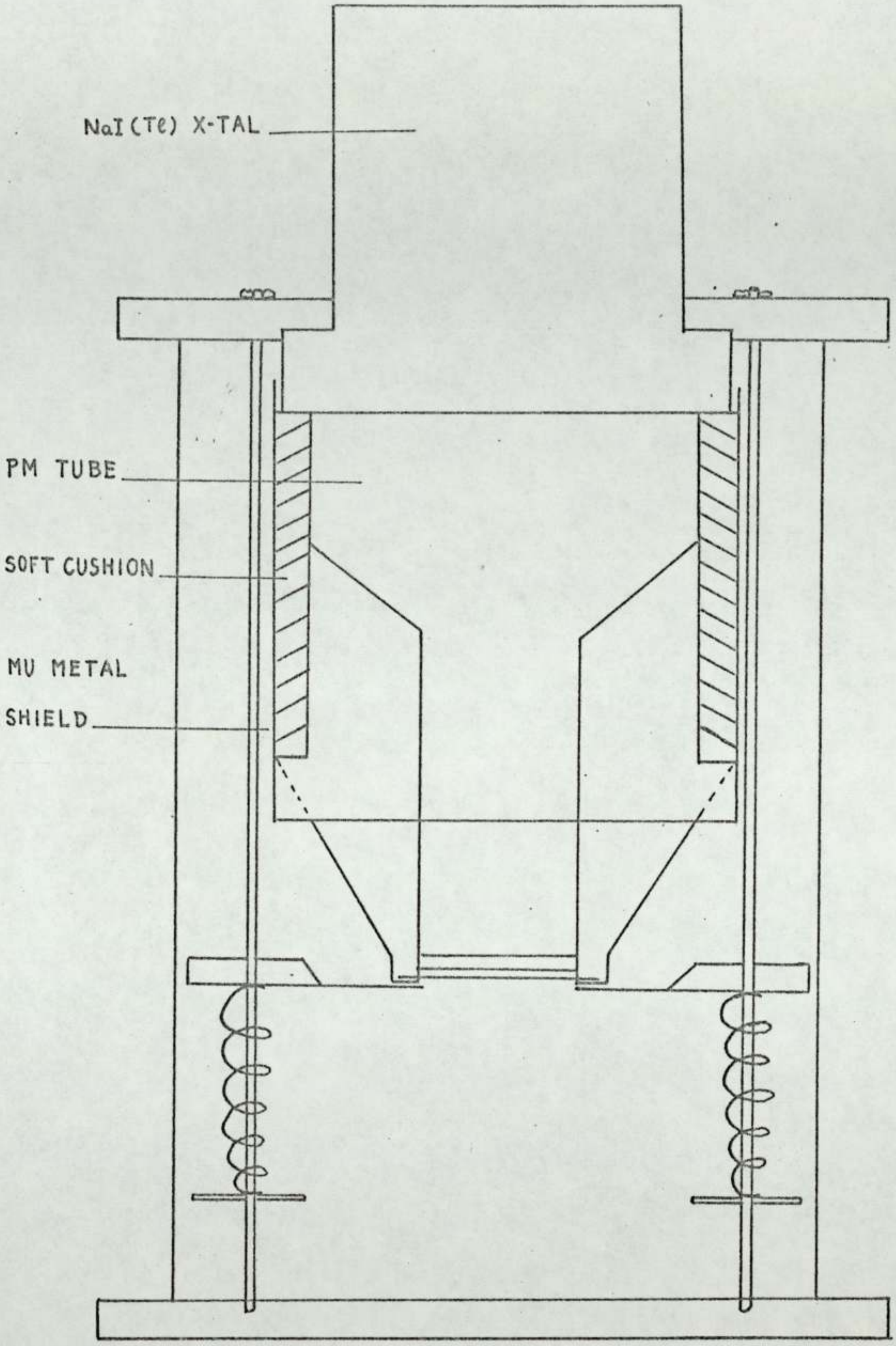

Figure 5.3.1 4x4-inch NaI(Tl) scintillation detector assembly

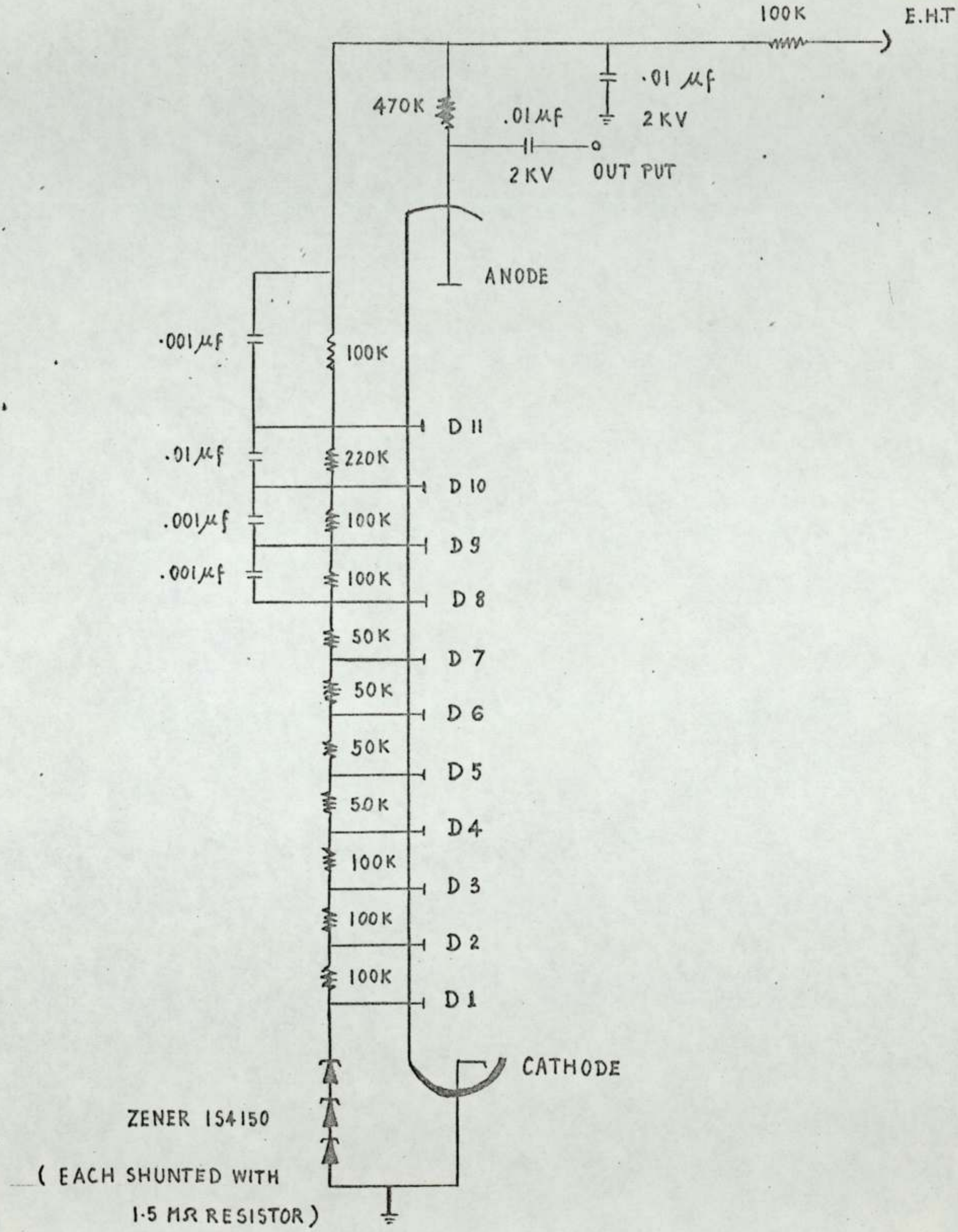

Figure 5.3.2    Dynode chain circuit

Figure 5.3.3

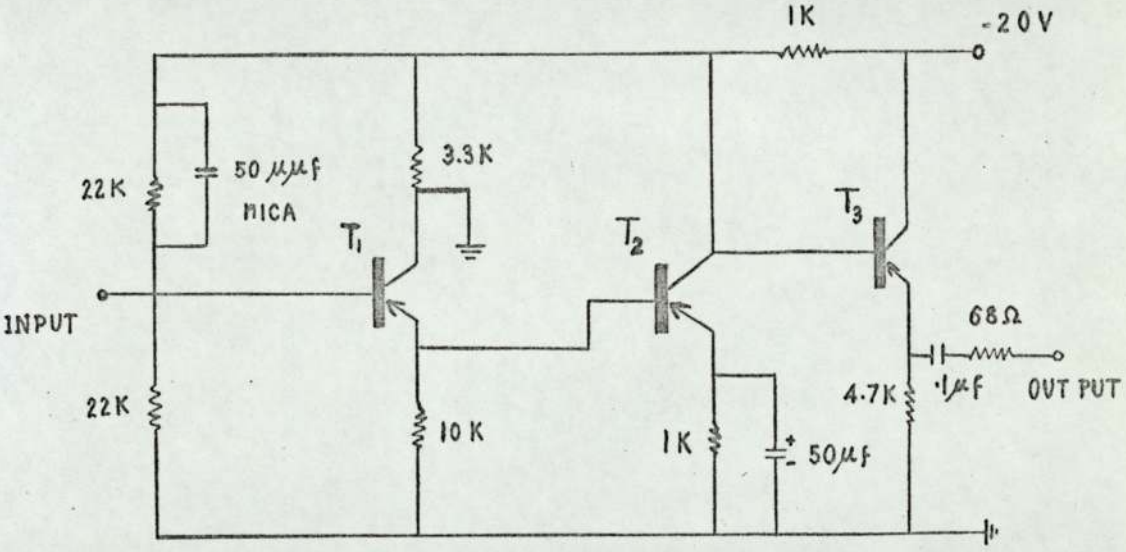

Figure 5.3.4     Preamplifier circuit

The output signal was fed into a modified R.I.D.L Charged sensitive preamplifier and then into a 400 multichannels analyser Fig5.3.3. Fig. 5.3.4. shows the circuit of the preamplifier.

### 5.3.2. Detector performance

The detector response was initially checked with standard $^{60}Co$ source the spectrum of which is shown in Fig. 5.3.5. The detector exhibits a resonable degree of resolution as indicated by the well resolved peaks of the two $^{60}Co$ $\gamma$-rays, which has a peak to valley ratio of 1.74 : 1.

Measurements of the pulse-height resolution were made for various $\gamma$-rays and the square of the resolutions were plotted in Fig. 5.3.6. as a function of the inverse of the energy. Extrapolation of the portion of the curve found between 0.5 MeV and 3 MeV yield a positive intercept on the y-axis of 4.4% indicating that with no variance due to cathode statistics and with energy uniformly deposited in the crystal, the line width would be that value found at the positive intercept. A high "infinite" energy intercept value would, then, to a certain extent, mean poor cathode response uniformity or crystal inhomogeneity.

### 5.4. Experimental targetry

To facilitate the experimental arrangement microcracked chromium target was prepared by electrodepositing on to the copper disc, 2.2 cm. diameter and 1.2 cm. thick. The disc was machined from spectrographically pure copper and had a 6 BA tapped hole in the back for mounting purposes.

The surface to be electrodeposited was first polished

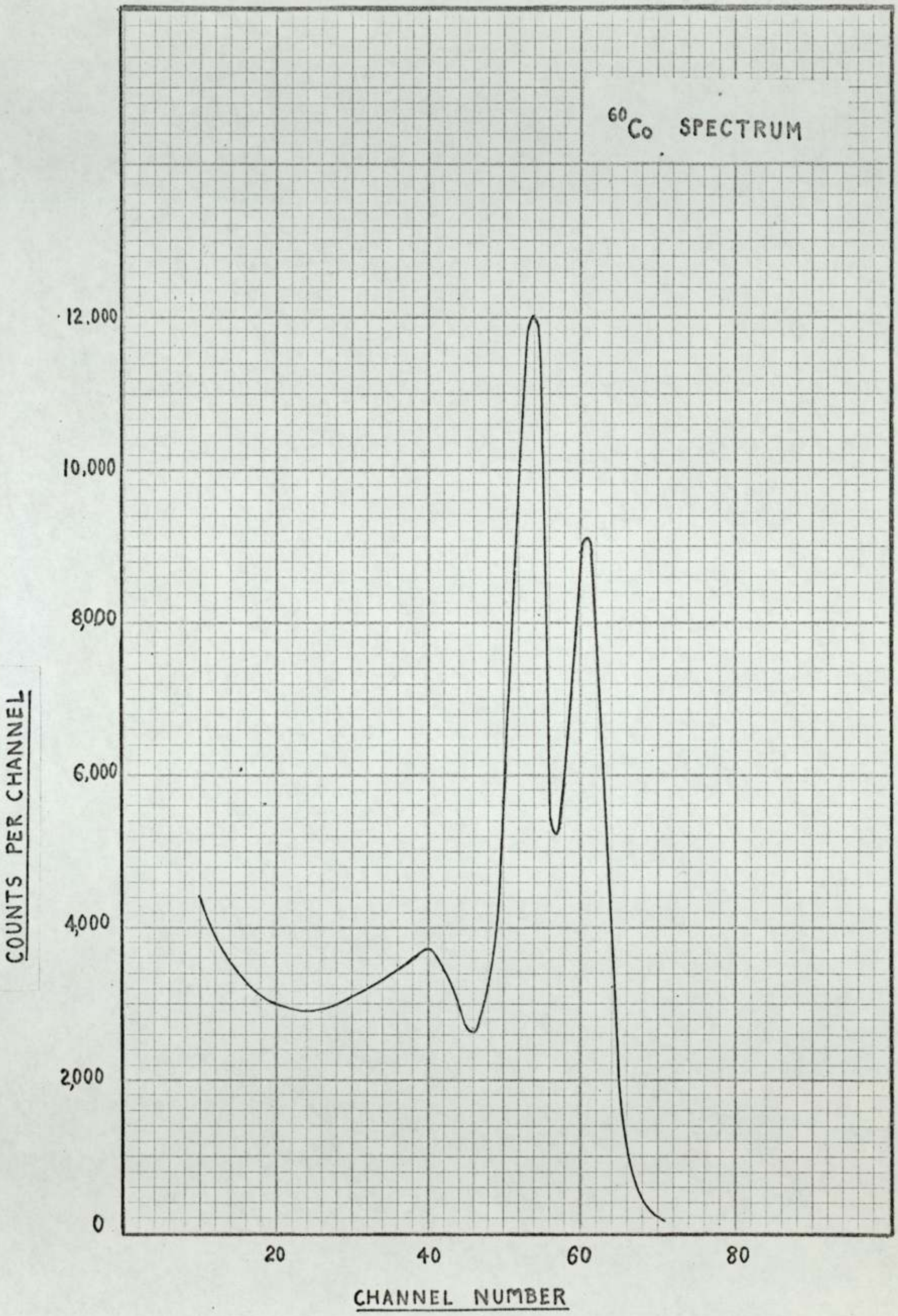

Figure 5.3.5 $^{60}$Co Spectrum

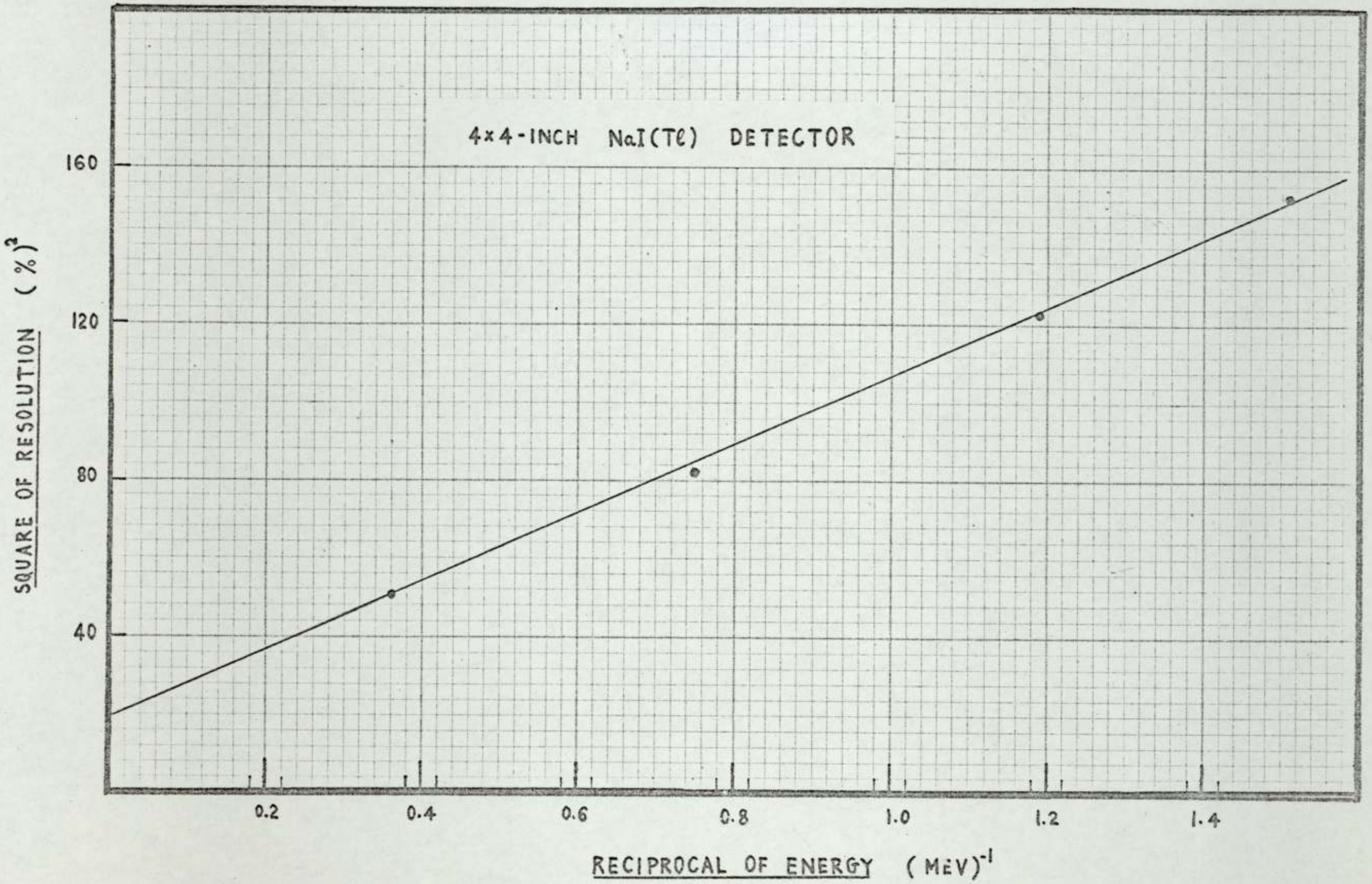

Figure 5.3.6 Plot of square of resolution VS reciprocal of gamma ray energy

carefully until bright surface obtained, the disc was then cleaned with acetone and rinsed in hot water. Normal procedure for cleaning the cathode was then applied electrolytically in a proprietary cleaning solution.

The following data was used to prepare the plating solution

| | |
|---|---|
| 150 gm./l | $CrO_3$ |
| 0.35 gm./l | $H_2SO_4$ |
| 3.00 gm./l | NaF |

Plating conditions: 14 amp./dm.$^2$ for 20 min. at 46°C.

Plating was done in a glass beaker for 40 min. on a dummy cathode before plating on a polished copper cathode. The disc was removed after 20 mins. and rinsed in hot water. The chromium deposit had a continuous and uniform net work of cracks as shown in Fig. 5.4.1.

### 5.4.1. Thick $CaF_2$ target

To establish a thick target yield curve the $CaF_2$ target was prepared by vacuum evaporation of known weight of $CaF_2$ onto a copper backing, from a small molybdenum boat. The preparation of backing material was similar to that described in the previous section. The quantity of material in mgm. per cm.$^2$ equivalent to a given target thickness, $\xi$, was determined from the values of the stopping cross section, $\epsilon$, compiled by Whaling (67) (Fig. 5.4.2.)

In most cases the targets prepared were thick i.e. $\xi \gg \Gamma$ and the target thicness was calculated by assuming that the source evaporated isotropically over the upper hemisphere. The targets thus prepared were stored in a dessicator until used.

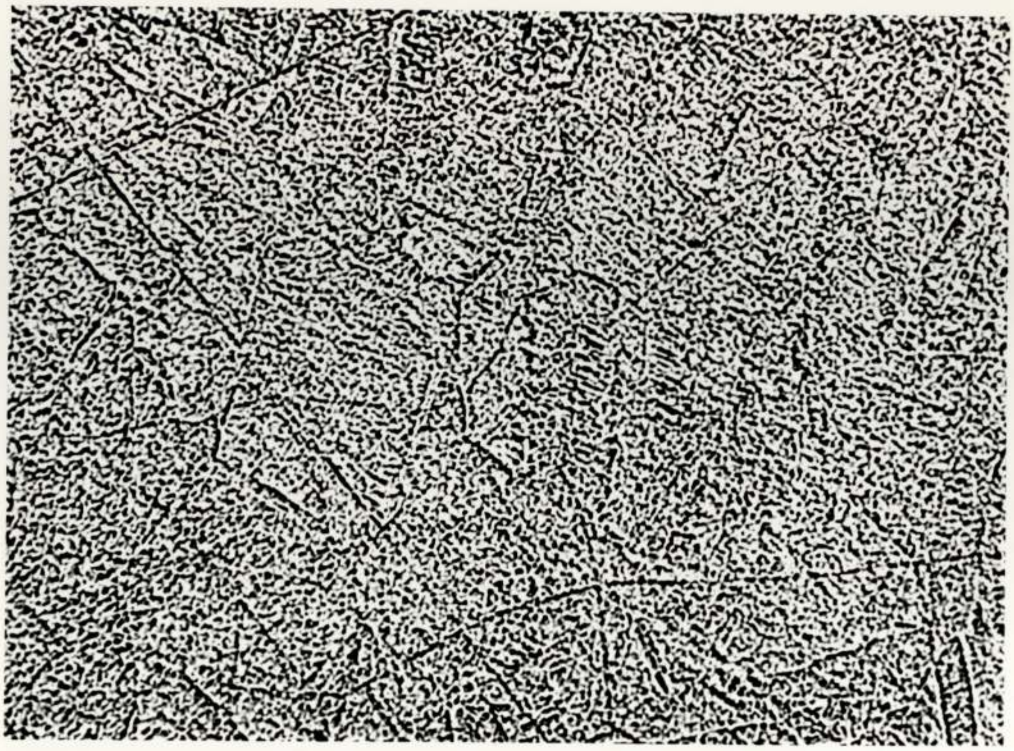

(A)

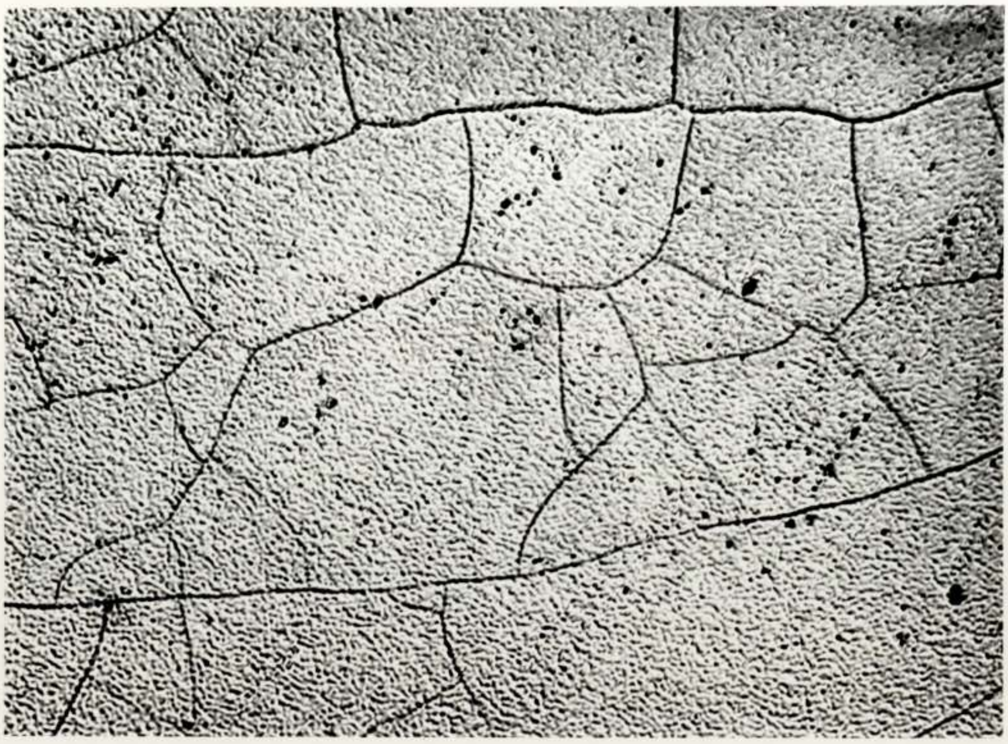

(C)

Figure 5.4.1

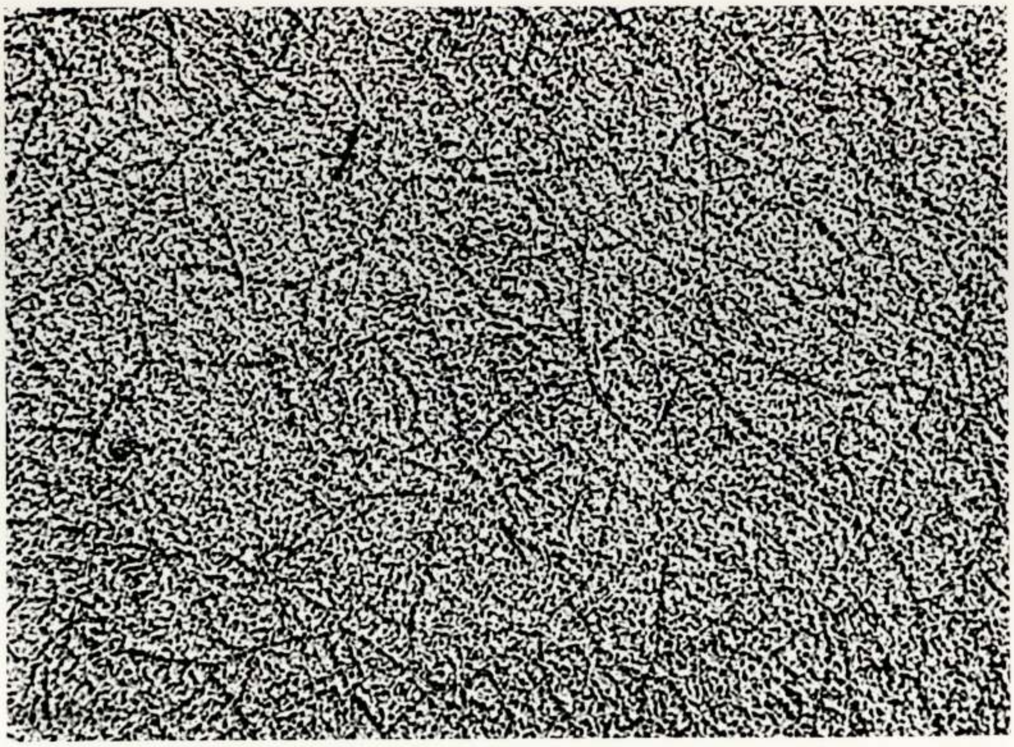

(D)

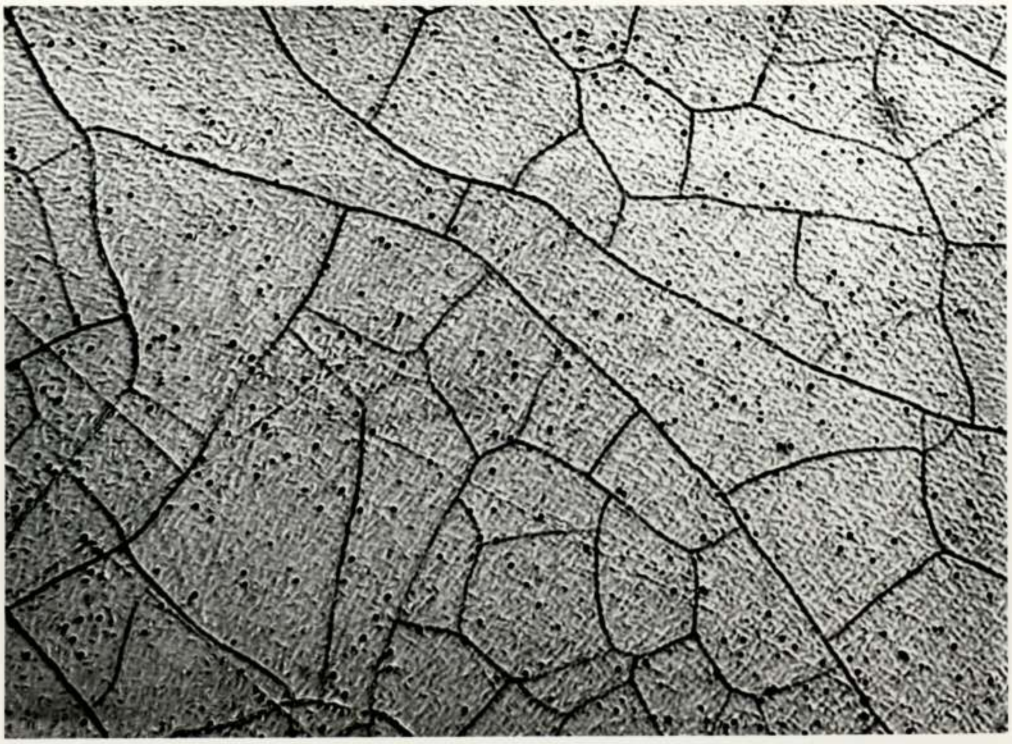

(G)

Figure 5.4.1

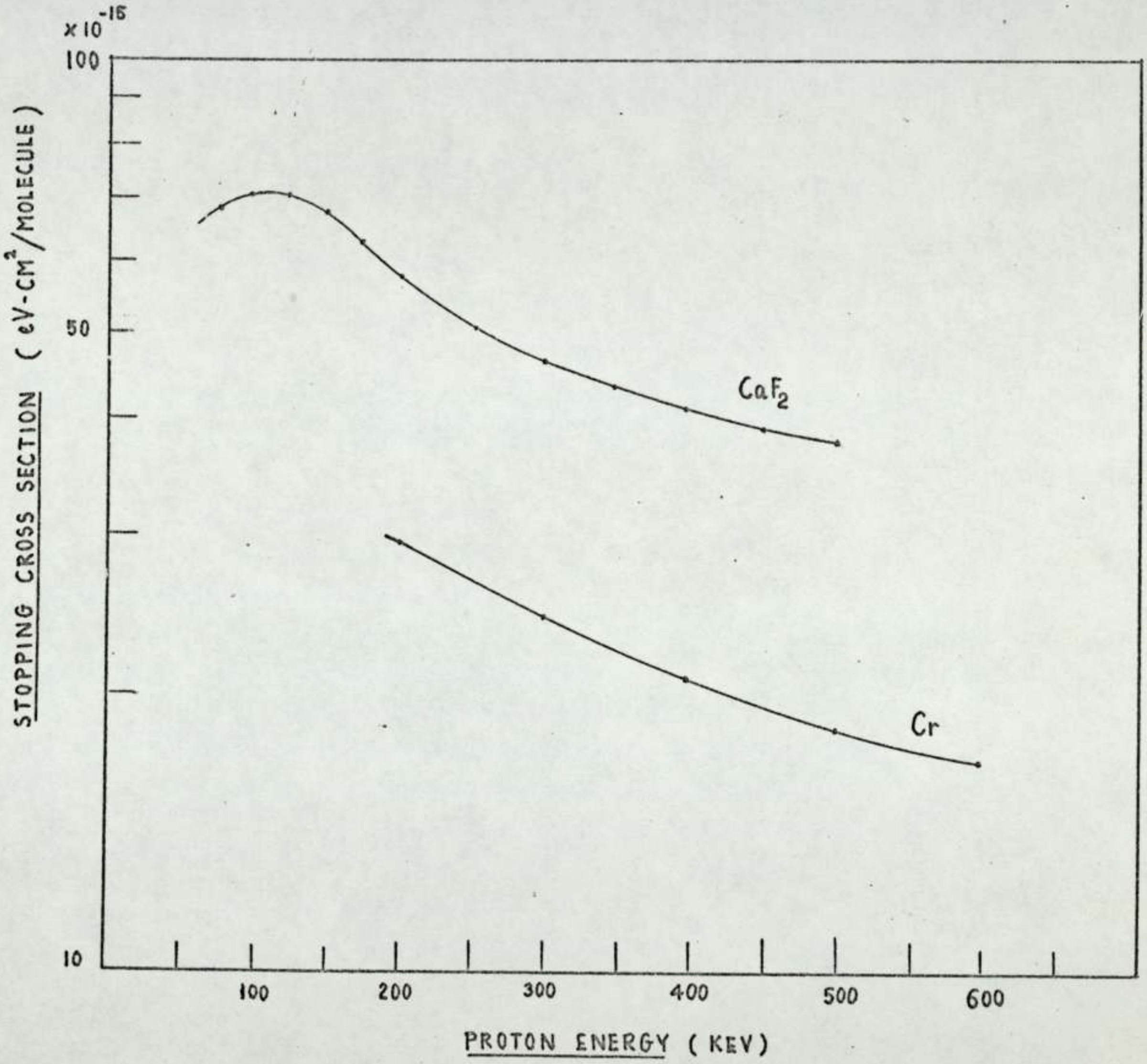

Figure 5.4.2 Stopping cross section curve for $CaF_2$ and Cr

## 5.5. Experimental method

The prepared target was mounted inside the vacuum chamber as shown in Fig. 5.5.1. The mounting of the target inside a small extended flight tube allowed the target to be changed without breaking the vacuum of the whole system in less than 5 min. A diaphragm made from spectrographically pure copper was placed in front of the target with a 1 cm. diameter hole bore through to define the ion beam on to the target only. A 250 V negative voltage was applied to the diaphragm and reduced the effect of secondary emission of electrons from the target. A liquid nitrogen trap was placed 50 cm. away to reduce hydrocarbon vapour pressure in the vicinity of the target and hence minimise carbon built up on the target surface.

### Monitoring electronics

The 6 and 7 MeV $\gamma$-rays were observed by a 4 x 4-inch NaI(T $\ell$) detector at 180° and 10.5 cm. away (Fig. 5.5.2). In this position the effect of source-detector geometry was minimised. The amount of charge deposited upon the target was recorded using a beam current integrator which enabled the $\gamma$-emission to be related to the charges deposited. Beam current integrator output (1 pulse per $\mu$ coul. of charge deposited ) was amplified and fed into a scaler and timer unit. The 400 channels pulse height analyser was switched off when the predetermined target charge had accummulated.

### Beam energy analyser

Ionisation of hydrogen gas with a Thonemann (37) Radio Frequency source produced a beam of monatomic, diatomic and

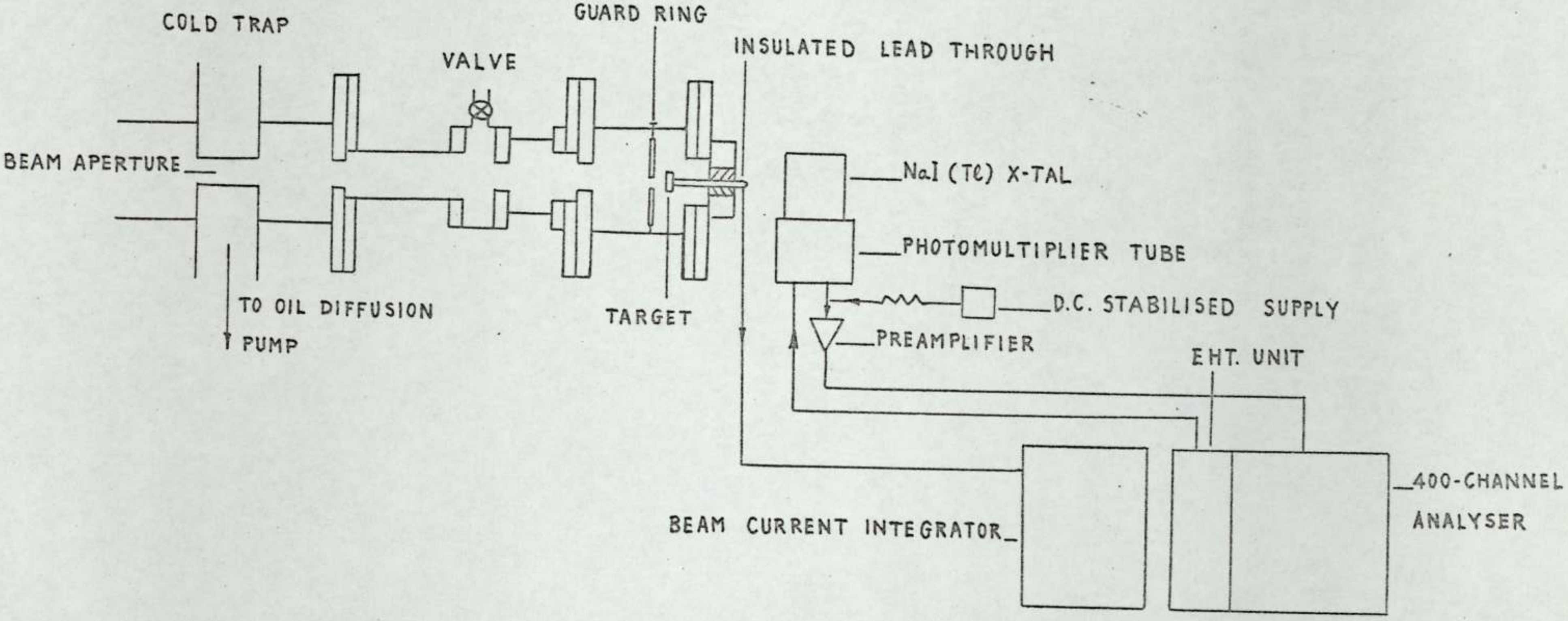

Figure 5.5.1 Sectional view of the target mounting facilities and monitoring electronics

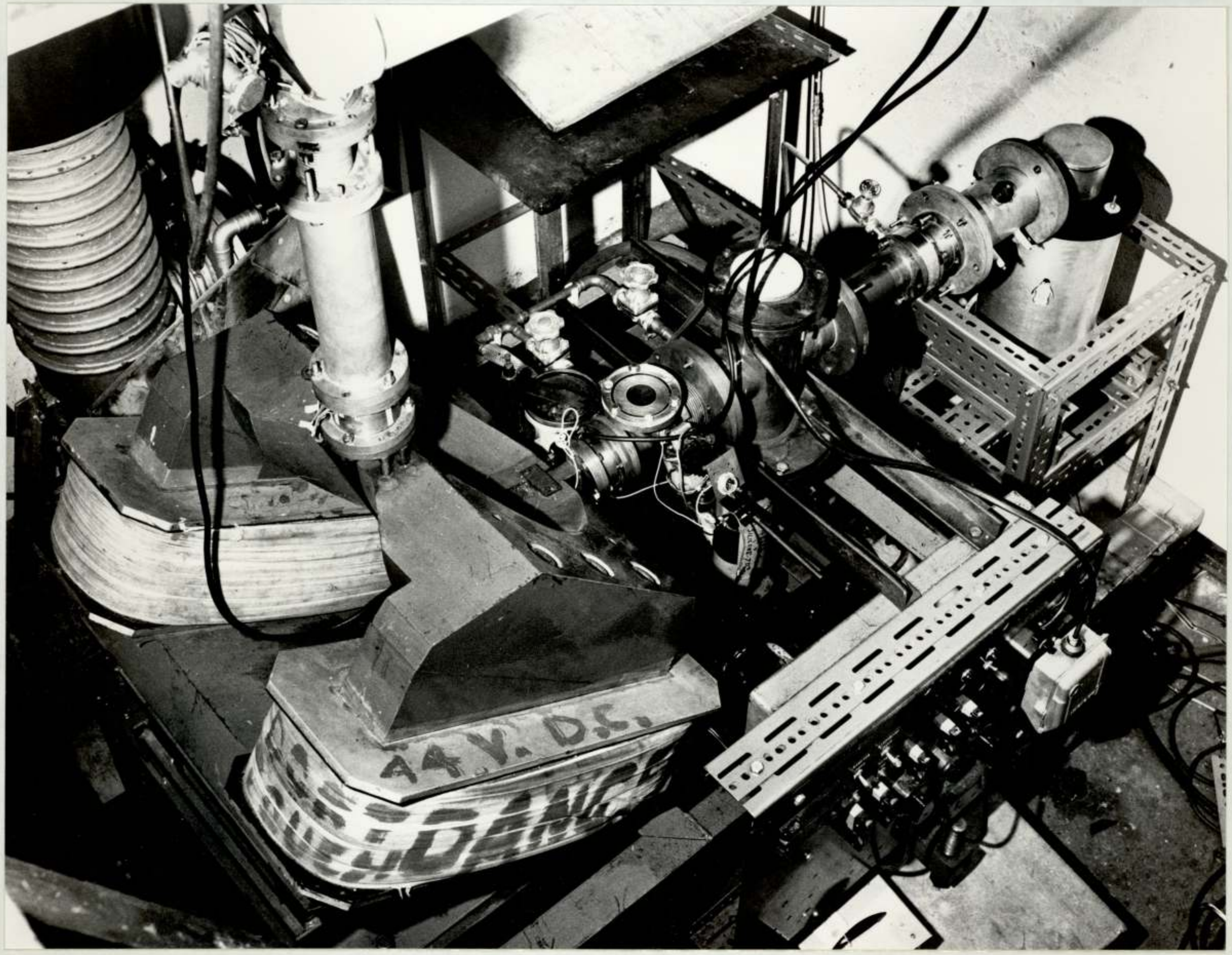

Figure 5.5.2

triatomic ions of mass equal to one proton mass, mp, $(2 + \frac{1}{1840})$ mp and $(3 + \frac{2}{1840})$ mp respectively. Protons were selected from mixed mass beam by using a $90^\circ$ magnetic deflector since the radius of curvature, R, of the path of the ions is related to the flux density, B, and the accelerating voltage, V, by:

$$R = \frac{1}{B}\sqrt{\frac{2Vm}{e}} \qquad (5.5.1)$$

where m = mass of the ion

e = electronic charge.

The exciting current for the electromagnet coils was variable and obtained from a 36 volt D.C. battery supply. Two sets of four adjustable electrodes were positioned at the entrance and the exit of the bending magnet. The exit aperture was used for energy stabilisation and resolution (30).

### Energy resolution

Consider three rays of radius R passing through the system as shown in Fig. 5.5.3. The focussing of these rays provides a natural exit aperture.

Denote the width of the entrance aperture by $\omega_1$, and the width of the exit aperture by $\omega_2$, then

$$\frac{\omega_1/2}{\omega_2} = \frac{2R - \omega_2}{\frac{\omega_1}{2}}$$

$$\omega_1 = 2\sqrt{2R\,\omega_2} \qquad (5.5.2)$$

Define the energy resolution of the system by $R_s = \frac{\Delta E}{E} = \frac{\Delta V}{V}$

where E is the primary beam energy and $\Delta E$ is the change in energy

V is the accelerating voltage

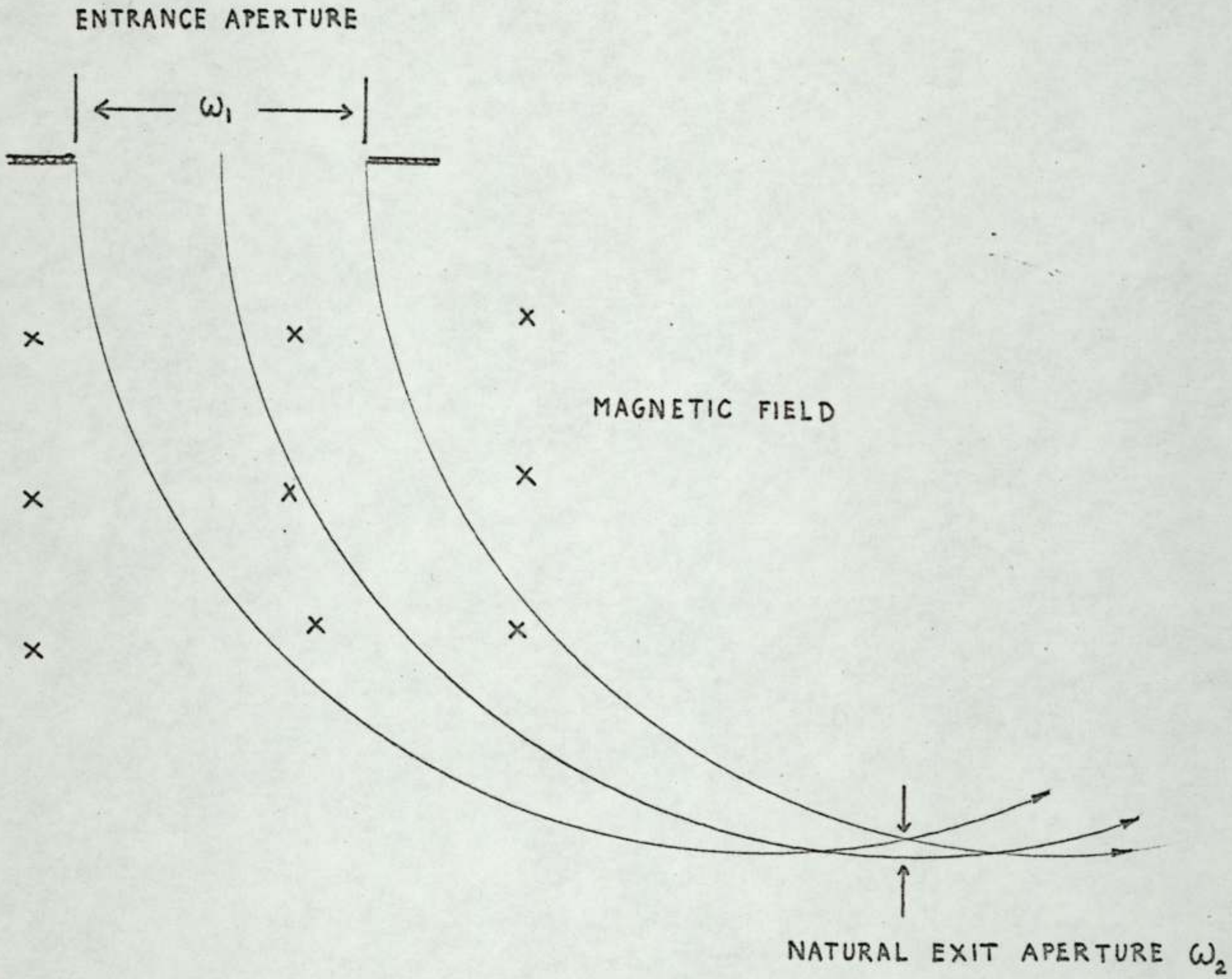

Figure 5.5.3 Focussing of ion beam through the magnetic analyser

From Eq. (5.5.1)

$$\frac{dR}{R} = \frac{dV}{2V}$$

$$\therefore \quad Rs = \frac{2dR}{R} \qquad (5.5.3)$$

The change in radius , dR, of the centre ray allowable for an exit aperture $\omega_2$, is $\omega_2$

$$\text{Hence,} \quad Rs = \frac{2\,\omega_2}{R} \qquad (5.5.4)$$

For this work the exit slits were set at 0.1" to ensure that sufficient beam was hitting the target and the mean radius of the separator R was 10". Eq. (5.5.4) gives a resolution of 2%. The entrance aperture was set at 0.8" so that the beam was reasonably central in the wave guide.

Fig. 5.5.4. shows the spectrum of the 6.13 MeV $\gamma$-ray using the calcium fluoride target. Background in the 4-7 MeV region was found to be virtually negligible hence the discriminators were set to accept only the $\gamma$-rays with energies higher than 4 MeV and the analyser was working in the multiscale mode. The yields from the calcium fluoride target were plotted against the energies of the protons in Fig. 5.5.5. the resonance energy was taken as the point of inflection of the curve which was formed at the energy of half maximum yield.

The maximum energy obtained with the Van de Graaf before sparks occurred was 420 KeV and no measurement was therefore attempted at higher energy.

Photomultiplier gain shift

During the day long operation the gain of the detector was

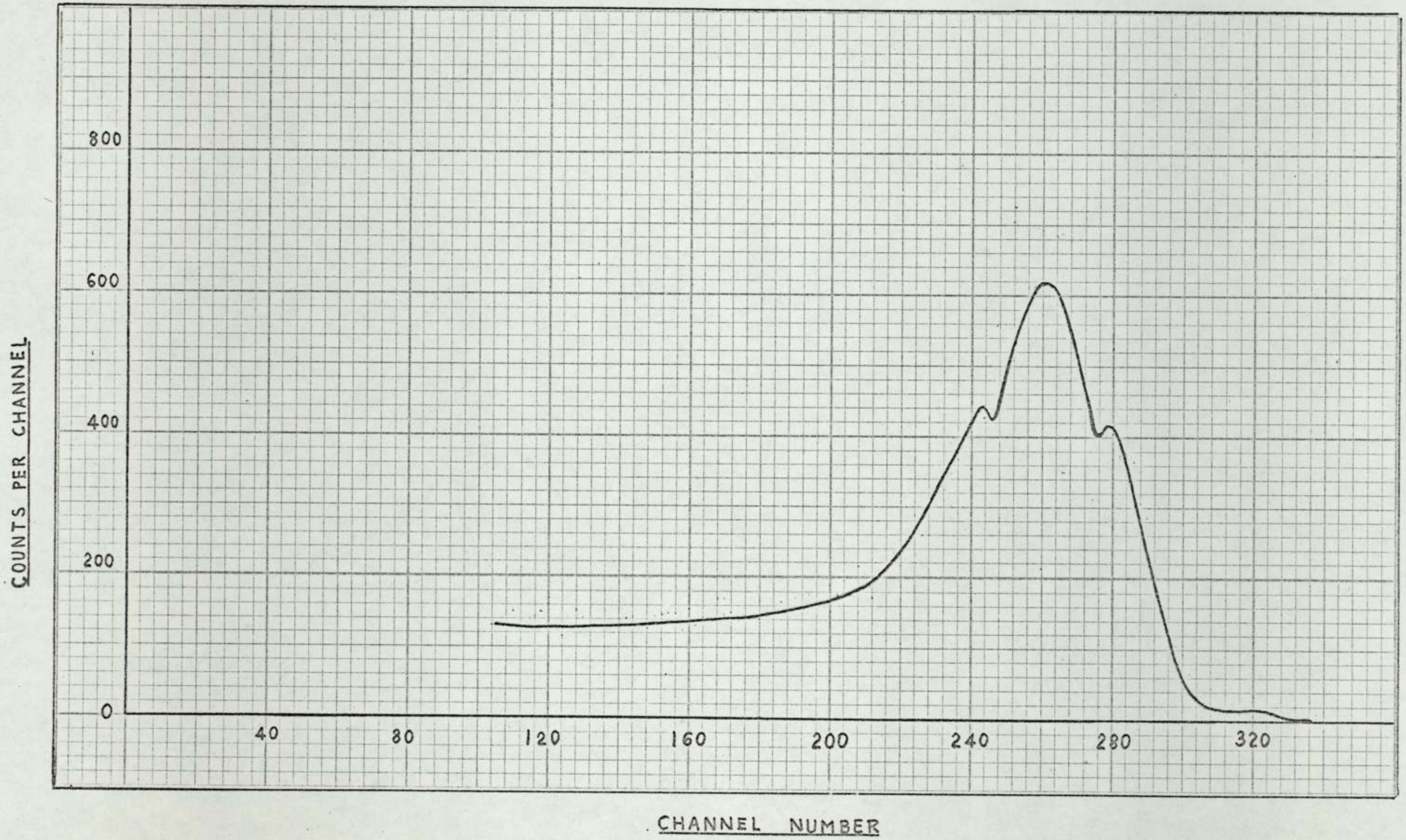

Figure 5.5.4 Gamma-ray spectrum from 50 micro coulomb proton bombardment of $CaF_2$ target

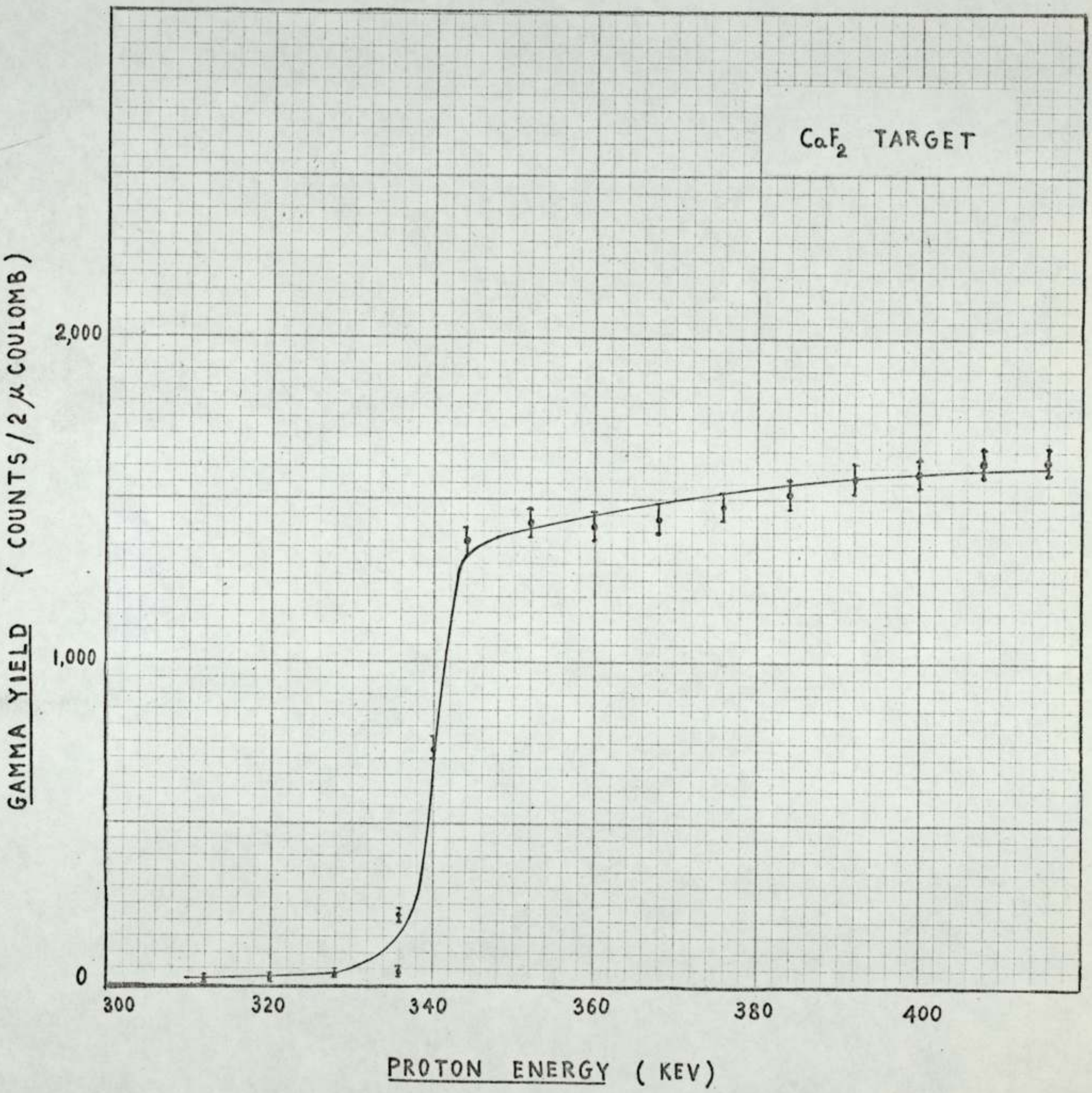

Figure 5.5.5 Gamma-ray yield as a function of proton energy from "Thick" CaF$_2$ target

observed to be slightly shifted which introduced approximately 2% error in the recorded gamma counts. The gain condition did not recover until after 24 hrs. elapsed. The effect was primarily due to the response of the phototube to temperature variation. In general the gain of a scintillation detector has a temperature coefficient on the order of 0.5% per C and because of limited space in the experimental area the detector was situated only 200 cms. away from the heater of the oil diffusion pump which was shielded with a 1.3 cm. thick asbestos plate. The effect was not however observed when working under normal room temperature.

### Beam current monitor

The beam current integrator was tested by injecting a 6.2 $\mu$A test current, the output should cycle at 62 times in 10 sec. It was found that they system was working within 1% accuracy.

### Background from fluorine contamination

It was realised that fluorine contamination in the system particularly the end flange and the stops was a difficult problem to eliminate specially after the system had been used with target containing high fluorine content material. Before the irradiation of microcracked chromium target the extended flight tube was cleaned first in sulphuric acid and then in chromic acid. A new diaphragmmade from spectrographically pure copper was then fitted.

Contamination from fluorine was checked by allowing the beam to hit a dummy target, made from spectrographically pure copper, at different proton energies. The results are shown, comparing with background from natural cosmic radiations, in Fig. 5.5.6.

Figure 5.5.6. Comparison of two different sources of background

| Ep. (KeV) | counts per 1000 $\mu$C on dummy target) | Natural background |
|---|---|---|
| 340 | 1014 ± 32 | 958 ± 31 |
| 344 | 680 ± 26 | 648 ± 26 |
| 352 | 828 ± 29 | 808 ± 28 |
| 368 | 679 ± 26 | 621 ± 25 |
| 384 | 1692 ± 41 | 1633 ± 40 |

Within the limit of experimental accuracy these backgrounds were taken to be the same.

The results of four different microcracked chromium targets are shown in Fig. 5.5.7 - Fig. 5.5.10 for a total charge deposited of 1000 $\mu$C.

## 5.6. Method of estimation fluorine quantity

Inspection of the yield curves indicates that in the vicinity of the resonance the yield curve corresponds to that of a thin target with the observed width at half maximum intensity of about 5.5 KeV. As the energy of the proton increases the yield behaves as that of the thick target. This can be interpreted in the following ways.

The majority but small quantity of fluorine lies in the surface of thickness in energy unit of less than 5.5 KeV. Deep inside the surface much smaller amounts distribute uniformly as seen by near constant of the yield at high proton energies. The calculation

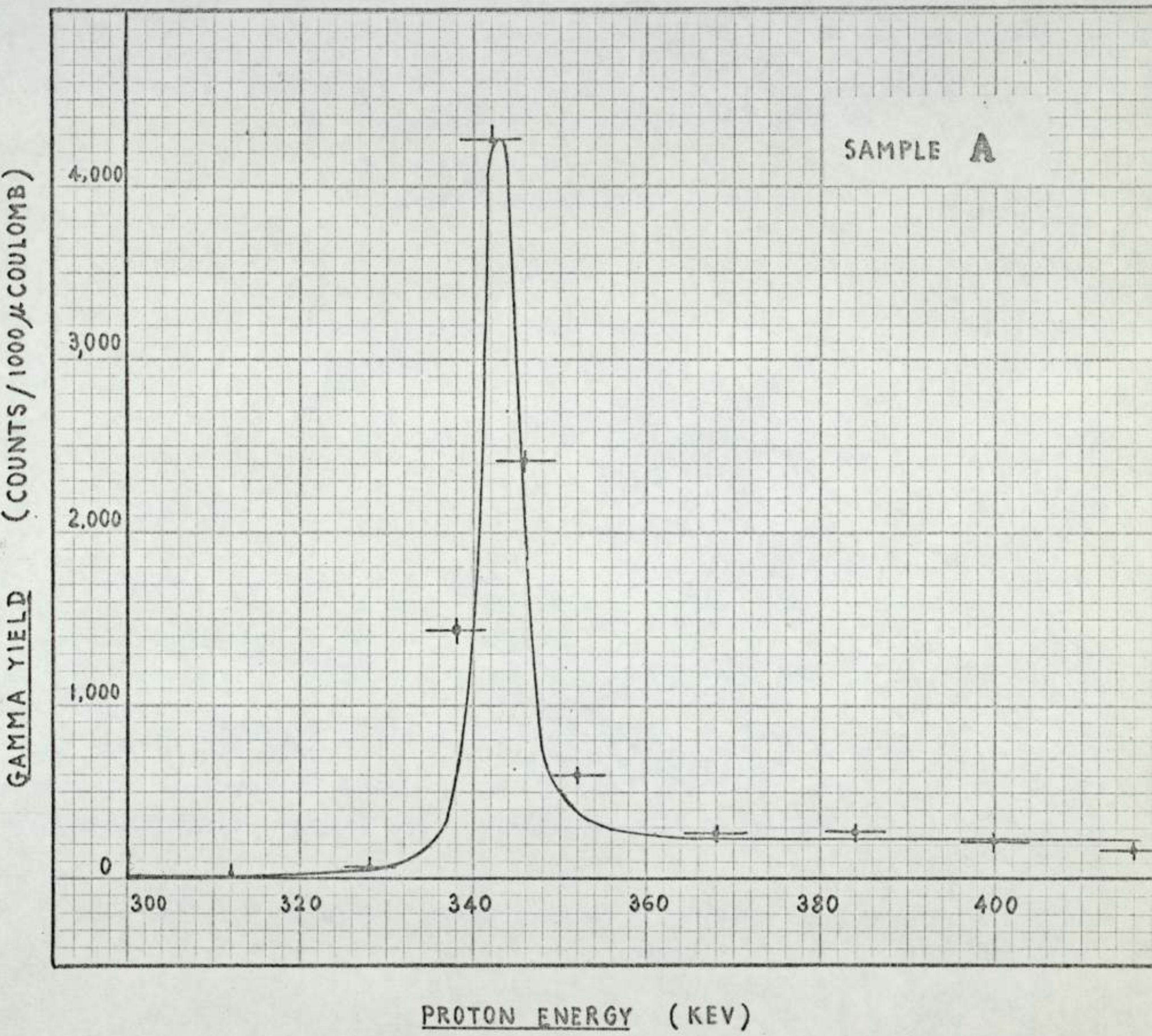

Figure 5.5.7 Gamma-ray yield as a function of proton energy from microcracked chromium (A)

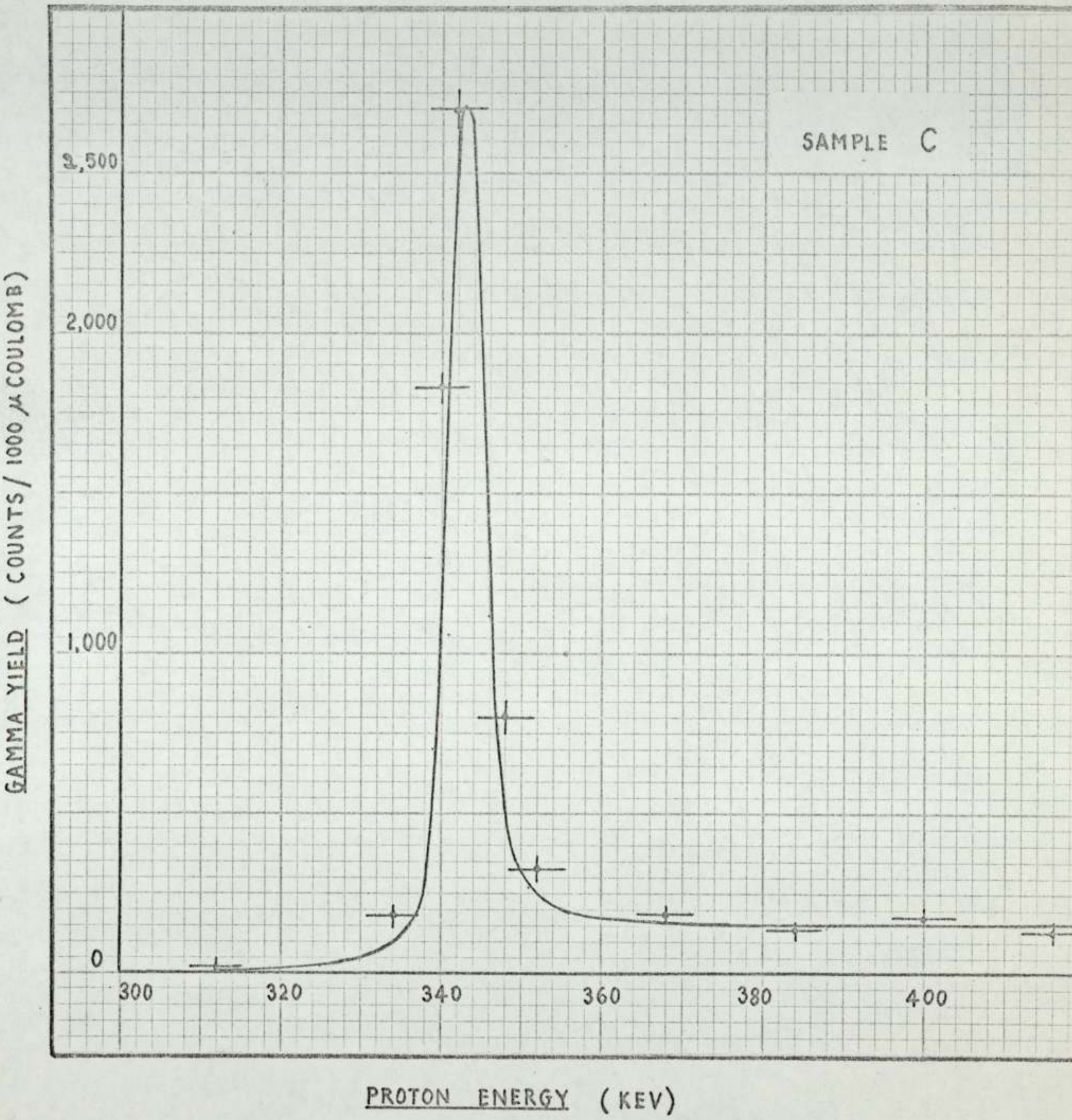

Figure 5.5.8 Gamma-ray yield as a function of proton energy from microcracked chromium (C)

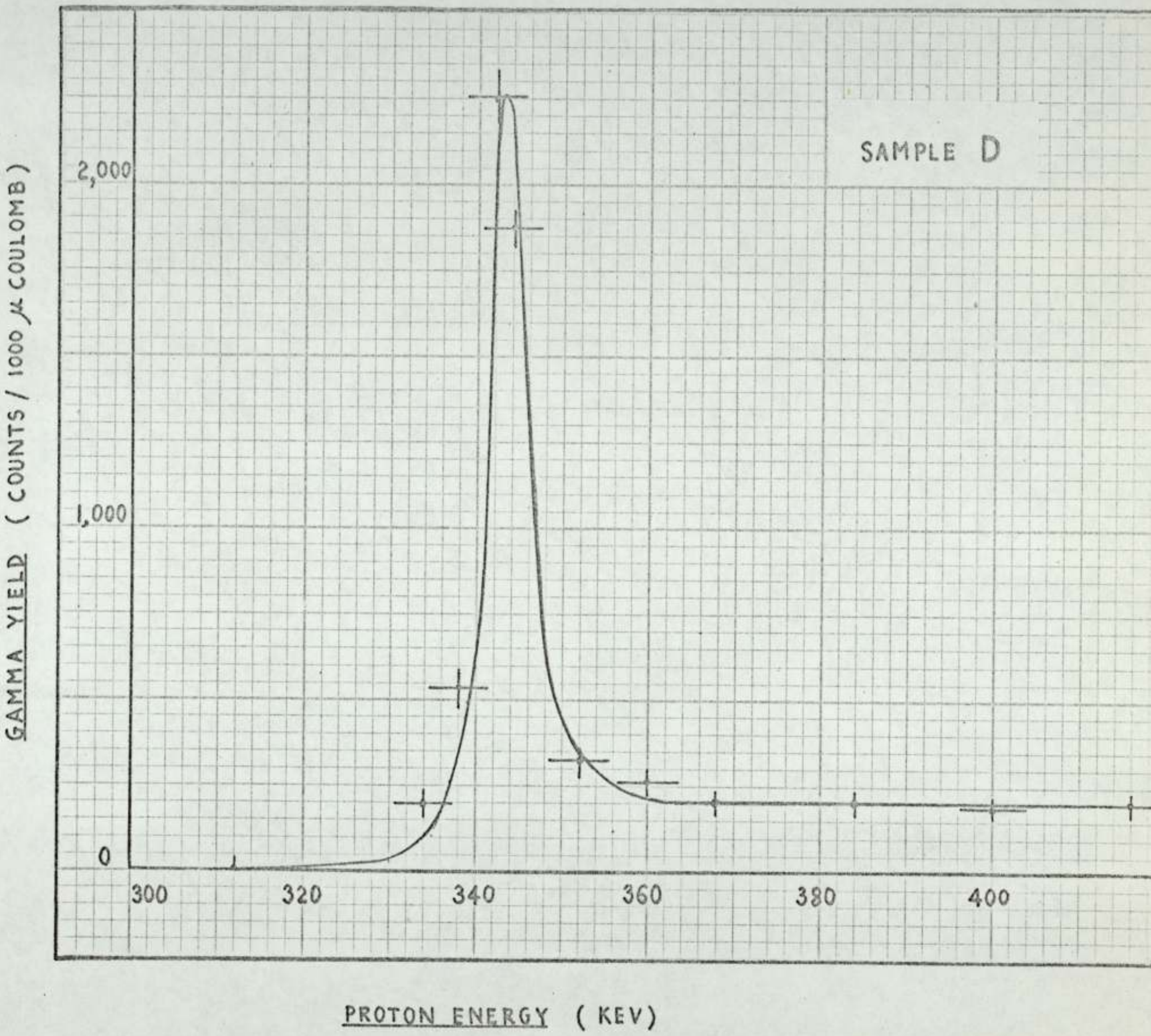

Figure 5.5.9 Gamma-ray yield as a function of proton energy from microcracked chromium (D)

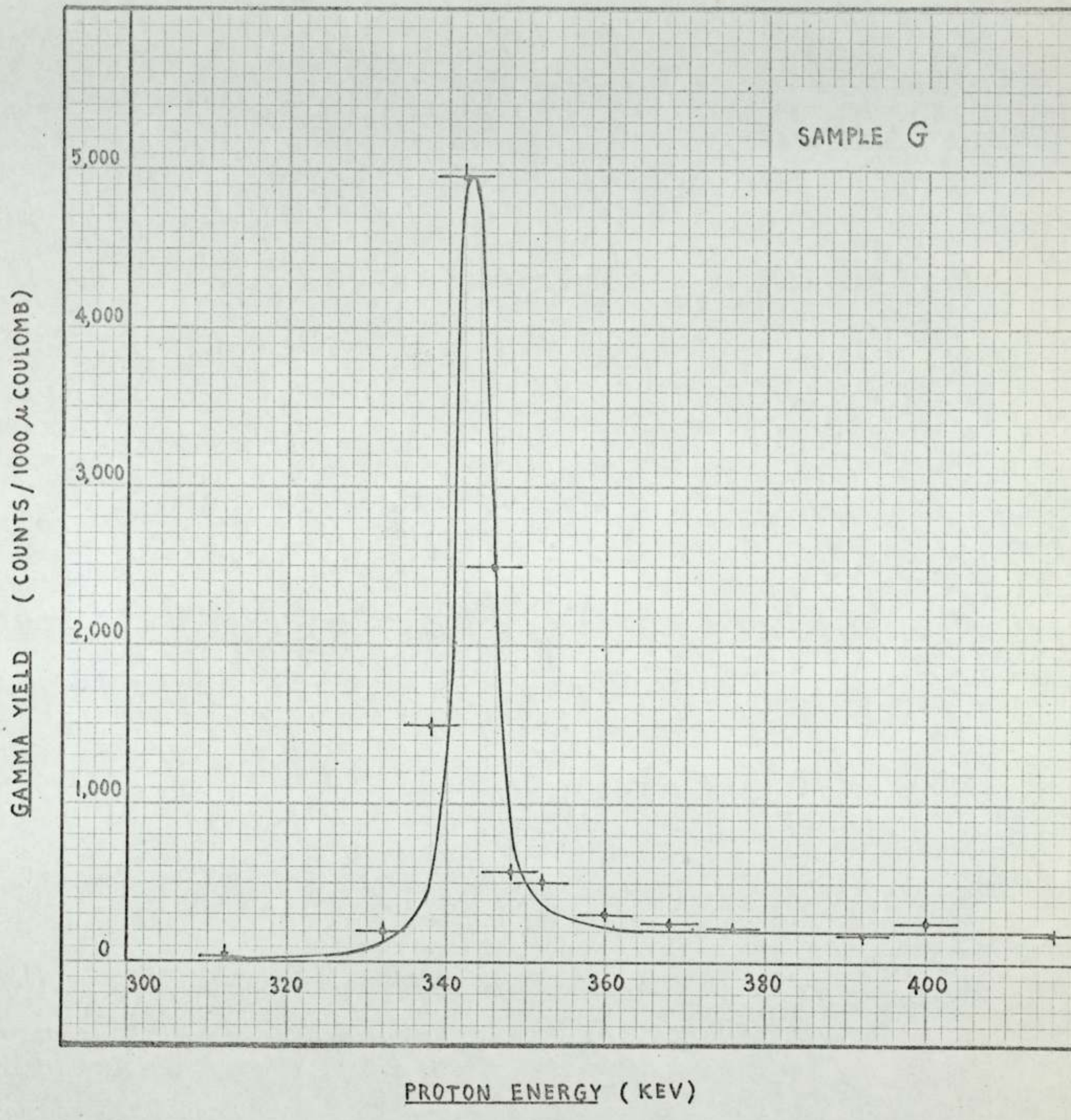

Figure 5.5.10 Gamma-ray yield as a function of proton energy from microcracked chromium (G)

can thus be divided into two independent stages; one of which is the determination of fluorine from a thin target, the other is the thick target calculation. The method is illustrated in Fig. 5.6.1.

Assumptions

The fluorine content was estimated by comparing the maximum yield with that of standard calcium fluoride to eliminate terms like detector efficiency and absorption factors. The calculations were based on the following assumptions.

(i) The fluorine content is small so that the stopping cross section is that due to the inactive matrix (Cr) alone.

(ii) Thickness of the sample can be divided into two different layers containing No and N1 atoms of fluorine per cc. respectively and $N_o >> N_1$.

(iii) Thin target yield curve is symmetric about maximum value.

(iv) Energy straggling in the thin layer is negligible as this error is very small compared to the error in estimating the thickness.

### 5.6.1. Thick target calculation

The maximum thick target yield was given by Eq. (5.2.9) to be

$$Y_{max}(\infty) = \frac{\pi}{2}\frac{\sigma_R \Gamma}{\epsilon}$$

where $\epsilon = \dfrac{1dE}{Ndx}$

N is the number of disintegrable fluorine-19 nucleus per cc. For the sample this can be written (dropping the subscript).

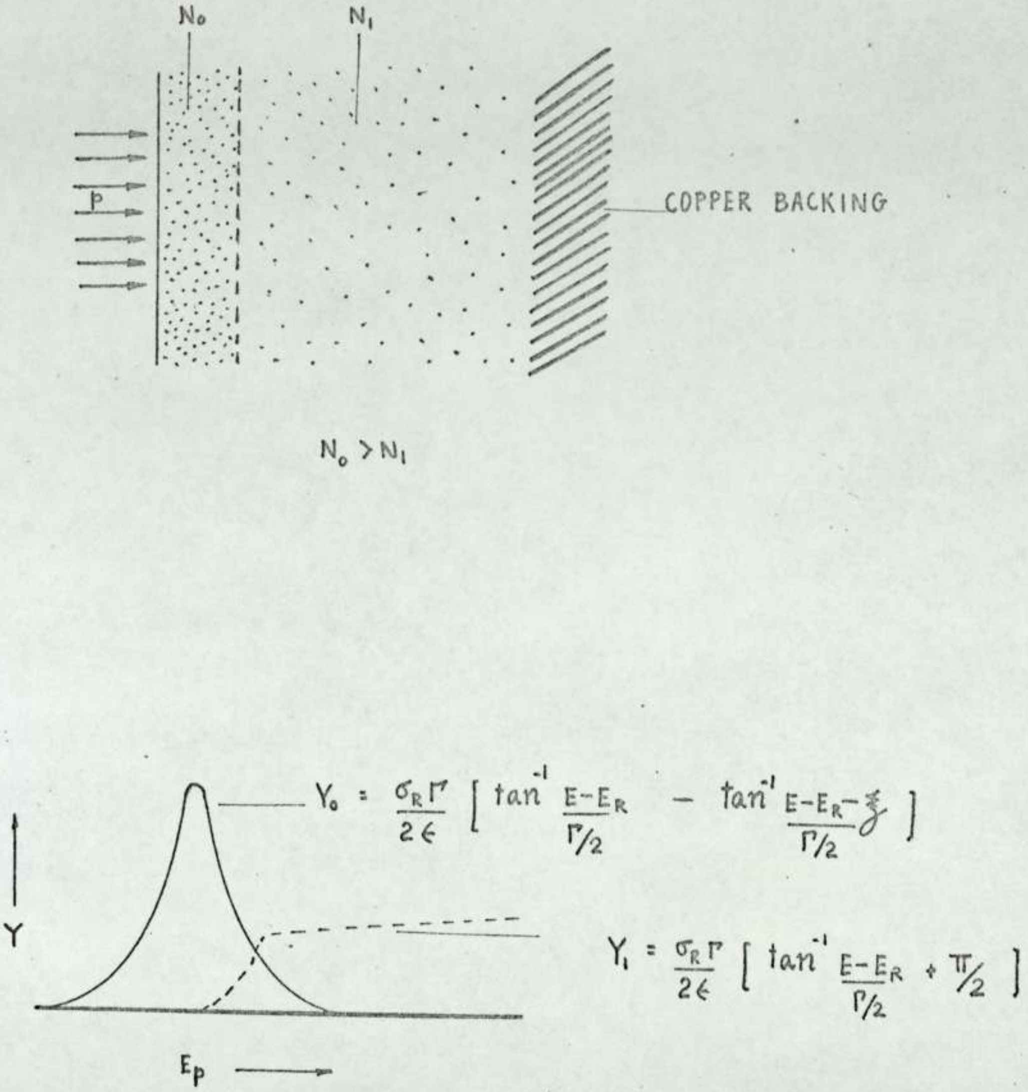

$$Y_0 = \frac{\sigma_R \Gamma}{2\epsilon}\left[\tan^{-1}\frac{E-E_R}{\Gamma/2} - \tan^{-1}\frac{E-E_R-\xi}{\Gamma/2}\right]$$

$$Y_1 = \frac{\sigma_R \Gamma}{2\epsilon}\left[\tan^{-1}\frac{E-E_R}{\Gamma/2} + \pi/2\right]$$

Figure 5.6.1 Illustration of distribution of fluorine in microcracked chromium

$$Y = \frac{\pi}{2} \frac{\sigma_R \Gamma}{\left.\frac{1}{N_1}\frac{dE}{dx}\right|_{Cr}} \qquad (5.6.1)$$

For the standard calcuim fluoride

$$Y^1 = \frac{\pi}{2} \frac{\sigma_R \Gamma}{\epsilon_{CaF_2}} \qquad (5.6.2)$$

Hence

$$N_1 = \frac{Y \frac{dE}{dx}}{Y^1 \epsilon} \qquad (5.6.3)$$

The stopping cross section and the stopping power of calcium fluoride and chromium at 340 KeV were taken from the compilation of Whaling. The errors associated with these experimental values were quoted as 3% and 5% respectively. The maximum yields were obtained by averaging the yields at high energies ( >390 KeV)

The following data were used in the calculation

| Material | Calcium fluoride ($CaF_2$) | Chromium (Cr) |
|---|---|---|
| Stopping cross section ( $\epsilon$) | $22.1 \times 10^{-15}$<br>eV-cm$^2$per F. atom | $23 \times 10^{-15}$<br>eV-cm$^2$, per Cr atom |
| Stopping power $\frac{dE}{dx}$ | $108.5 \times 10^7$ eV per cm. | $191.1 \times 10^7$ eV per cm |
| density ($\rho$) | 3.18 gm. per cc. | 7.1 gm. percc. |
| Atomic weight | 78.08 | 51.94 |
| Avogvadro number | $6.025 \times 10^{23}$<br>molecules per mole | $6.025 \times 10^{23}$<br>atoms per mole |

Results for the thick target calculation expressed as a percentage by weight of the chromium are shown in Fig. 5.6.2.

### 5.6.2. Thin target calculation

The maximum thin target yield was given by Eq. (5.2.8) as

$$Y_{max}(\xi) = \frac{\sigma_R \Gamma}{\epsilon} \tan^{-1} \frac{\xi}{\Gamma}$$

Figure 5.6.2. Results of thick target calculation

| Sample | Y/1 $\mu$C | Weight (g/cc.) | $\%\left(\frac{W_F}{W_{Cr}}\right)$ |
|---|---|---|---|
| A | .234 ± 11.1% | $7.98 \times 10^{-4}$ | .011 ± 12.6% |
| C | .154 ± 11.8% | $5.25 \times 10^{-4}$ | .007 ± 13.2% |
| D | .197 ± 10.4% | $7.71 \times 10^{-4}$ | .01 ± 11.7% |
| G | .215 ± 10% | $7.33 \times 10^{-4}$ | .01 ± 11.7% |
| $CaF_2$ | 800 ± 1.5% | | |

Comparing with the maximum thick target yield of the calcium fluoride (dropping the subscripts)

$$\frac{Y(\xi)}{Y^1(\infty)} = \frac{2}{\pi}\frac{\epsilon}{\frac{1dE}{N_o dx}}\tan^{-1}\frac{\xi}{\Gamma} \qquad (5.6.3)$$

$$N_o = \frac{\pi}{2}\,\frac{Y}{Y^1}\,\frac{\frac{dE}{dx}}{\epsilon}\cdot\frac{1}{\tan^{-1}\frac{\xi}{\Gamma}} \qquad (5.6.4)$$

The thickness of the target can be found from the observed width, $\Delta E$, and the natural width, $\Gamma$, of the resonance at 340 KeV as follows:

Eq. (5.2.5) and Eq. (5.2.8) give

$$Y = \frac{\sigma_R \Gamma}{2\epsilon}\left[\tan^{-1}\frac{E-E_R}{\Gamma/2} - \tan^{-1}\frac{E-E_R-\xi}{\Gamma/2}\right]$$

and

$$Y_{max} = \frac{\sigma_R \Gamma}{\epsilon}\tan^{-1}\xi/\Gamma$$

then at half maximum intensity

$$\tan^{-1}\frac{\xi}{\Gamma} = \tan^{-1}\frac{E-E_R}{\Gamma/2} - \tan^{-1}\frac{E-E_R-\xi}{\Gamma/2} \qquad (5.6.5)$$

Employing trigonometric formula $\tan(\phi-\theta) = \dfrac{\tan\phi - \tan\theta}{1+\tan\phi\tan\theta}$

Eq.(5.6.5)

can be written as

$$\frac{\xi}{\Gamma} \doteq \frac{\dfrac{E-E_R}{\Gamma/2} - \dfrac{E-E_R-\xi}{\Gamma/2}}{1+\left(\dfrac{E-E_R}{\Gamma/2}\right)\left(\dfrac{E-E_R-\xi}{\Gamma/2}\right)} \qquad (5.6.6)$$

Solving Eq. (5.6.6) for E

$$E = \frac{E_R - \xi \pm \sqrt{\xi^2+\Gamma^2}}{2} \qquad (5.6.7)$$

Assume the yield curve is symmetric, the observed width is the difference in values of E, hence

$$\Delta E = \sqrt{\xi^2 + \Gamma^2}$$

$$\therefore \quad \xi = \sqrt{\Delta E^2 - \Gamma^2} \qquad (5.6.8)$$

Because of the uncertainty in reading the generating voltmeter which was about three parts in 400 due to fluctuation in beam energy measured values of $\Delta E$ from the resonance curves would be in relatively large error. Trial measurement of $\Delta E$ indicated an associated error of about 10% hence the values of $\xi$ obtained would be in error by the same amount. However the term $\tan^{-1}\frac{\xi}{\Gamma}$ is not very sensitive to value of $\xi$, a 10% change in $\xi$ would only cause a 5% change in the term $\tan^{-1}\frac{\xi}{\Gamma}$. Hence the value of $\xi$ was assigned to be 5 KeV ± 10% and calculations were based on this value.

The results of the calculation are shown in Fig. 5.6.3

Figure 5.6.3. Results of thin target calculation

| Sample | $Y/1\,\mu C$ | Weight (g/cc) | $\%\left(\frac{W_F}{W_{Cr}}\right)$ |
|---|---|---|---|
| A | 4.277 ± 2.9% | $138 \times 10^{-4}$ | .27 ± 8% |
| C | 2.711 ± 3.1% | $87.5 \times 10^{-4}$ | .17 ± 8.4% |
| D | 2.256 ± 3.5% | $72.8 \times 10^{-4}$ | .14 ± 8.7% |
| G | 4.954 ± 2.8% | $160 \times 10^{-4}$ | .32 ± 8.3% |
| $CaF_2$ | 800 ± 1.5% | | |

Error

The following sources of error were taken into consideration

(i) Error in the value of $Y_{max}$ which was composed of counting statistic uncertainty, gain shift (2%) and beam current integrator (1%). These are combined and shown with each value of Y

(ii) stopping cross section per F atom of $CaF_2$, 3%

(iii) stopping power of chromium, 5%.

(vi) term $\tan^{-1}\frac{\xi}{\Gamma}$, 5%.

These errors were combined quadratically and shown appropriately in Fig. 5.6.2 and Fig. 5.6.3.

## 5.7. Conclusion

The presence of fluorine was detected in the bulk of the electrodeposit at a level of 0.01% and in the surface layers of less than 300 Å thick it varied from 0.1% to 0.3% depending on the quality of cracks. It should be however noted that deep inside the surface the fluorine level was constant within an experimental accuracy irrespective of the type of crack on the surface.

The high surface percentage should be treated with some reservation since it could be an absorption effect and further work is necessary. According to Barrett (62), should the 0.1% to 0.3% be confirmed then probably fluorine diffuses outwards from the inner layers remaining concentrated in the surface on ceasing of plating. An alternative explanation is that fluorine concentrated in the outer layers influences the cyclic cracking and healing processes.

# CHAPTER VI GENERAL CONCLUSION

## 6. Conclusion

The principles and applications of low energy electrostatic accelerators have been described in relevent chapters. Two specific problems have been studied using methods of neutron activation and charged particle analysis. The results of which have been shown in Section 4.7 and Section 5.6 and the following conclusions can be drawn.

(i) The experimental neutron activation analysis method discussed in this work is fairly simple but yet tedious. The irradiation and counting times could be considerably reduced with a higher beam current, as obtained in most modern accelerators. The same information can be obtained by the integrated counts in the photo peak or by only portion of the photo peak counts with the advantage that this can be done automatically, for example, if an on line computer is already present on site. Different stages of analysis can then be performed simultaneously and hence speed up the time taken to obtain results.

(ii) The analysis by the charged particle method is perhaps more complicated than the neutron activation however it can be tried for the analysis of light elements in cases where neutron activation is impossible. With higher beam currents and less energy spread in the beam more accurate results could be obtained particularly in the calculation of a thin target yield. Further more it has also been suggested that silicon is also codeposited at a level of about .005% and complex similar to $S_iF_6^-$ could be responsible for distortion of the chromium lattice resulting in stress of the electrodeposit which is then releived by microracking. Future work on the determination of silicon would be useful.

In conclusion it has been shown that nuclear analytical techniques can be used successfully in cases where more conventional techniques failed.

# APPENDIX A COMPUTER PROGRAMME

## Algol programme for the calculation of induced activities

```
'BEGIN'  'REAL' 'ARRAY' BG[1:90], XX[1:90,1:7], X[1:90,1:7],
                   YY[1:90,1:7], Y[1:90,1:7];
         'REAL' L1,L2, SUM1, SUM2, R,S,W,RO,PC,RR,AA,Y1,B1,K1;
 'REAL' 'ARRAY' T1[1:90], T2[1:90];
   'REAL' T,ER;
         'INTEGER'  B,I,J,C;
         B:=READ;
         'FOR' I:=1 'STEP' 1 'UNTIL'  B 'DO'
               'BEGIN'    BG[I]:=READ;
   T1[I]:=READ;  T2[I]:=READ;
         'FOR' J:=1 'STEP' 1 'UNTIL'  5 'DO'
               'BEGIN'
                     XX[I,J]:=READ;    X[I,J]:=READ;
                     YY[I,J]:=READ;    Y[I,J]:=READ;
               'END'; 'END';
         L1:=0.693/15;  L2:=0.693/2.58;  C:=1;
 ED1:    J:=1;  SUM1:=0; SUM2:=0;
 ED2:    R:= Y[C,J]*EXP(L1*X[C,J]);
         S:= (Y[C,J] +BG[C])↑(1/2)*(R/Y[C,J])/(T1[C]↑(1/2));
         W:=1/(S*S);
         SUM1:=SUM1+ W;   SUM2:= SUM2+W*R;
         'IF' X[C,J+1] 'GT'  100 'THEN' 'GOTO'  ED3;
         J:=J+1;  'GOTO' ED2;
 ED3:    RO:=SUM2/SUM1;
         ER:=(1/SUM1)↑(1/2);
         PC:= ER*100/RO;
  WRITETEXT('('BG=')');  PRINT(BG[C],3,1);   NEWLINE(1);
    WRITETEXT ('('RO=')');   PRINT(RO,6,2);
    WRITETEXT('('PERCENTAGE=')');     PRINT(PC,3,3);
         I:=1;
 ED4:    SUM1:=0;  SUM2:=0;  J:=1;
 ED5:    T:=X[C,J]-XX[C,I];
         R:=Y[C,J]*EXP(L1*T);
         S:=(Y[C,J]*BG[C])↑(1/2)*(R/Y[C,J])/(T1[C]↑(1/2));
         W:= 1/(S*S);
         SUM1:= SUM1+ W;   SUM2:= SUM2+ W*R;
         'IF'  X[C,J+1]  'GT'  100 'THEN' 'GOTO'  ED6;
         J:=J+1;  'GOTO' ED5;
 ED6:    RR:= SUM2/SUM1;    AA:=(1/SUM1)↑(1/2);
         SUM1:=0;  SUM2:=0;
         Y1:=(YY[C,I]-RR)*EXP(L2*XX[C,I]);
         B1:=(YY[C,I]+ BG[C])↑(1/2)/(T2[C]↑(1/2));
         K1:=(B1*B1+AA*AA)↑(1/2)*(Y1/(YY[C,I]-RR));
         W:= 1/(K1*K1);
         SUM1:=SUM1+ W;     SUM2:= SUM2+W*Y1;
         'IF'  XX[C,I+1] 'GT' 100 'THEN' 'GOTO' ED7;
         I:=I+1;  'GOTO' ED4;
 ED7:    RO:= SUM2/SUM1;
         ER:= (1/SUM1)↑(1/2);
         PC:= ER*100/RO;
    WRITETEXT('('R=')');   PRINT(RO,6,2);
    WRITETEXT('('PERCENTAGE=')');    PRINT(PC,3,3);
    'IF'  C 'EQ' B  'THEN' 'GOTO' STOP;   NEWLINE(2);
    C:=C+1;   'GOTO'  ED1;
STOP:      'END';
    15
        EC
```

Typical results print out

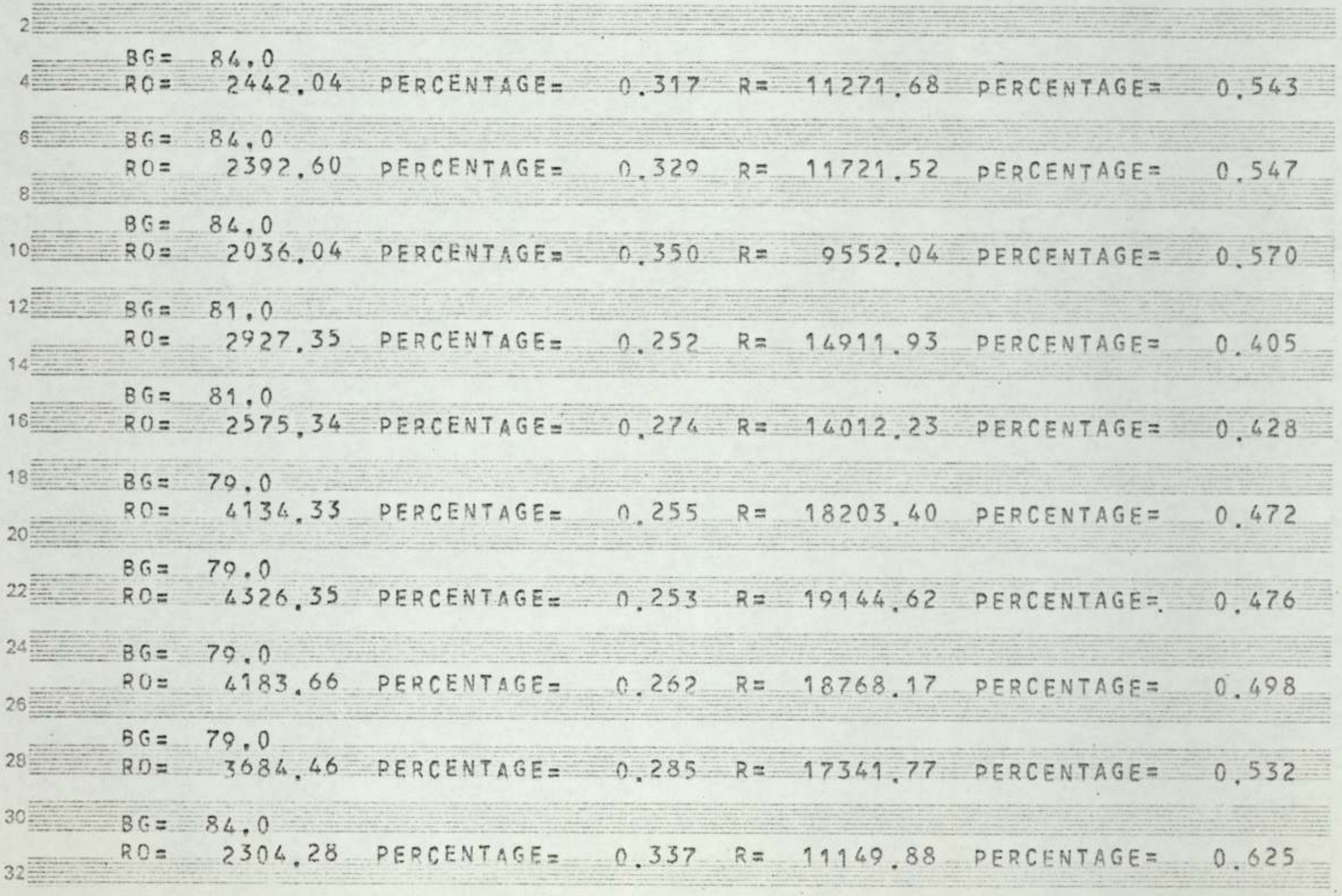

```
BG=  84.0
RO=   2442.04  PERCENTAGE=   0.317  R=  11271.68  PERCENTAGE=   0.543

BG=  84.0
RO=   2392.60  PERCENTAGE=   0.329  R=  11721.52  PERCENTAGE=   0.547

BG=  84.0
RO=   2036.04  PERCENTAGE=   0.350  R=   9552.04  PERCENTAGE=   0.570

BG=  81.0
RO=   2927.35  PERCENTAGE=   0.252  R=  14911.93  PERCENTAGE=   0.405

BG=  81.0
RO=   2575.34  PERCENTAGE=   0.274  R=  14012.23  PERCENTAGE=   0.428

BG=  79.0
RO=   4134.33  PERCENTAGE=   0.255  R=  18203.40  PERCENTAGE=   0.472

BG=  79.0
RO=   4326.35  PERCENTAGE=   0.253  R=  19144.62  PERCENTAGE=   0.476

BG=  79.0
RO=   4183.66  PERCENTAGE=   0.262  R=  18768.17  PERCENTAGE=   0.498

BG=  79.0
RO=   3684.46  PERCENTAGE=   0.285  R=  17341.77  PERCENTAGE=   0.532

BG=  84.0
RO=   2304.28  PERCENTAGE=   0.337  R=  11149.88  PERCENTAGE=   0.625
```

```
BG=  84.0
RO=   2209.92  PERCENTAGE=    0.337  R=  11494.41  PERCENTAGE=    0.586

BG=  84.0
RO=   2320.63  PERCENTAGE=    0.343  R=  11673.79  PERCENTAGE=    0.629

BG=  83.0
RO=   4260.30  PERCENTAGE=    0.201  R=  21450.82  PERCENTAGE=    0.490

BG=  83.0
RO=   4631.05  PERCENTAGE=    0.196  R=  21900.96  PERCENTAGE=    0.510

BG= 830.0
RO=   1748.12  PERCENTAGE=    0.618  R=   6470.11  PERCENTAGE=    0.988

BG= 830.0
RO=   1681.56  PERCENTAGE=    0.660  R=   6581.55  PERCENTAGE=    1.041

BG= 1063.0
RO=   2492.98  PERCENTAGE=    0.465  R=   8950.71  PERCENTAGE=    0.767

BG= 1063.0
RO=   2307.64  PERCENTAGE=    0.504  R=   8795.62  PERCENTAGE=    0.745

BG=  85.0
RO=   2636.95  PERCENTAGE=    0.329  R=  11924.31  PERCENTAGE=    0.687

BG=  85.0
RO=   2237.43  PERCENTAGE=    0.353  R=  10196.69  PERCENTAGE=    0.716
```

```
BG=  85.0
RO=    2262.88  PERCENTAGE=    0.339  R=  10863.87  PERCENTAGE=    0.638

BG=  85.0
RO=    2161.63  PERCENTAGE=    0.353  R=   9959.33  PERCENTAGE=    0.697

BG=  88.0
RO=    4255.36  PERCENTAGE=    0.244  R=  19863.76  PERCENTAGE=    0.632

BG=  88.0
RO=    4008.53  PERCENTAGE=    0.256  R=  18855.47  PERCENTAGE=    0.673

BG=  88.0
RO=    3692.86  PERCENTAGE=    0.273  R=  18483.34  PERCENTAGE=    0.697

BG=  88.0
RO=    3709.63  PERCENTAGE=    0.278  R=  17878.72  PERCENTAGE=    0.743
```

## LIST OF REFERENCES

1. Van de Graaf, R.J., Phys.Rev. 38, 1919 (1931)
2. Cockcroft, J.D., and Walton, E.T.S., Proc.Roy.Soc. (London) A136, 619 (1932)
3. Lawrence, E.O., and Livingston, M.S., Phys.Rev. 40, 19 (1932)
4. Cockcroft, J.D. and Walton, E.T.S., Proc.Roy.Soc. (London) A 137, 229 (1932)
5. Berl, W.G. Physical Methods In Chemical Analysis, Vol.3, Academic Press, 1956
6. Prud'home, J.T., Texas Nuclear Corporation Neutron Generators Hand Book, Texas (U.S.A.)
7. Persico, E., and Ferrari, E., Principles of Particle Accelerators, W.A. Benjamin, Inc., 1968
8. Parkinson, Herb, Bernet and McKibben, Phys.Rev. 53, 642 (1938)
9. Van de Graaf, R.J., Nuclear Instr. and Methods, 8, 195 (1960)
10. Rose, P.H., Nuclear Instr. and Methods, 11, 49 (1961)
11. Rosenblatt, J., Particle Accelerator, Methuen & Co. Ltd., 1968
12. Burrill, E.A., Nucleonics, 18 (12), 64 (1960)
13. Marion, J.B., and Fowler, J.L., Fast Neutron Physics, Part I, Interscience Publishers, N.Y. 1960
14. Hughes, D.J., and Harvey, J.A., Neutron Cross Sections, BNL-325 (1955)
15. Hughes, D.J., and Schwartz, R.B., Neutron Cross Sections, BNL-325, 2nd Ed. (1958)
16. Hughes, D.J., Magurno, B.A., and Brussel, M.K., Neutron Cross Sections, BNL-325, 2nd Ed., Supplementary No 1 (1960)
17. Coleman, R.F., Analyst, 86, 39 (1961)
18. Gillespie, A.S., and Hill, W.W., Nucleonics, 19 (11), 170 (1961)
19. Perdijon, J., Anal.Chem., 39 (4), 448 (1967)
20. Seaborg, G.T., and Livingood, J.J., J.Am.Chem.Soc. 60, 1784 (1938)
21. Albert, P., Proc. of the 2nd Conference on Activation Analysis with Charged Particles, EUR.3896, d.f.e., p3-14 (1948)
22. Rubin, S., Passell, T.O., and Bailey, L.E., Anal.Chem. 29, 736 (1957)

23. Sippel, R.F., and Glover, E.D., Nuclear Instr. and Methods, 9, 37 (1960)

24. Pierce, T.B., Peck, P.F., and Henry W.M., Analyst, 90,339 (1965)

25. Möller, E., and Starfelt, N., Nuclear Instr. and Methods, 5, 225 (1967)

26. Pierce, T.B., Peck, P.F., and Cuff, D.R.A., Analyst, 92, 144 (1967)

27. Bewers, J.M., and Flack, F.C., Analyst , 94, 1 (1969)

28. Piece, T.B., Practicle Aspects of Activation Analysis with Charged Particles, EUR 2957 dfe, p53

29. Inall, E.K., A.E.I. Report, A103, 1950

30. Crumpton, D., Ph.D. Thesis, University of Aston in Birmingham,1967

31. Fowler, J.L., and Brolley Jr., J.E., Revs. Modern Physics, 28, 102 (1956)

32. Benveniste and Zenger, Information on the Neutrons Produced in the $^3H(d,n)^4He$ Reaction, UCRL 4266, 1954

33. Allan, D.L., and Poole, M.J., Proc.Roy.Soc. (London) 204A, 500 (1950)

34. Argo, Agnew, Hemmendinger and Leland, Phys.Rev. 87, 612 (1952)

35. Seagrave, J.D, $D(d,n)^3He$ and $T(d,n)^4He$ Neutron Source Hand Book, LAMS-2162, 1958

36. Gunnersen, E.M., and James, G., Nuclear Instr. and Methods, 8, 173 (1960)

37. Thonemann, P.C., Proc.Phys.Soc. 61, 483 (1948)

38. Breynat, G., and Guillaume, M., Accelerator Target Designed for the production of Neutrons, EUR.2641, d.f.e., 1965

39. Davisson, C.M., and Evans, R.D., Revs.Modern Physics, 24, 79 (1951)

40. Evans, R.D., The Atomic Nucleus, McGraw-Hill, Inc., 1955

41. Klein, O., and Nishina, Y., Z.Physik, 52, 583 (1929)

42. Müller, R., and Maeder, D., Scintillation Spectroscopy of $\gamma$-radiation, Vol. I, Gordon and Breach Science Publishers,

43. Pell, E.M., J.Appl.Phys. 31, 241 (1960)

44. Blankenship, J.L., and Borkowski, C.J., I.R.E. Trans., NS-7:190 (1960)

45. Harshaw Scintillation Phosphors, The Harshaw Chemical Co., Bulletin

46. Girardi, F., and Pauly, J., Radiochem. Acta, 7, 202 (1967)

47. Lamb, Prussin, Harris and Hollander, Anal.Chem. 38, 813 (1966)

48. Paladino, A.E., J.Amer.Ceram.Soc. 48, 183 (1960)

49. Reijnen, P.M. Reactivity of Solids, Elzevier Publishers, Amsterdam, p.562 (1965)

50. Grimes, N.W., Private Communication

51. Lederer, C.M., Hollander, J.M., and Perlman, I., Table of Isotopes, 6th Ed. (1967)

52. Crumpton, D., In Private Communication with Mostafa, A.B.M.G.

53. Yasumi, S., J.Phys.Soc. Japan, 12, 443 (1957)

54. Terrell, J., and Holm, D.M., Phys.Rev. 109, 2031 (1958)

55. Kreger, W.E., and Mather, R.L., Scintillation Spectroscopy of $\gamma$-Radiation, Vol.I, Gordon and Breach Science Publishers.Inc.,196

56. Covell, D.F., Anal.Chem. 31, 1785 (1959)

57. Jaffey, A.H., Nucleonics,18 (11), 4 (1960)

58. Grosjean, C.C., Nuclear Instr. and Methods, 17, 289 (1962)

59. Grosjean, C.C., and Bossaert, W., Computing Laboratory, Publication in University of Ghent, Belgium, 1965.

60. Avery, Bendall, Butler and Spinney, A.E.R.E. Report, R3216, Harwell, 1960

61. Storm, E., and Gilbert, E., Los Alamos Sciencetific Laboratory Report, LA-2237

62. Barret, P.L., Ph.D. Thesis, University of Aston in Birmingham, 1971

63. Ajzenburg-Selove, F., and Lauritsen, T., Nucl.Phys. 11, 1 (1959)

64. Marion, J.B, Rev. Modern Physics, 38, 660 (1966)

65. Fowler, W.A., Lauritsen, C.C., and Laritsen, T., Rev. Modern Physics, 20, 239 (1948)

66. Bewers, J.M., and Flack, F.C., Nucl.Instr. and Methods, 59, 337 (1968)

67. Whaling, W., Hand b. Phys. 34, 193 (1958)